ACOUSTO-OPTIC SENSING FOR SAFE MRI PROCEDURES

A Dissertation
Presented to
The Academic Faculty

by

Yusuf Samet Yaras

In Partial Fulfillment
of the Requirements for the Degree
Doctor of Philosophy in the
School of Electrical and Computer Engineering

Georgia Institute of Technology
May 2020

ACOUSTO-OPTIC SENSING FOR SAFE MRI PROCEDURES

Approved by:

Dr. F. Levent Degertekin, Advisor
School of Electrical and Computer Engineering
Georgia Institute of Technology

Dr. Omer Inan
School of Electrical and Computer Engineering
Georgia Institute of Technology

Dr. Ali Adibi
School of Electrical and Computer Engineering
Georgia Institute of Technology

Dr. Ozgur Kocaturk
Institute of Biomedical Engineering
Bogazici University

Dr. John Oshinski
School of Biomedical Engineering
Georgia Institute of Technology

Date Approved: [March 25, 2020]

yol arkadaşıma

ACKNOWLEDGEMENTS

I am very grateful to my thesis advisor Levent Degertekin for providing his invaluable support and sharing his experience of research as well as life perspective. He supported my PhD life with hours of professional advice and counseling, caring for me and guiding me out whenever I am in the dark, whether it is research or life.

I would also like to thank my other committee members for their support over the years in various capacities and to varying degrees. While our collaborator Ozgur Kocaturk was always many states away, he always had helpful feedback and suggestions. I want to thank John Oshinski for teaching me nuts and bolts of MRI. I am also thankful to Ali Adibi and Omer Inan for taking part in my thesis committee and their feedback and suggestions.

I would also like to thank Robert Lederman and his team at NIH Cath Lab. I would not be able to perform the MRI experiments without their help. It would have been impossible to complete my studies without the help of our collaborator Robert Lederman and his team at NIH Cath Lab. I would like to thank Robert Lederman for providing me a fellowship at NIH to work on my research. I am also grateful that I had the chance to work with Korel Yildirim and became a lifelong friend. He helped me through endless after hours testing. I am also thankful for other members of the Cardiovascular Intervention Lab: Merdim Sonmez, Adrienne Campbell-Washburn, Daniel Herzka and Rajiv Ramasawmy. I enjoyed working with them.

I am thankful to my lab mates: to Sarp Satir for helping me to start me on a smooth PhD journey and my life in Atlanta; to Sushruta Surappa for the endless technical but

mostly non-technical discussions; to Evren Arkan for the support and lifting my spirits with spirits; to Dylan Fife for bearing with my mentoring style that is still in progress; to Sait Kilinc, Ahmad Rezvanitabar and Coskun Tekes for making me feel like at home.

I would like to thank the funding sources that made this research possible - the National Institutes of Health, National Science Foundation and Georgia Research Alliance.

I want to thank my parents; Huseyin and Teslime, and my sister; Fatma. They always respected my decisions and supported me through my endless education.

Finally, I would like to give special thanks to my partner in crime, my adventure buddy, my family; Duygu, for the endless love and emotional support. Feeling your support was the main source of confidence and peace during the first steps in my academic career. Half of this PhD belongs to you (the better half). I can’t wait to begin the next adventure (or the nap) of my life with you at my side.

TABLE OF CONTENTS

LIST OF TABLES

LIST OF FIGURES

LIST OF SYMBOLS AND ABBREVIATIONS

B_0	Static magnetic field
B_1	RF transmit signal
B field	Magnetic field
bSSFP	Balanced steady-state free precession
BW	Bandwidth
CT	Computer tomography
CMT	Coupled mode theory
ECG	Electrocardiography
E field	Electric field
EPI	Echo planar imaging
FA	Flip angle
FEA	Finite element analysis
FBG	Fiber Bragg grating
π-FBG	π-phase shifted FBG
FOTS	Fiber optic temperature sensor
f_0	Larmor frequency
GRE	Gradient echo
MR	Magnetic resonance
MRI	Magnetic resonance imaging
NMR	Nuclear magnetic resonance
PID	Proportional integral derivative
RF	Radio frequency

SAR	Specific absorption rate
SNR	Signal to noise ratio
StD	Standard deviation
TAVR	Transcatheter aortic valve replacement
TEM	Transverse electromagnetic
γ	Gyromagnetic ratio
λ_{Bragg}	Bragg wavelength

SUMMARY

In this work, a novel sensor platform is developed for safer and more effective magnetic resonance imaging (MRI). Even though MRI is a safe imaging technique, it uses powerful radio frequency (RF) fields, which is absorbed by the tissue and causes temperature rise. RF induced heating is a significant safety concern during diagnostic imaging especially for patients with implants and pacemaker leads, as these conducting structures can resonate with the RF field and cause local hot spots. The first part of this work focuses on a sensor for the measurement local RF field with high SNR. When MRI is used to guide interventional devices, such as guidewires and catheters, it is important to track the location of these devices in the body while avoiding RF induced heating and image distortion. Thus, the second part of this work aims to develop RF safe tracking sensor for interventional MRI procedures.

The sensor is based on an acousto-optic modulator coupled with a miniature antenna. This structure is realized on an optical fiber which is immune to the RF field and eliminates the need for conducting lines. The acousto-optic modulator consists of a piezo-electric transducer and a fiber Bragg grating (FBG). The piezoelectric transducer is electrically connected to the miniature antenna and mechanically coupled to the FBG. Local RF signal received by the miniature antenna is converted to acoustic waves by the piezoelectric transducer. Acoustic waves change the grating geometry on the FBG, thus the reflected light from the FBG is modulated. For diagnostic imaging, short dipole antennas are used for sensing the local electric field, which is the primary cause of RF induced heating. For tracking purposes, small loop antennas are used for capturing local

MRI signal which contains the location information. In the scope of this work, an end-to-end model for the acousto-optic sensor is developed and validated through sensitivity and linearity tests. Prototype sensors are built and characterized: sensitivity of 1.36mV/nT and 98 μV/V/m with minimum detectable field strength of 8.2pT/√Hz and 2.7V/m/√Hz and dynamic range of 117dB/√Hz at 23MHz are achieved with 4mm single loop and 8mm short dipole antennas respectively. These figures are competitive with commercial sensors with much larger form factors. Catheter tracking capability of the sensor is also demonstrated under 0.55T and 1.5T clinical MRI system via phantom studies and in-vivo experiments in swine in a 0.55T scanner using a 8F catheter.

CHAPTER 1. INTRODUCTION

The objective of this research is to develop optical fiber based acousto-optic sensors for safe and more effective magnetic resonance imaging (MRI) procedures. Although MRI is a widely used and significant diagnostic imaging modality, RF induced heating is a concern for different MRI procedures; from diagnostic imaging, imaging of patients with implants, to interventional procedures. Thus, RF field measurement with high SNR without image and signal distortion and additional RF heating is key for evaluating MRI safety. In this chapter; basic working principles of MRI is given, interventional MRI procedures are explained, then safety concerns related to MRI are discussed and lastly motivation of the work and sensor specifications are laid out.

1.1 Magnetic Resonance as a Medical Imaging Modality

Magnetic resonance imaging (MRI) is a medical imaging technology that uses strong static and gradient magnetic fields and radio frequency (RF) waves. MRI exploits the physical phenomena nuclear magnetic resonance (NMR) manipulating the hydrogen nuclear spins in the patient body [1]. An MRI system consists of two main components; MRI scanner and control unit. MRI scanner is the heart of an MRI system; MRI scanner excites the hydrogen spins and reads out the MR signal. A cutaway image of a typical MRI scanner showing main components is given in Figure 1-1. A static magnet, mostly in the form of an electromagnet, creates polarizing magnetic field, B_0, manipulating the spins such that a net alignment of the spins will be in the direction of B_0, which is usually along the bore of the electromagnet ($\vec{z}$). According to nuclear magnetic resonance, the spins will resonate at a certain frequency, called Larmor frequency f_0, proportional to the B_0 field.

$$f_0 = \frac{\gamma}{2\pi}|B0| \tag{1-1}$$

where γ is the gyromagnetic ratio, a constant that is specific to the type of atomic nuclei. In medical MRI, hydrogen atoms are used for imaging, the gyromagnetic ratio for hydrogen atom is,

$$\frac{\gamma}{2\pi} = 42.58\ \text{MHz/T} \tag{1-2}$$

Most common B_0 field strength used in clinical settings are 1.5 Tesla and 3 Tesla, resulting in Larmor frequencies of 63.87 MHz and 127.74 MHz respectively.

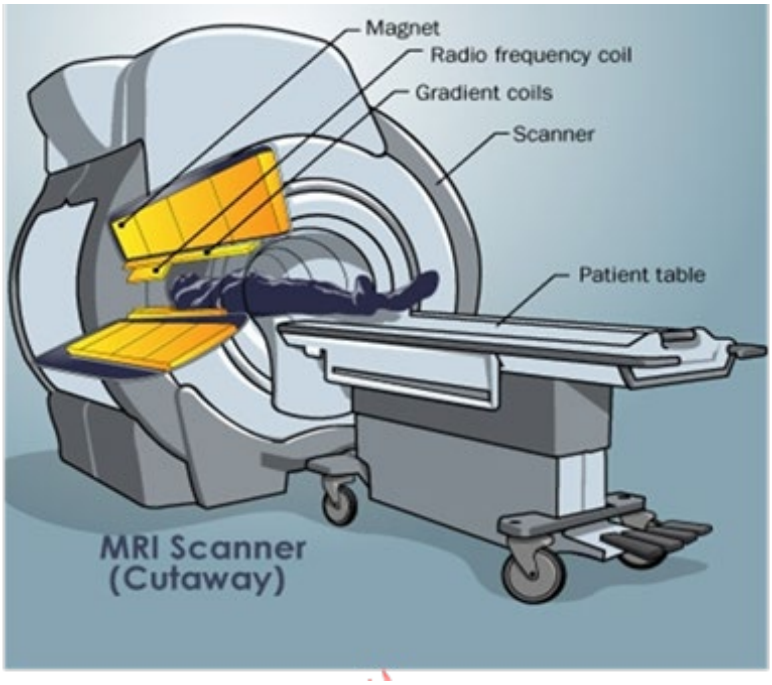

Figure 1-1 MRI scanner cutaway showing main components [2].

Alignment of the spins with B_0 field creates a net magnetization, $\vec{M}$, in the direction of B_0 field. Radio frequency (RF) coils generates an alternating magnetic field, B_1, at Larmor frequency. B_1 is used to excite the spins that perturbs the alignment of $\vec{M}$ with the B_0 field resulting in spin precess. $\vec{M}$ will rotate in B_1 direction by flip angle, θ, with respect to B_0 field as it absorbs the RF energy. Thus, higher the B_1

$$\theta = \gamma \cdot B_1 \cdot t_p \tag{1-3}$$

where $\gamma = 42.58$ MHz/T and t_p is the duration of RF transmit signal (B_1) field. The spin precession decays as soon as the B_1 field is ceased and $\vec{M}$ vector returns back to its original orientation along B_0 field. Figure 1-2 depicts the precession of a net magnetization vector $\vec{M}$ after an excitation pulse of flip angle θ=90°.

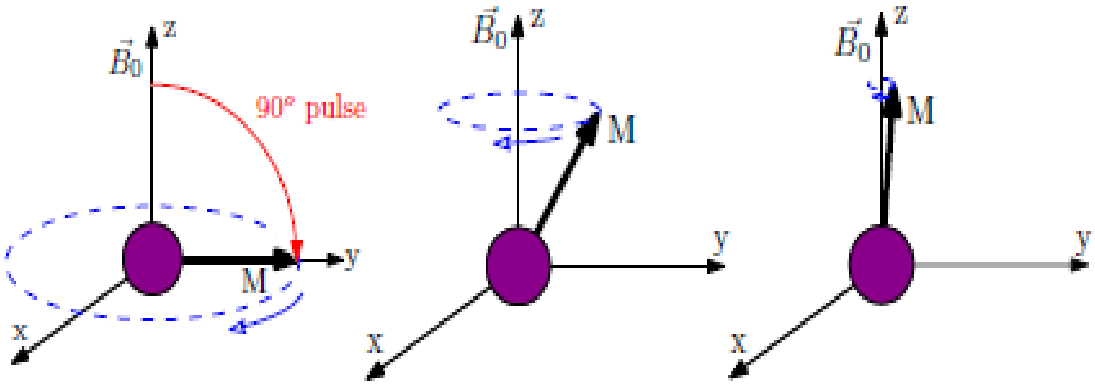

Figure 1-2 Illustration of excitation and precession of net magnetization vector $\vec{M}$ for flip angle θ=90° [3].

The rate of precession decay depends on the physical properties of the surrounding tissue, namely time constants of T1 and T2. Time constants, T1 and T2, are exploited for the differentiation of different tissues. By careful design of MRI sequences, contrast between different tissues can be adjusted in order to get most clinically relevant anatomical and physiological information.

As the $\vec{M}$ vector returns to its steady state position during , spins lose their energy and emits MR signal at Larmor frequency, called free induction decay (FID), [4]. The FID signal can be detected with receiver coils. A changing magnetic field in a loop of wire generates an electromotive force (emf) that is proportional to the change to the rate of change in magnetic flux (ϕ_B),

$$\text{emf} = \frac{d\phi_B}{dt} \tag{1-4}$$

Usually RF transmit coils are used for receiving purposes too. Additionally, specialized coils such as surface coils, head coils, knee coils can be in order improve the sensitivity in the target region of the patient body.

B_0 field has been assumed homogeneous and constant inside the bore. Thus, the FID signal for the whole imaging region of the patient body will have the same frequency and phase, thus the signals from spins at various locations in the object will be indistinguishable from each other. In order to get usable images, gradient coils are used for image encoding. Gradient fields (G or dB/dt) are used for distorting B_0 field slightly at different locations. Figure 1-3 shows different cases when gradients are applied in different orientations. Note

that the G vector is along with the B_0 field, thus only changing local static magnetic field causing small changes in the local Larmor frequency, hence the FID signal, as shown in (1-5).

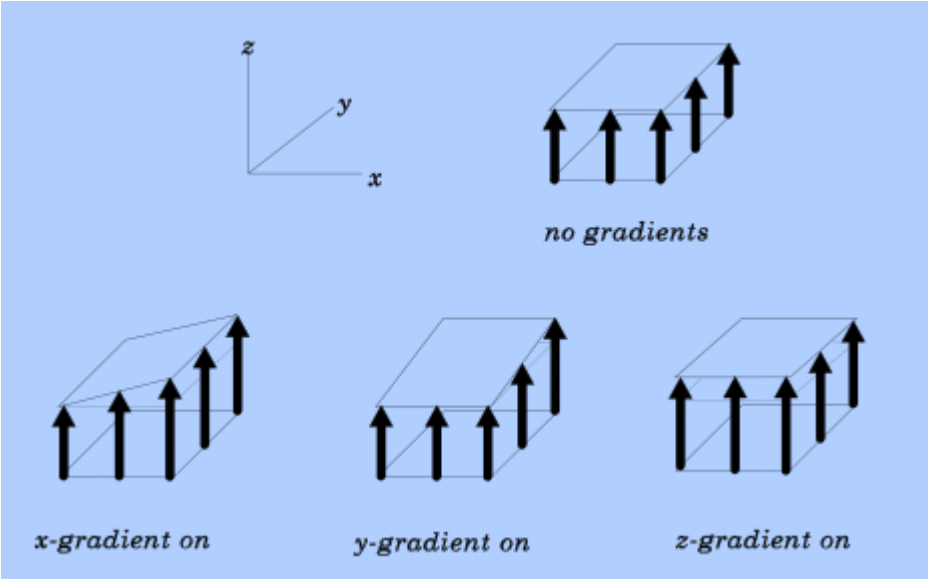

Figure 1-3 Gradient fields are used for image encoding. Gradients are small amplitude magnetic fields along the B_0 field [5].

$$f_{(x,y,z)} = \frac{\gamma}{2\pi}|\mathrm{B}_0 + G_{(x,y,z)}| \tag{1-5}$$

Location information in the FID is encoded with the gradient coils which translates to frequency shifts and time evolving phase. Thus, image can be obtained by taking Fourier transform of the collected signal with the information of the encoding gradient fields and their spatial distribution. Since gradient field amplitude and orientation is controlled electronically, the imaging can be planar (2D) or tomographic (3D). Moreover, any desired

imaging plane can be selected by adjusting the gradient fields and the RF transmit signal without repositioning the patient.

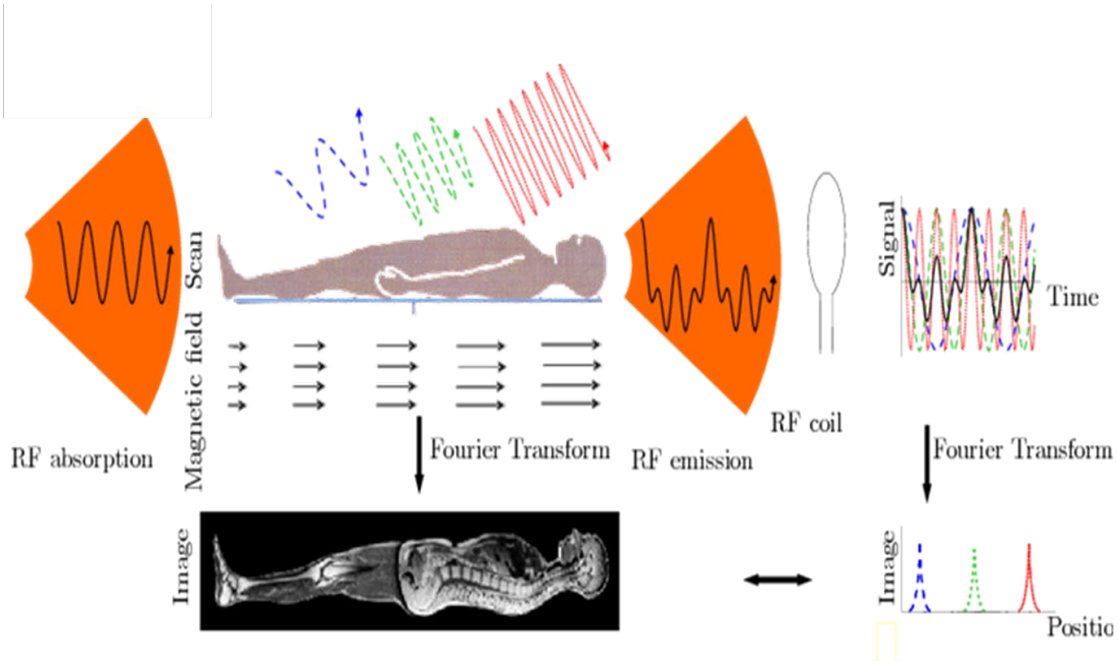

Figure 1-4 Imaging mechanism of an MRI system [6].

Figure 1-4 illustrates the whole imaging mechanism of an MRI system. Patient body is excited by the magnetic field $|B_0 + G_{(x,y,z)}|$ where $G_{(x,y,z)}$ is used for image encoding. Spins at different portions of the body will resonate at different Larmor frequencies due to gradient signal. The MR signal is collected from the whole body with receiver coils. MRI pulse sequences (collection of RF transmit waveform, gradient encoding signal and read-out timings) are designed to fill a spatial frequency domain, k-space, with data points determined by the gradients. The MR image can be reconstructed when k-space is sampled by taking an discrete Fourier transform.

Since MRI provides excellent soft tissue contrast; pathology and abnormalities can be detected at an earlier stage, both anatomical and physiological information (such as early stage tumor detection[7], diffusion imaging [8], functional MRI [9] etc.) can be obtained. Unlike other imaging techniques, different planes, standard or oblique, can be imaged without moving the patient [10]. More importantly, MRI utilizes magnetic and electromagnetic fields, thus procedure is completely ionizing radiation free [11]. Since the introduction of MRI technology to clinical studies in 1982, clinical utilization of MRI has been rising steadily [12]. As of 2013, there are approximately 36000 MRI systems in operation with 11500 in USA alone despite the high start-up (roughly a million dollar per Tesla) and running costs [13]. However, MRI has been extensively used for diagnostic imaging purposes. In the next section, an emerging clinical application of MRI, interventional radiology, will be discussed.

1.2 Interventional MRI

Interventional radiology is a specialized sub field of radiology in which medical therapies are guided by medical imaging to the target tissue within the patient body through a small incision or a body orifice [14]. Interventional techniques include both diagnostic; such as biopsies[15] and angiography[16], and therapeutic techniques; such as tumor ablations [17] and balloon angioplasty [18]. Interventional procedures are preferred over traditional surgical techniques as interventional techniques are minimally invasive thus reducing operation time, patient discomfort, hospitalization time, and procedure related risks. In the case of aortic valve stenosis, aortic valve of the patient needs to be replaced. Traditionally, valve replacement is done via open heart surgery where the rib cage is split and heart is stopped during the valve replacement [19], shown in Figure 1-5(a). As a

minimally invasive alternative, transcatheter aortic valve replacement (TAVR) procedure is performed by carrying the replacement valve over a hollow tube, catheter, to the heart and deployed by an expendable balloon [20], shown in Figure 1-5(b). TAVR reduces the hospital stay from weeks to days compared to open heart surgery.

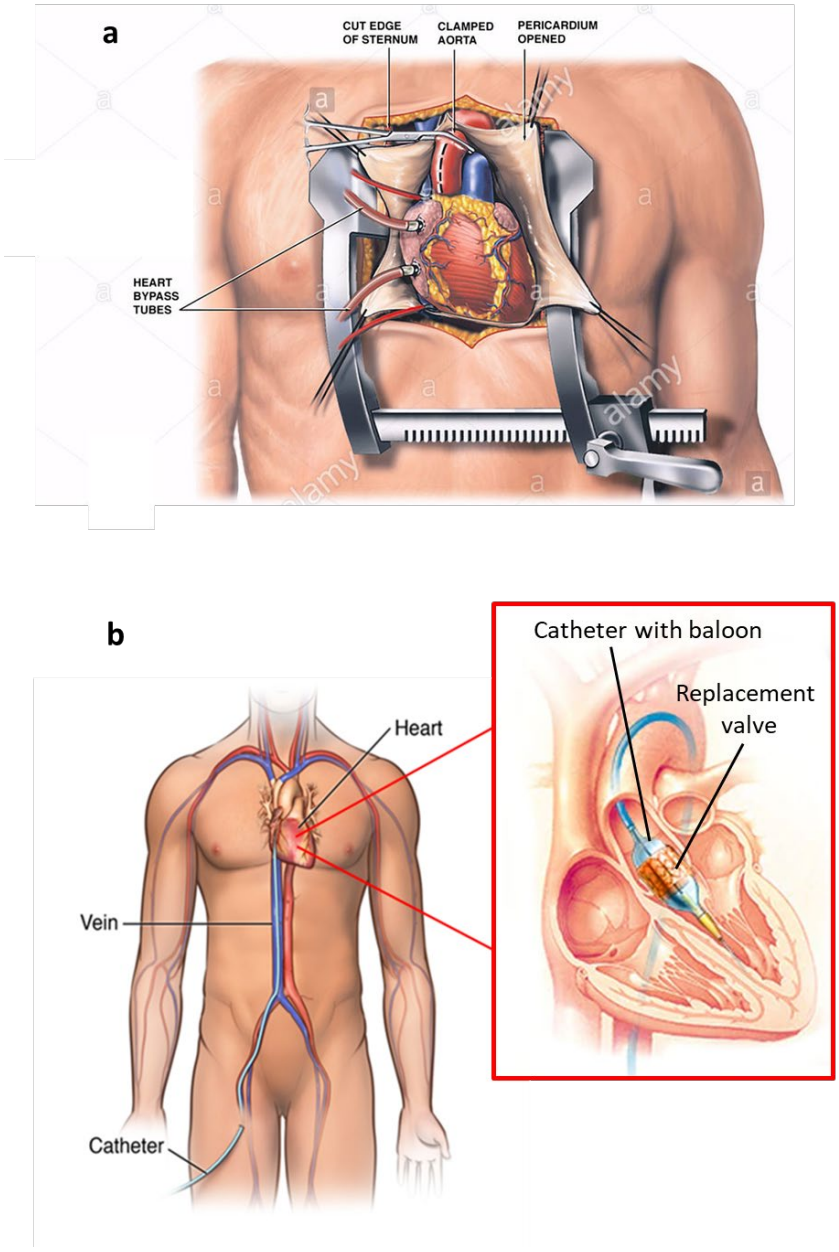

Figure 1-5 a) Open heart surgery for aortic valve replacement [21] b) Transcatheter aortic valve replacement (TAVR) as a minimally invasive alternative [22].

1.2.1 Advantages of Real-time MRI over Fluoroscopy in Interventional Radiology

Interventional device tracking and guidance in the body is an essential part of any interventional procedure. Even though, various imaging modalities have been used for image guidance of certain interventional procedures, X-ray fluoroscopy has been the leading medical imaging technology utilized for real time device-tracking purposes. In X-ray fluoroscopy, a continuous X-ray image of the body is taken and the image is transmitted to a monitor so the movement of a body part, i.e. beating heart, or of an interventional device is tracked through the body. An interventional fluoroscopy performed under a C-Arm image intensifier is shown in Figure 1-6. X-ray fluoroscopy delivers high-resolution projection-based images of metallic guidewires and tungsten or barium sulfate ($BaSO_4$) doped catheters easily with high frame rate. However, there are intrinsic problems with X-ray fluoroscopy; it depicts soft tissue poorly thus requires toxic radiopaque contrast agents. Iodine based contrast agents might cause kidney failures whereas barium sulfate based dyes often result in severe allergic reactions [23]. More importantly, medical staff and patient are exposed to harmful ionizing X-ray radiation for prolonged times during the entire procedure [24]–[27]. Even though medical staff are required to wear lead layered protective vests during procedure to minimize the effect of radiation, the risk is still very high due to years of exposure [25]. The level of ionizing radiation from X-ray imaging contribute to an increased risk of cancer as X-ray radiation limits for pediatric patients than adults rendering fluoroscopy a high-risk alternative for pediatric patients. Thus, doctors prefer traditional surgeries over interventional procedures in pediatric applications in most cases due to X-ray radiation.

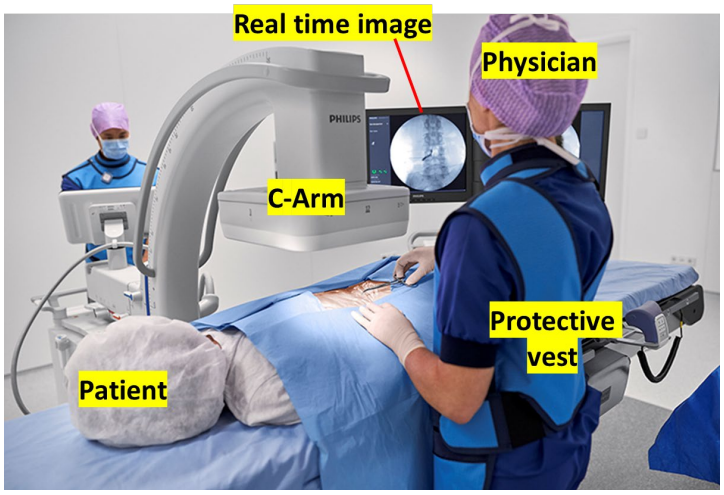

Figure 1-6 Interventional fluoroscopy performed under a C-Arm image intensifier. Note that the physicians are wearing protective vest to reduce exposure to radiation.

MRI is an attractive imaging technology with several advantages for image guided interventional procedures. MRI provides excellent soft tissue contrast thus eliminating the need for toxic contrast agents. More importantly, MRI utilizes only magnetic and RF fields for imaging, thus procedure is completely ionizing radiation free.

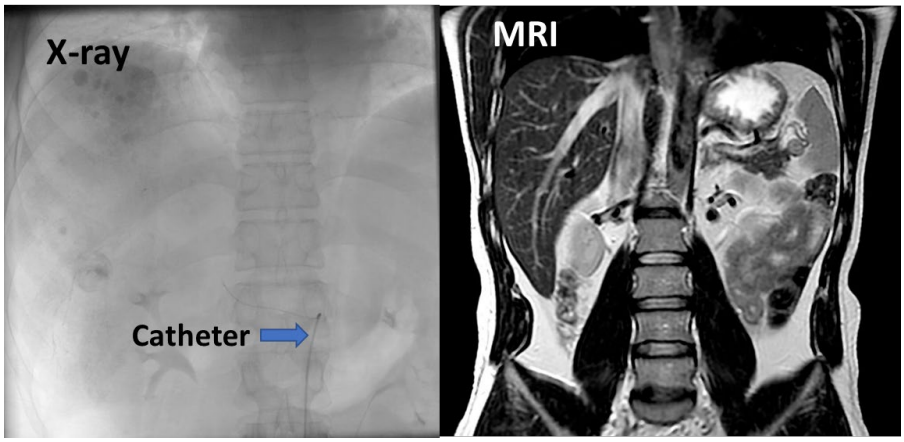

Figure 1-7 Soft tissue contrast comparison of a chest image between X-ray and MRI.

1.2.2 Common Challenges in Developing Interventional MR devices

There are several technical challenges that is slowing the adoption of MRI guidance in interventional radiology. Historically, small bore diameter of the scanner was a limiting the movement of the physician. Previously, mostly open bore scanners and exotic double donut scanners were used for the ample working space provided for the performing physician [28], [29]. However, those scanners are limited to 0.5T field strength and specialized, thus suffers from poor image quality. In the recent years, large bore size – 70 cm and short magnet length's has been developed which allows dual use of the MRI suite for both diagnostic and interventional MRI (iMRI) procedures [30]. Figure 1-8 shows different iMRI suites with open bore scanner, double donut scanner and large bore scanner set-ups. Moreover, image acquisition time for MRI is much slower compared to X-ray and historically prevented real time image guidance. However, fast imaging sequences developed for real time MR image guidance with sufficient image quality [31], [32], given in Table 1-1.

Table 1-1 Characteristics of commonly used iMRI sequences [33]

Contrast weighting	Sequence	Comments
T1/T2	Balanced SSFP (aka, FIESTA, TrueFISP, or balanced FFE)	- Fast - No gadolinium required -At low flip angles, SSFP (or FLAPS) can be used for positive contrast passive tracking of susceptibility markers - Susceptible to B_0 disturbances and blood flow artifacts in setting of slow or turbulent flow
T1+T2*	GRASS, FISP, FFE	-fast, but less SNR efficient than SSFP
T2	TOSSI (RARE, HASTE) TSE	- Flexibility in image contrast - Relatively fast acquisition
T1	FSPGRFLASHT1-FFE	-May be used with IA gadolinium for roadmap guidance

All the equipment inside MRI suit needs to be MRI compatible according to the FDA guidelines [34]. During iMRI procedures, number of medical equipment is required ranging from anesthesia equipment to biopsy needles depending on the specific procedure. Thanks to increase in the demand for iMRI, MRI compatible equipment, robotic systems and tools have been developed for new iMRI applications [35]–[37]. Moreover, interoperative iMRI suites with additional imaging modalities such as ultrasound and CT are developed for complicated iMRI procedures [38]–[40].

Radiopaque markers used for fluoroscopy are not visible under MRI due to the fundamental differences between MRI physics and X-ray physics. Thus, safe and effective device tracking under MRI remains one of the challenges. Different techniques for device tracking under MRI are discussed in detail in the next section.

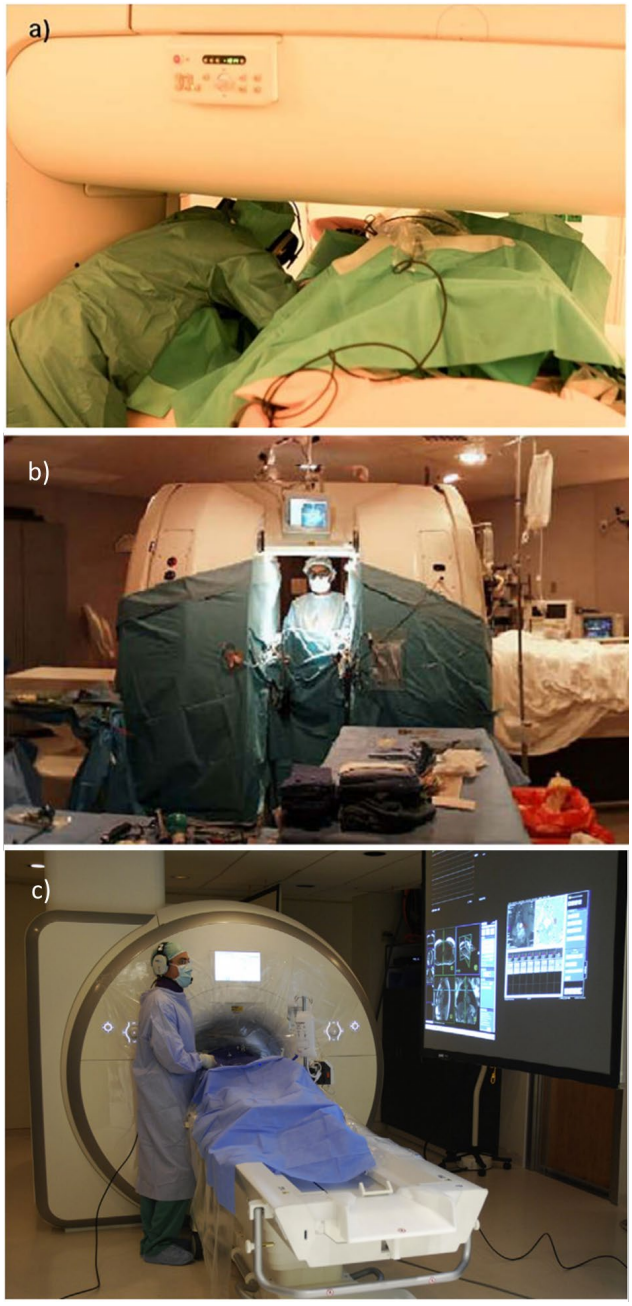

Figure 1-8 a) An open scanner configuration provides sufficient space for the patient and the interventionalist [41] b) GE double donut scanner designed specifically for interventional MRI [28] c) Real-time MR images and hemodynamics are displayed in the room via a projector [42].

1.2.3 Review of Device Tracking Techniques Under MRI

There are two main approaches, based on active and passive techniques, to visualize interventional devices under MRI [43]. Passive visualization relies on the material intrinsic magnetic properties. Ferromagnetic, when placed on the device as fiducial markers [44], [45]. Although passive visualization technique requires minimum device modification, it is still not a preferred technique for physicians due to obstruction of the surrounding anatomy, distortion in the MR images and visualization performance depending on the device orientation. Active visualization techniques require incorporating RF receiver antennas [46], [47], usually in small coil form, to collect localized RF signal [48]. Figure 1-9 illustrates the basic working principle of an active marker with a tracking coil. These miniature coils are used as receiver antennas, imaging only the immediate surrounding of the coil marking the device location on the reconstructed MR image when overlaid with the regular MR image. Figure 1-10 shows the conspicuity difference between an active marker and a passive marker on MRI images of a canine model. While active catheter tacking systems offers conspicuity without obstructing the surrounding anatomy, they suffer from RF induced heating on the conductive transmission lines that transmit the RF signal out of body to MR scanner [49], [50].

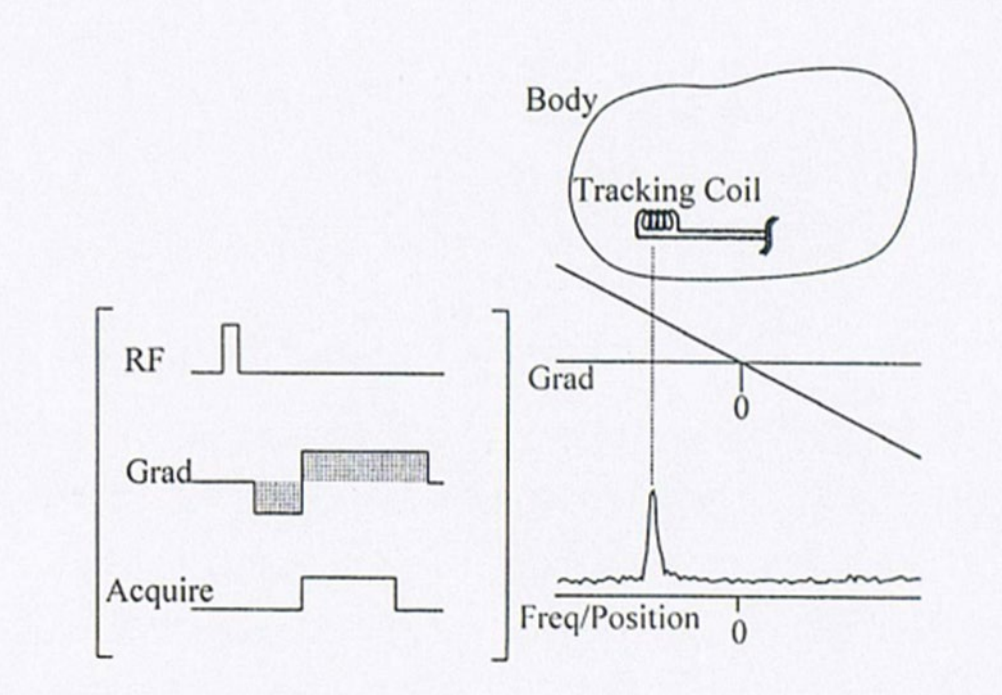

Figure 1-9 Active MR tracking scheme with 1D imaging sequence [51].

Elongated conductors with lengths comparable to RF wavelength may resonate with RF transmit signal and creates local hot spots [52]. Local RF induced heating on catheters or guidewires can cause serious tissue damage and can even risk the patient life. Effect of RF induced heating will be discussed in depth in the Section 1.3. Current heat mitigation techniques are based on either limiting local RF resonances [53]–[55] during RF transmission or replacing electrical transmission lines with optical fiber [56], [57]. Balun and billabong structures are incorporated on the transmission lines to reduce local RF field concentrations [58]. Another RF engineering approach is detuning the resonant structure of the active marker [59]–[61]. However, these RF engineering techniques do not eliminate heating completely and suffer from reduced SNR. Moreover, interventional neuro radiology applications require 3T scanners, in which the wavelength is shorter and

blood perfusion effect is not present to mitigate effect of heating. Therefore, MR safety of interventional devices at 3T is much more serious problem and it is hard to eliminate RF induced heating by implement existing RF engineering techniques.

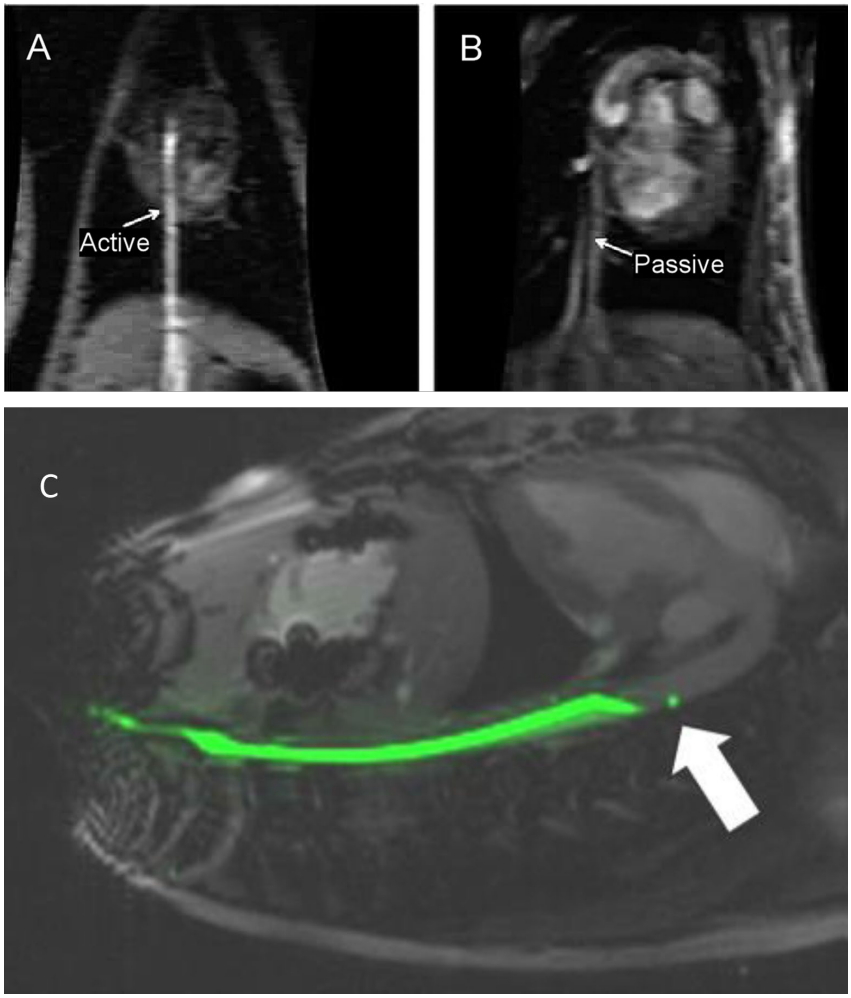

Figure 1-10 Difference in visibility of active (A) (capable of receiving MRI signal) and passive catheters (B) on MRI images of the canine model [62]. Note that the passive catheter is barely distinguishable from the anatomical structure whereas the active marker has distinctive signal along the whole catheter. Visibility of the active marker can be further increased by highlighting the marker channel (C) [50].

Replacing electrical transmission lines with optical fiber eliminates the RF induced heating completely thanks to intrinsic electromagnetic immunity of optical fibers. One method to use optical fiber connection is using an optical Faraday sensor to detect gradient fields for device localization [63]. Because, this system requires additional gradient fields further prolonging the imaging sequence, it is not suitable for real time image guidance. Another approach is using electro-optic modulators as an intermediator between the coil and the optical fiber [56], [64]. The electro-optic modulators used for MRI applications consist of an optical modulator circuit with a laser diode and power up circuit that has photovoltaic power converter, shown in Figure 1-11. The power is supplied by an optical fiber and the local MR signal is carried over a separate fiber. Electro-optic modulator based optical solutions require complex electronics and tight optical alignments resulting in long rigid structures that will impair the mechanical performance which is crucial in clinical use.

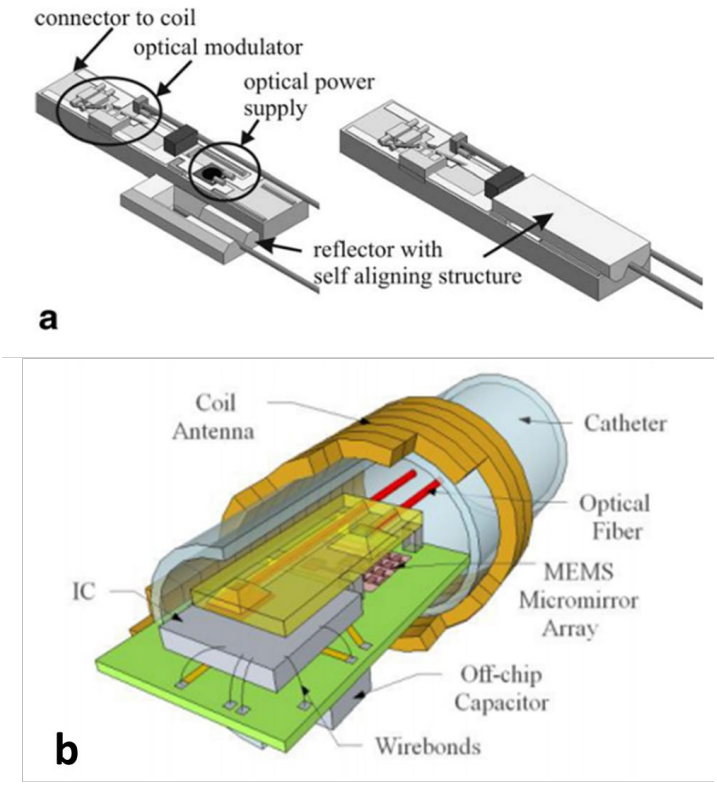

Figure 1-11 Different electro-optic modulator based active markers: a) an electro-optic modulator constructed with discrete components and a self-aligning structure for fiber optic placement [57], b) an electro-optic modulator based on MEMS mirrors and integrated circuit (IC) [64].

1.2.4 Interventional MRI applications: Present and Future

iMRI is used for clinically established routine procedures such as biopsies, tumor ablations, angioplasty, and stent as well as novel procedures developed thanks to MRI guidance. MRI has the ability to differentiate benign and malignant lesions, normally not visible by X-ray or ultrasound-based imaging. Thus, MRI guidance is very effective for breast and prostate biopsy guidance [41]. Another common iMRI application is

neurosurgical guidance for craniotomies, biopsies, intracranial cyst evaluations, subdural drainages and deep brain stimulator leap placement, with lesser complication and infection rates compared to standard surgery [65]. An ever-growing field where iMRI use has been steadily increasing is monitoring various tumor ablation procedures; RF thermocoagulation, chemoablation and laser ablation [66]. MRI is especially practical for non-invasive ablation techniques such as high intensity focused ultrasound (HiFU) [67] as MRI can map the temperature change noninvasively [68]. MRI is also effectively used for cryoablation based pain management therapies [69]. MRI utilization has been limited in vascular and cardiac interventions due to lack of MRI visible, mechanically and electrically safe catheters/guidewires [70].

iMRI adoption has been always hampered by lack of effective MRI markers. Most of the iMRI procedures uses primitive guidance techniques in which the needle or the catheter placement is monitored retrospectively: biopsy needles and catheters are pushed, location is checked with MRI, if the device is not at the target location, device pulled back and push-pull trial is performed until device is delivered to the target location [71]. This process is lengthy and success rate is highly dependent on the experience of the operator. Development of safe device tracking techniques with the introduction of cost-effective MRI scanners will enable new iMRI procedures while reducing the adoption time of already existing interventional techniques. Moreover, better performing markers can be integrated to next generation robot assisted MRI guidance, promising increased efficacy and reduced procedure times [72].

1.3 Safety Concerns Related to MRI

Even though MRI is accepted as a fairly safe imaging technique compared to X-ray based imaging modalities as MRI is ionizing radiation free, there are certain safety concerns related MRI. Patients being scanned and people in the immediate vicinity of the scanner can be exposed to three variants of magnetic fields simultaneously: RF field (B_1), static magnetic field (B_0) and time varying gradient field (dB/dt). Each of these fields poses specific hazards, each of these risks are discussed separately in the following sections 1.3.1, 1.3.2 and 1.3.3.

1.3.1 B_1 Field: RF Induced Heating

During a magnetic resonance imaging (MRI) study, the human body is exposed to RF fields at the Larmor frequency, ranging from 1 MHz in very low field scanner up to 300 MHz (7T) in high field scanners. RF power is deposited in the patient body due to the non-zero electrical conductivity of biological tissues [73]. This absorption causes temperature rise, called RF induced heating, which is the primary safety concern for MRI [11]. Primary heating mechanism is the joule heating of the resistive tissue due to eddy current formation by the fast-changing RF field. In extreme cases, RF induced heating will accumulate and cause RF burns, an example of RF burn is shown in Figure 1-12. Note that RF induced heating concerns only the patients during MRI scan and has insignificant effect on MRI staff, since the magnitude of RF field decreases exponentially outside of the bore of the scanner.

Figure 1-12 Superficial skin burn caused by RF induced heating. [74]

1.3.1.1 RF Dosimetry and SAR Measurement

RF dosimetry studies RF field interaction with the tissues. The RF absorption by the tissue is a complex problem with many variables including field strength, dielectric properties of the tissue, RF field – tissue orientation, field polarization, geometry of the specific tissue, RF frequency etc [75]. The dose rate is called specific absorption rate or SAR. SAR is defined as the amount of RF power absorbed per unit of mass of an object indicated in W/kg. In order to mitigate RF induced heating, RF excitation is bound by safety limits of SAR for different MRI applications [76]. SAR is defined as

$$\mathrm{SAR} = \frac{\sigma\,|E|^2}{2\rho}\ \ [\mathrm{W/kg}] \tag{1-6}$$

where σ is the electric conductivity of a uniform conducting tissue, ρ is tissue density and E is the induced electric field.

In order to mitigate the risk of RF burns, SAR limits are determined to dictate the maximum RF transmit signal power level and duration. FDA and IEC 60601 SAR limits

are given below [34], [77], [78]. All commercial MRI scanners have a built-in tool for SAR calculation using the weight of the patient and some empirical RF field parameters. The built in SAR monitors are quite conservative to assure safety and used as a general guide to prevent RF induced heating. However, excessive concentration of RF energy -hot spots- can occur even when the SAR level is kept way under limits due to uneven distribution of RF field within the body. Thus, it is imperative to measure local SAR values in order to better understand the RF field – tissue interaction and assure patient safety.

Table 1-2 International Electrotechnical Commission SAR limits for MRI

Limit	Whole-Body Average	Heat Average	Head, Trunk Local SAR	Extremities Local
IEC (6-minute average)				
Normal (all patients)	2 W/kg (0.5°C)	3.2 W/kg	10 W/kg	20 W/kg
First level (supervised)	4 W/kg (1°C)	3.2 W/kg	10 W/kg	20 W/kg
Second level (IRB approval)	4 W/kg (>1°C)	>3.2 W/kg	>10 W/kg	>20 W/kg
Localized heating limit	39°C in 10 g	38°C in 10 g		40°C in 10 g
FDA	4 W/kg for 15 min	3 W/kg for 10 min	8 W/kg in 1g for 10 min	12 W/kg in 1g for 5 min

There are two methods of localized SAR measurement; local RF field measurement and temperature measurement. From (1-6), SAR can be measured with an E field sensor and if tissue properties are known. Standard E field probes are based on short dipole antennas, that dipole length needs to be shorter than 1/10 of the RF wavelength in the tissue-equivalent material to assure field uniformity over the entire dipole length, i.e. dipole length needs to be smaller than 5 cm for a 1.5T MRI. Since E field sensitivity of shorty dipole is proportional to dipole length, dipole size needs to be carefully selected for balance

the localization area and SNR performance. Sensitivity of short dipole is anisotropic, therefore three orthogonal short dipoles are used for isotropic measurement, especially important when the polarization of RF field is unknown such as in a complex shaped non uniform tissue [79]. Short dipole based E field probes coupled to a monitoring instrument by either a highly resistive transmission line or fiber optics. Even though the resistive transmission line is easiest to implement, transmission line will pick up the E field too and hinder the accuracy of the probe. In order to prevent this, optical fiber link with electro-optic modulators can be used. Short dipole based different E field probes are shown in Figure 1-13.

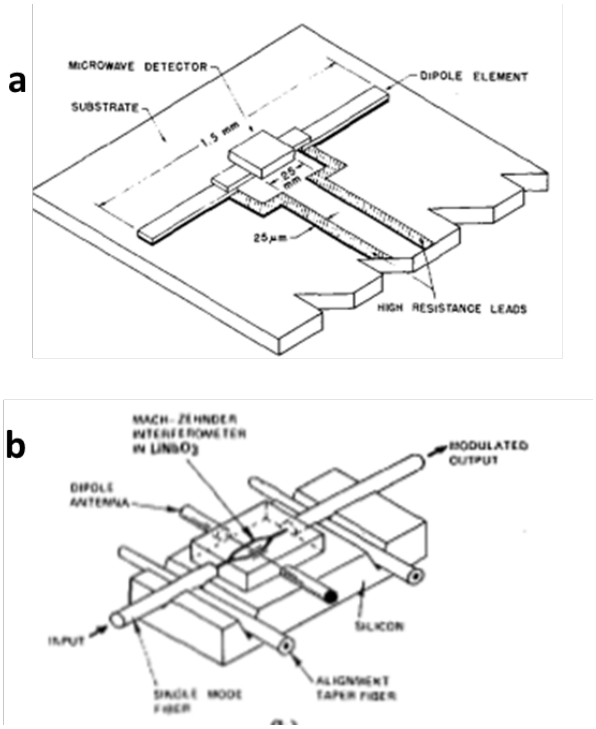

Figure 1-13 a) Detail of dipole/detector for miniature E-field probe [80] b) Short dipole E field probe using electro-optical modulator (antenna/integrated optical modulator) [81].

Another common technique for E field measurement is use of electro optic sensors. Certain crystals, such as $LiNbO_3$ exhibit Pockels effect, that the refractive index changes proportional to the ambient E field [82], [83]. Then the refractive index change can be probed by passing a laser light through it. Optical modulation can be achieved via various read-out topologies inducing a change in the amplitude, phase or polarization stage of the laser light [84]. Figure 1-14 is showing an example of an electro-optic E field sensor developed for MRI systems. Pockels effect E field probes are fully dielectric thus the unwanted electromagnetic coupling is eliminated. However, they suffer from poor sensitivity.

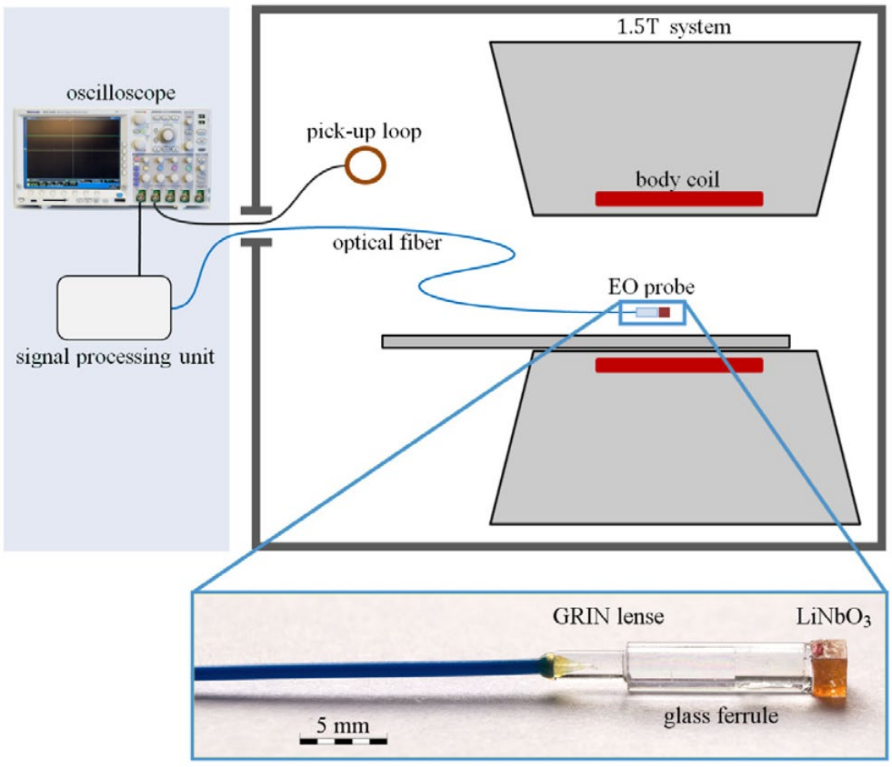

Figure 1-14 Schematic overview of an electro optic E-field probe for SAR measurements for MR systems. The sensor head is connected to the signal processing unit via a 10 m long polarization maintaining optical fiber. The signal of a pick-up loop placed in the Faraday cage is used for reference and triggering [83].

SAR can be also determined by measuring temperature change due to RF field absorption. SAR and temperature relationship is given in (1-7).

$$\mathrm{SAR} = 4186 \frac{c_H \, \Delta T}{t} \ [\mathrm{W/kg}] \tag{1-7}$$

where c_H is the specific heat capacity of the tissue, ΔT is temperature change in ^{o}C, t is RF exposure duration and 4186 is the conversion factor from kcal to joule. In live tissue

measurements, the thermal diffusion into the surrounding tissues and blood perfusion creates a cooling effect leading to read out errors, especially when the excitation duration is relatively long. A comparison between the SAR distribution and corresponding temperature rise, considering thermoregulated and basal perfusion as well as thermal properties of tissues, is shown in Figure 1-15.

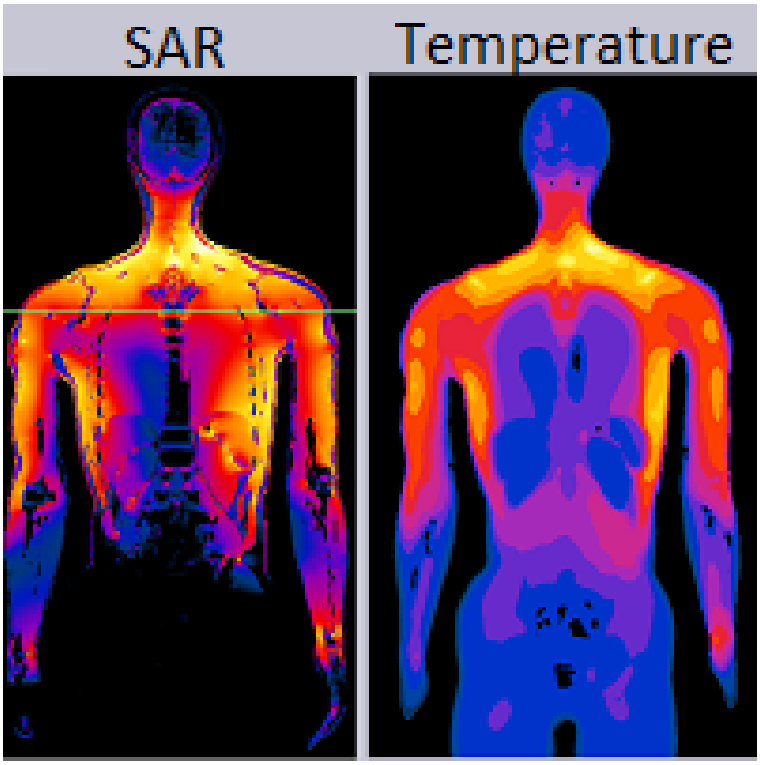

Figure 1-15 Comparison of RF induced SAR and corresponding temperature rise, considering thermoregulated and basal perfusion as well as thermal properties of tissues. [85]

Temperature for SAR can be measured in two main way: indirect and direct. In indirect methods, special MRI sequences are used and spin relaxation shift due to temperature elevation is exploited [68]. Direct temperature measurement use fiber optic

based temperature sensors (FOTS) in order to prevent additional RF induced heating. Birefringent crystal FOTS [86], GaAs based sensors [87] and fiber Bragg gratings [88], [89] are the most used optical temperature sensors in the literature [90], [91]. FOTS offers compact and robust solutions and can be easily integrated with other MRI devices such as catheters [50] and pacemakers [92].

1.3.1.2 RF Induced Heating on Metallic Devices and Implants

In the presence of long conductive structures on or within the patient body, the effect of RF induced heating will be increased [52], [93], [94]. Elongated metallic devices, such as pacemaker leads, ECG cables, guidewires, long implants etc, can act like an RF wire antenna collecting RF field, E field in particular. The induced current will accumulate at certain points, such as the tip of a guidewire, creating 'hot spots' along the metallic structure. The maximum RF induced heating will occur when the metal structures inside the body resonates with the RF field. Patients with certain implants such as pacemaker leads, neurostimulators and active implants are rejected by most hospitals due to increased risk of RF induced heating on the implant. Even the RF power is kept within SAR limits given Table 1-2, one can not assure the safety of the patient as there can be local SAR values way above the limits, as can be seen in Figure 1-16; there is three orders of magnitude difference between the minimum and maximum SAR on the same wire. Figure 1-17 shows an image of third degree skin burns caused by ECG leads. Placement of the electrodes is indicated by the graphical overlay. The wounds are oriented in between the electrodes, which indicate burn caused by the ECG leads instead of the ECG electrodes.

Note that deepest tissue damaged happened towards the tip of the leads, which is consistent with the SAR distribution given in Figure 1-16.

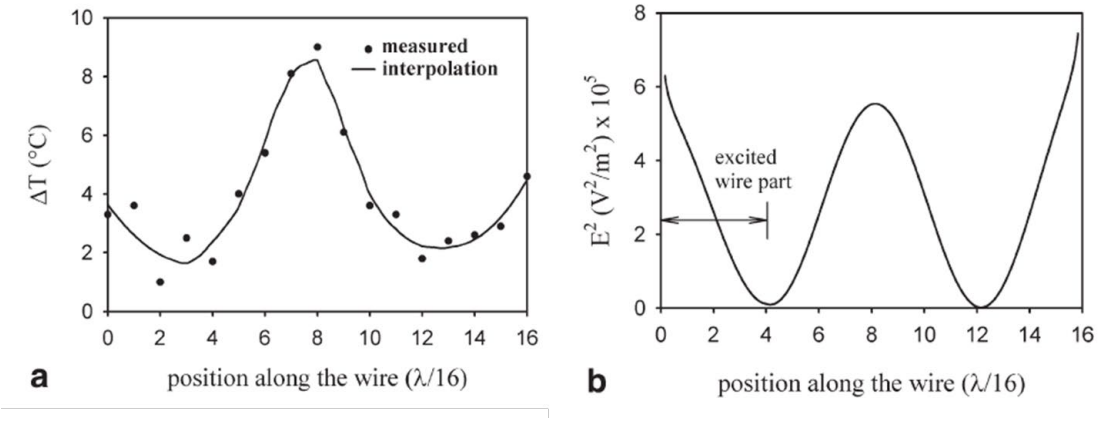

Figure 1-16 a: Experimental evaluation of the temperature increase along a metallic λ length wire. Maximum temperatures are observed at both tips of the wire, and for a λ/2 distance from the tip. Heating is observed not only at the wire tips but also along the wire. b: Simulated squared E-field (SAR) along a metallic λ length wire [93].

Recently, a new safety parameter, B_{1+rms} is introduced to have a better assessment of the implant safety under MRI, ISO/TS 10974:2018 standard. B_{1+rms} is a time-weighted average RF magnetic field exposure independent of the patient [95]. B_{1+rms} is a function of physical properties of the RF field; flip angle, pulse type, number of echoes, slices, and TR. New active implants are required to have a B_{1+rms} limit, but this ISO/TS 10974:2018 does not govern the millions of older implants. As those patients need MRI scans to be able diagnosed properly, physicians need a better way of determining safety of implants. One way might be use of RF field probes as a monitoring system by measuring the induced field along the implant locally and limiting the RF exposure according to the worst case 'hot spot'.

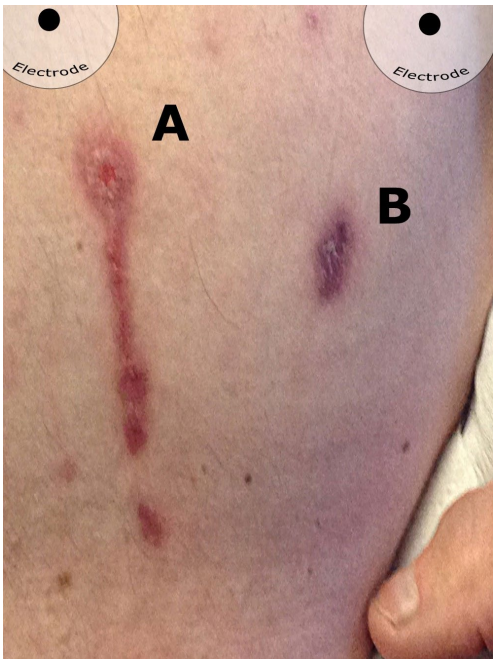

Figure 1-17 Image of third degree skin burns caused by ECG leads. Placement of the electrodes is indicated by the graphical overlay. The wounds are oriented in between the electrodes, which indicate burn caused by the ECG leads instead of the ECG electrodes. Note that deepest tissue damaged happened towards the tip of the leads [96].

1.3.2 B_0 Field: Projectile Effect

Main magnetic field B_0 is quite strong, 1.5T and 3T are the most common field strengths in clinical settings, and will attract any ferromagnetic object in the magnet room. As the ferromagnetic object experiences the attractive force, it will become a projectile if it is unsecured. Most incidents related to projectile effect are prevented by enforcing strict rules around the MRI suite, proper MRI safety labelling, limiting the number of people who can access the scanner room and mandating proper metal screening before entering the MRI room.

1.3.3 Gradient *dB/dt: Peripheral Nerve Stimulation*

Gradients, magnetic field change over time dB/dt, have become stronger with the advancements in MRI hardware technology. Rapid imaging sequences, such as echo planar imaging or EPI, requires very high values of dB/dt. A changing magnetic field will generate a current in the human body and sometimes in nerve and muscle tissues, resulting in a peripheral nerve stimulation, in which the patient experiences twitching and tingling. The maximum dB/dt values are restricted to prevent cardiac stimulation and pain.

1.4 Motivation and Objectives

1.4.1 Motivation

Motivation of this work is the development of a versatile sensing platform for safer and more effective MRI procedures. In order to cover most of the MRI safety issues described in section 1.2 and section 1.3, we aim to develop a sensing platform for two applications;

1) Local RF field sensing for the assessment RF induced heating on implants for diagnostic MRI.
2) Device tracking/profiling for real time image guidance in interventional MRI procedures.

1.4.2 Aims

Since we are investigating the sensor for two distinct applications, the sensor specifications for RF field sensing and device tracking are different from each other. The aims of the project are labelled and numbered in 4 different group: A, B, C and D. These labels will be referred throughout the text.

Group A aims are related to RF field sensing. An ideal RF field sensor for local field measurements must be capable of the following:

- Measurement of electric field component of RF field with high SNR (A1)
- Measurement of magnetic field component of RF field with high SNR (A2)
- High spatial resolution for fine mapping of current accumulation on implants (A3)
- Directional sensitivity to determine field orientation (A4)

Group B aims are related to device tracking under MRI. An ideal device tracking sensor for real time MRI guidance must be capable of the following:

- High visibility with real time fast imaging sequences (B1)
- Accurate and reliable localization (B2)
- Small form factor (B3)
- Easy integration with existing interventional devices (B4)

Group C aims are desired for any sensor and will be advantageous for both applications;

- High dynamic range (C1)

- Adaptability for different MRI systems (C2)
- Easy integration with the existing hardware and software of the MRI system (C3)
- Immune to electromagnetic fields – should not introduce extra RF induced heating (C4)
- Scalability for distributed marker schemes (C5)
- In-situ temperature measurement (C6)

Aim D is to development of a detailed model of the sensor in order to design and optimize the sensor for different applications – RF field sensing and device tracking- and different MRI system adaptations and achieve the aims A, B and C.

The sensors are designed for and tested with a 0.55 Tesla and 1.5 Tesla MRI systems. However, the framework presented can be easily applied to different field strength MRI systems.

1.4.3 Structure of the Thesis

This dissertation is organized as follows.

Chapter 1 introduces safety issues in medical MRI and outlines the motivation and aims of the research.

Chapter 2 introduces acousto-optic modulation as a sensor platform, explains the working principle of the acousto-optic sensor and describes an end-to-end model of the acousto-optic modulator. This chapter focuses on aim D for model development with model predictions.

Chapter 3 presents the a prototype for the acousto-optic modulator and backend opto-electronics for read-out. Moreover, model is validated through characterization test of the acousto-optic modulator. This chapter focuses on group C aims.

In Chapter 4, RF field sensing capability of the acousto-optic sensor is investigated. Different antennas are coupled with the acousto-optic modulator for electric and magnetic field measurements. Sensitivity, directivity and repeatability tests as well as field mapping on a pacemaker lead model are performed. This chapter focuses on group A aims.

In Chapter 5, the acousto-optic marker is integrated with a catheter and real time device tracking capability of the sensor is investigated in phantom and animal studies under MRI. This chapter focuses on group B aims.

Finally, Chapter 6 provides conclusions and a discussion of recommended future work for further improvement of the sensor.

CHAPTER 2. ACOUSTO-OPTIC SENSOR: WORKING PRINCIPLE AND ANALYSIS

2.1 Overview

Objective of the research was stated in the previous chapter as to develop a sensor platform for both RF field sensing and device tracking under MRI. This chapter introduces acousto-optic modulation for such application. The advantages of acousto-optic modulation are laid out, then the working principle of the chosen acousto-optic modulator are presented. Lastly, a model of the sensor is developed in order to optimize the sensor for different applications.

2.2 Acousto-Optic Modulation

Different antennas in the form of either loop or dipole, can be used for both RF field (electric field and magnetic field) sensing and device tracking. However, antennas require conductive transmission lines. In the previous chapter, we established that regardless of the sensor technology, long conductive lines need to be eliminated in order to eliminate RF induced heating. Dielectric transmission lines can be used instead of conducting electrical transmission lines to eliminate RF induced heating since dielectric materials do not absorb RF energy. As a dielectric transmission medium, optical fiber offers low insertion loss, mechanical flexibility, easy integration with electronics and most importantly, immunity to RF fields. However, a transduction scheme is needed to convert electrical signal to optical signal that will be guided within the optical fiber. A block diagram of such a system is given in Figure 2-1. Antenna picks up the RF field and generates an electrical signal. An

intermediate transduction mechanism converts the electrical signal into optical signal to be carried by an optical fiber out of the MRI scanner. Lastly, the optical signal needs to be converted back electrical signal by a photodetector.

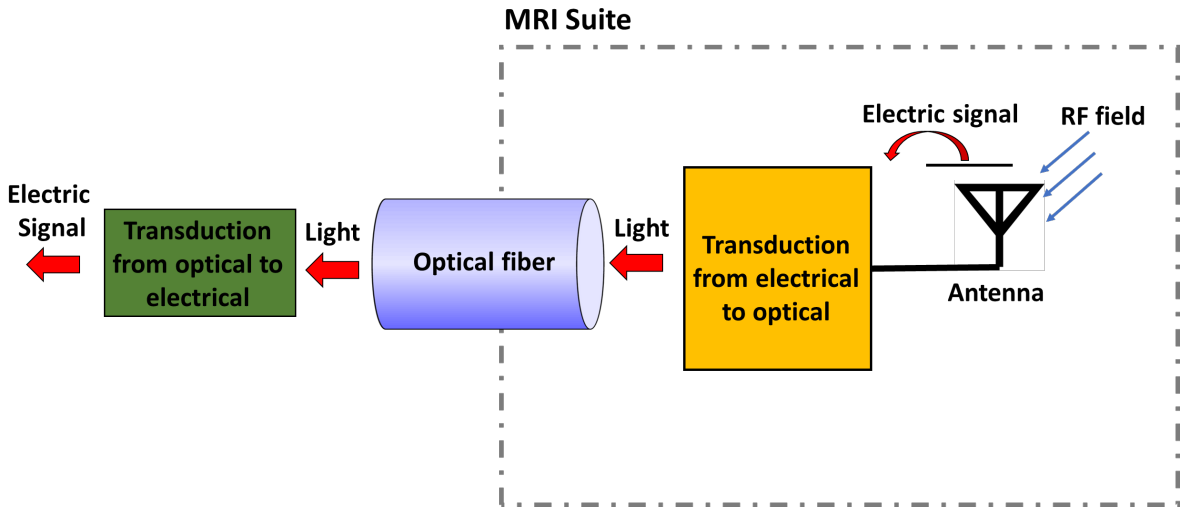

Figure 2-1 Block diagram of a RF field/device tracking sensor with fiber optic connection.

Electro optic modulation schemes have been proposed as an transduction mechanism in the literature [56], [57], [64]. A general topology for such an electro-optic modulator is given in Figure 2-2. Electro-optic modulator-based MRI sensors have three main components; antenna to pick up MRI signal, a light source that is modulated by signal from the antenna and a power up circuit. The optical modulation is achieved by modulating the bias current of a laser diode. Since this type of modulator is active, it requires external power. A separate optical fiber carries high intensity laser light into the sensor to power up the laser diode. A photovoltaic power converter is used for electricity generation. Since the optical modulator does not provide high SNR, the antenna requires to be resonant which

might lead to additional local RF heating exacerbated by the resonant antenna. Moreover, such a system results in long rigid structures due to packaging of complex electronics and optical alignments, which will hinder the clinical use. Larger size prevent the use of such a sensor for device tracking in iMRI.

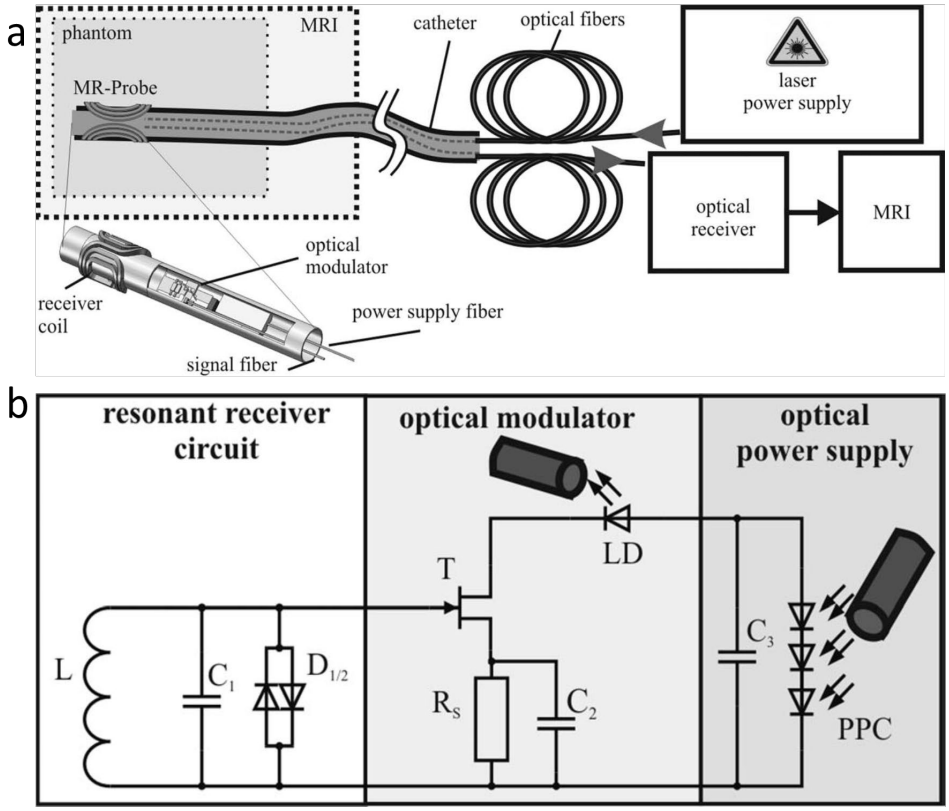

Figure 2-2 a) Concept of electro-optic modulator based sensor. Two fibers are applied in the catheter. One fiber is used to carry the signal information from the optical modulator and the other fiber for the optical power supply. b) Electrical circuit of an electro-optic modulator based sensor: The MR signal is received by the resonant circuit (L, C1). The signal is directly fed into the gate of the transistor T of the optical modulator. The signal is then transmitted by the laser diode (LD) to the optical receiver. The power is supplied by a photovoltaic power converter (PPC).

Another transduction mechanism can be realized with acousto-optic modulation. In acousto-optic modulation, optical properties of the medium are modulated using acoustic waves [97]. The electrical signal from the antenna can be used to generate acoustic signal via a piezoelectric transducer. Note that, the available MRI signal to the device tracking sensor will be quite low, in sub nW range, thus the acousto-optic modulator needs to be very sensitive. Performance of electro-optic based device tracking sensors suffer from low SNR whereas resonant nature of the piezoelectric transducers can be utilized for increased SNR. Since RF fields in MRI are in a narrow band, few kHz, around the Larmor frequency, high quality factor piezoelectric transducers with their resonances at the Larmor frequency can be used. If a passive acousto-optic modulator is used, power up circuits and other complex electronics will be eliminated resulting in a compact sensor package.

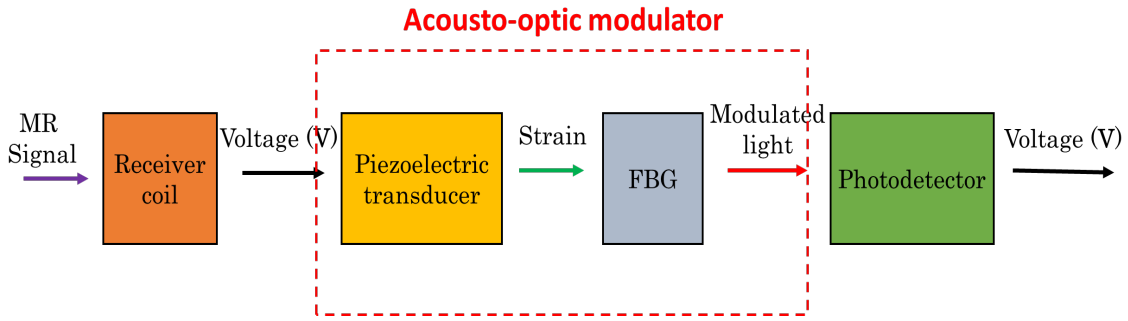

Figure 2-3 Block diagram of a RF field/device tracking sensor with acousto-optic modulator.

One type of acousto-optic modulation is interferometer utilizing reflectors and a reference beam [98]. Although interferometric transducers are easy to implement, they suffer from low sensitivity and mechanical stability. Another approach is employing fiber Bragg gratings (FBG) [99], [100][101]. FBG based acousto-optic modulators are small in

size; gratings are already embedded in the optical fiber, and acoustic wave generators such as piezoelectric layers can directly be deposited over the optical fiber [102]–[104]. FBG based sensors have been widely employed for ultrasound detection for the past few decades [100], [105]–[107]. FBGs can be used as hydrophones up to 100 MHz [108]. Moreover, multiple FBGs can be easily fabricated on a single fiber enabling multiple sensors on one optical fiber [109]. Block diagram of the acousto-optic transduction mechanism for an FBG based MRI sensor is given in Figure 2-3.

2.3 Working Principle of the Acousto-Optic Sensor

The block diagram of the proposed acousto-optic sensor is shown in Figure 2-4. Sensor system consists of four main components: an antenna to receive RF signal; a piezoelectric transducer to convert electrical signal to acoustic waves; an FBG sensor embedded in an optical fiber for acousto-optic modulation; and backend optoelectronics (light source and photodetector) for converting optical signal to electrical signal.

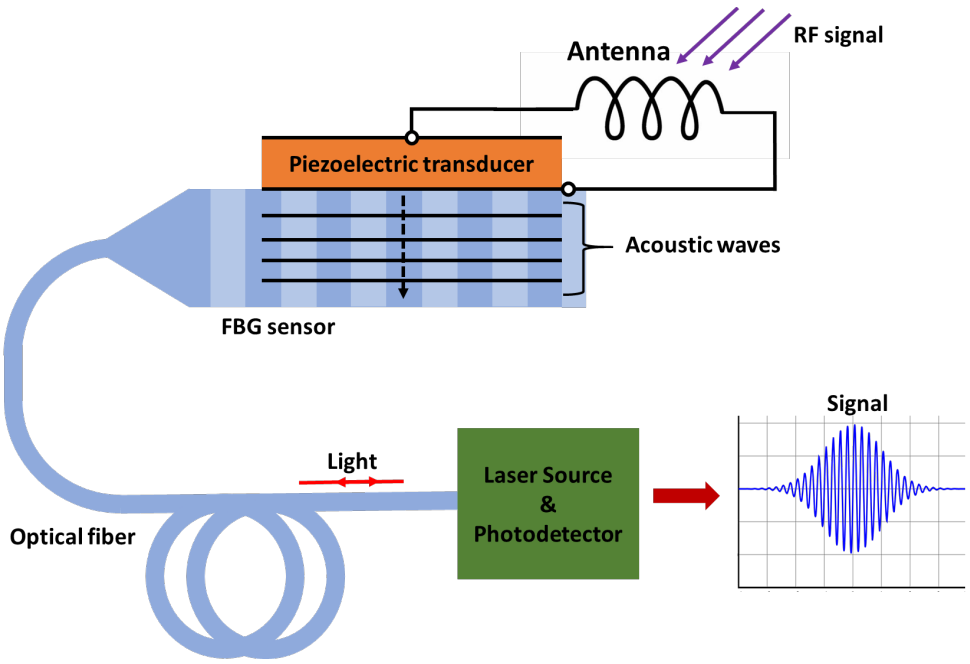

Figure 2-4 Block diagram of the FBG based acousto-optic catheter tracking sensor. Note that FBG sensor is embedded in the optical fiber, FBG part of the fiber is enlarged for illustrative purposes.

2.3.1 Fiber Bragg Gratings as Ultrasound Detectors

FBG is a type of distributed Bragg reflector; multiple mirrors in the fiber core are formed by periodic refractive index variations which generates a wavelength-specific dielectric mirror. Figure 2-5 illustrates the refractive index modulation and spectral response of an FBG. Wavelength of the reflected light from FBG, called Bragg wavelength, strongly depends on the periodicity of the mirrors and refractive index modulation depth in the fiber core. FBG based acousto-optic modulation relies on the Bragg wavelength change by acoustic waves. Reflectivity spectrum of the FBG, hence the Bragg wavelength,

shifts due to both periodicity change of Bragg grating and refractive index change by elasto-optic effect [110].

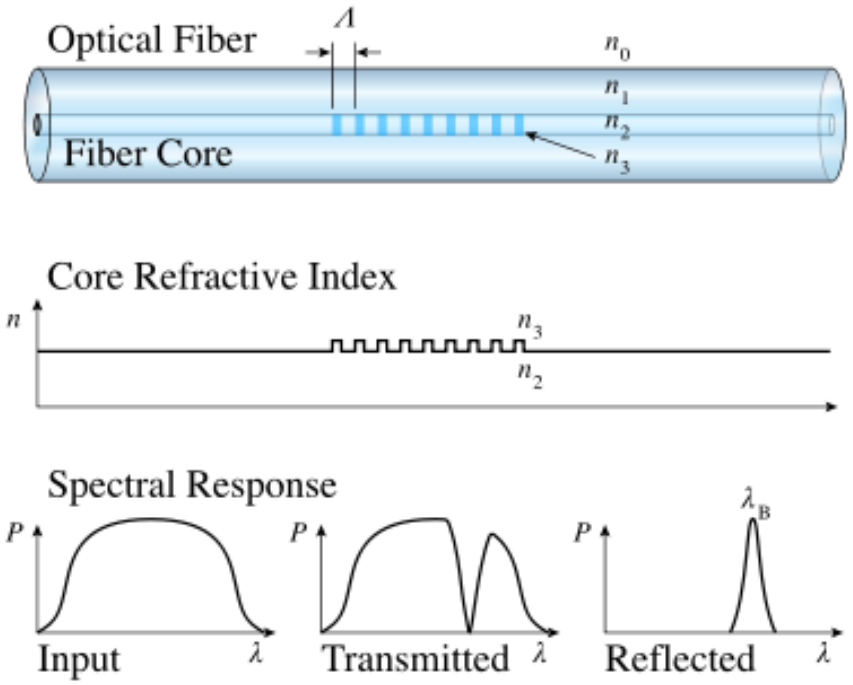

Figure 2-5 Schematic of FBG showing refractive index modulation and spectral response. [99]

The periodicity of an FBG can change with induced strain or temperature. Thus FBGs have been widely used and studied for strain and temperature measurements over the last few decades in nondestructive structural health monitoring [100], [111], [112] . When an ultrasonic wave is impinged on the FBG, the periodicity of the refractive index modulation changes resulting in a spectral shift, illustrated Figure 2-6. A detailed theoretical background on the ultrasound sensing with FBG is provided in the next section with a numerical model of FBG.

Since FBG is directly inscribed into the optical fiber, multiple gratings can be embedded onto a single optical fiber enabling multiplexed sensor topologies with wavelength division multiplexing [109]. In addition to intrinsic advantages of fiber optic sensors, FBG sensors offer amplitude/intensity fluctuation independent results due to spectrum based detection mechanisms [111], [113], [114], which ensures reproducible measurements despite the optical losses.

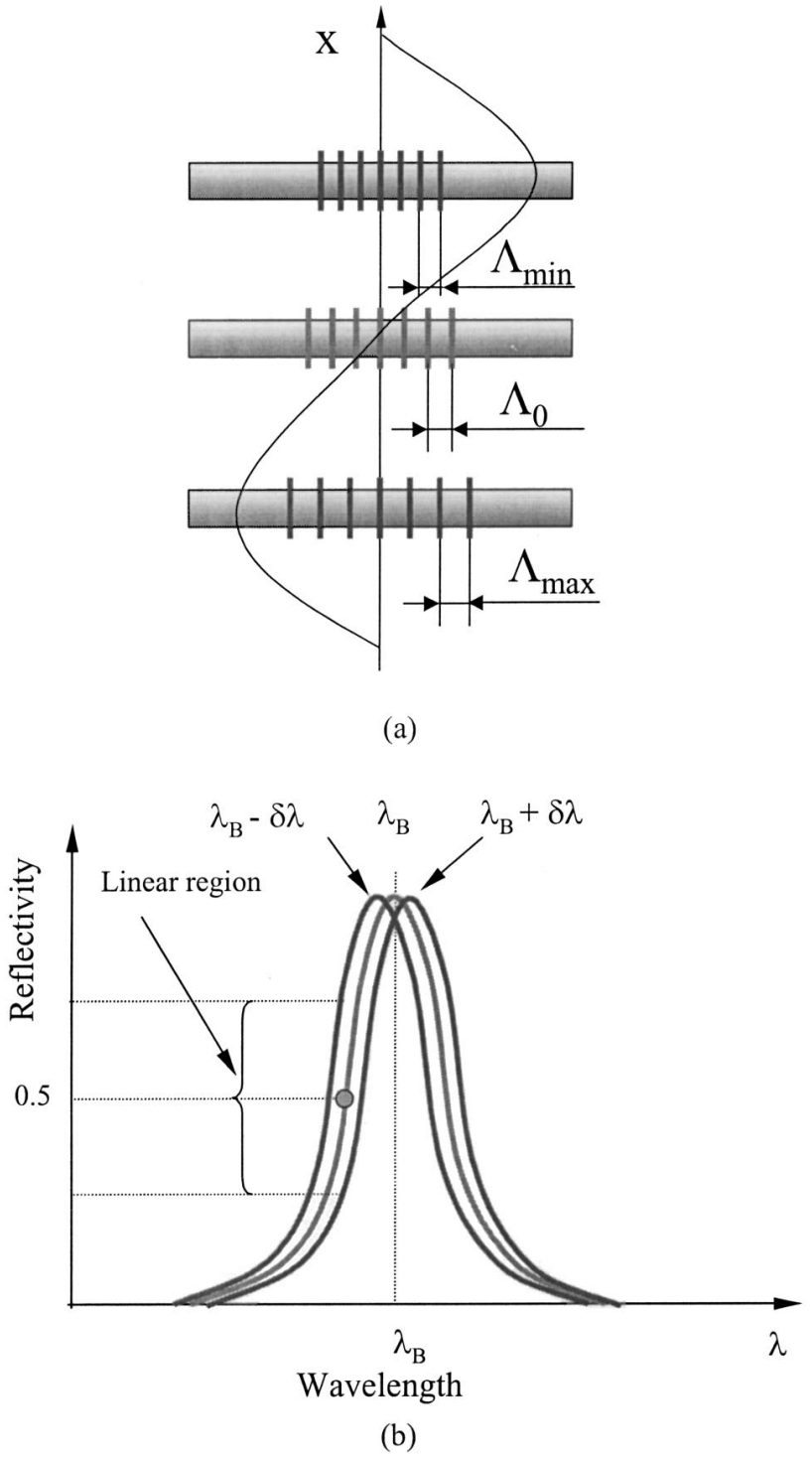

Figure 2-6 Ultrasound detection with FBG. (a) Modulation of the FBG period by acoustic pressure, and (b) corresponding shift of the FBG spectrum [113].

2.3.2 Optical Read-out Scheme

The most common read out scheme for FBG sensors employs a spectrometer and generates output based on the spectrum shift induced by applied strain or change in temperature. Spectrometer based approaches are well suited for multiplexed measurements where the inspection of the full response of the FBG is required [115], [116]. However, this approach is limited by the speed of the spectrometer, which limits the use of FBG sensors in higher frequency applications. In ultrasound detection and acousto-optic modulators, frequencies are in MHz range whereas strain levels induced by the acoustic waves are in μ-strain range or less [117]. Since the spectrum shift of the FBG is fast and amplitudes are small, the most sensitive region in the spectrum of the FBG is monitored instead of the whole spectrum [100], [118]. A narrow linewidth laser is used as input light source and wavelength of the laser is fixed in the middle section of the slope of the FBG spectrum, side slope detection scheme is shown in Figure 2-7. As the reflectivity spectrum of the FBG constantly shifts back and forth due to acoustic waves created, power of the reflected light from the FBG is modulated since laser light is fixed at a certain wavelength, the bias point on the side slope. Then, a photo detector captures the reflected light from FBG sensor.

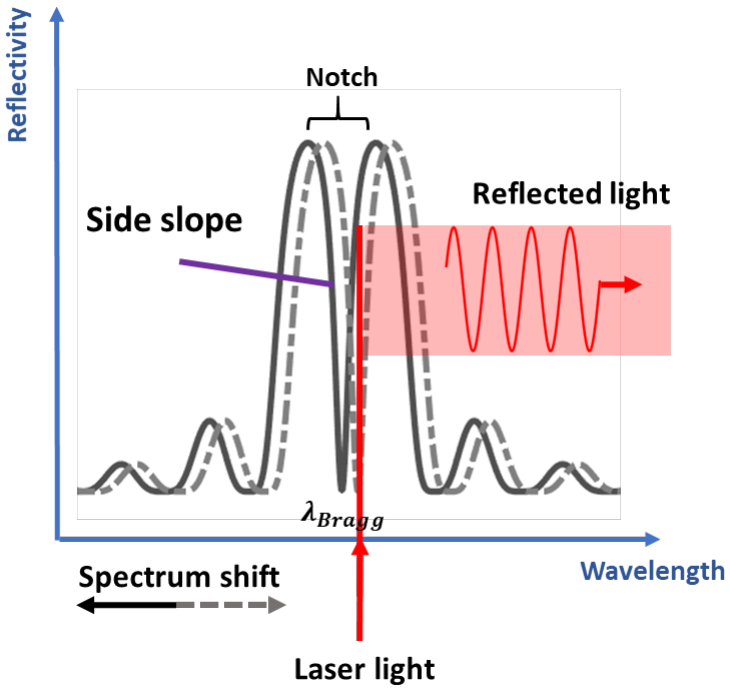

Figure 2-7 Side slope read-out scheme for the acousto-optic modulator.

2.4 Acousto-optic Modulator Model

A detailed model of the FBG sensor is required for the analysis and optimization of the sensor. Numerical methods are well suited for analysing optical characteristics of the FBGs whereas complex mechanical models utilize finite element analysis (FEA) tools. Thus, a composite model of the FBG utilizing both numerical and FEA methods is developed in order to investigate the linearity and sensitivity of the FBG as an ultrasound sensor, shown in Figure 2-8. Numerical methods, namely coupled mode theory (CMT) using transfer matrix method, is used for optical simulations. This method allows random grating profile and refractive index modulation as well as coupling with acoustic waves

and temperature fields. Mechanical response of the FBG to acoustic waves are simulated using a FEA tool. Two models are coupled through the pressure field within the fibre optic in the grating region. Then the photo detector sensitivity is used to calculate the output electrical signal.

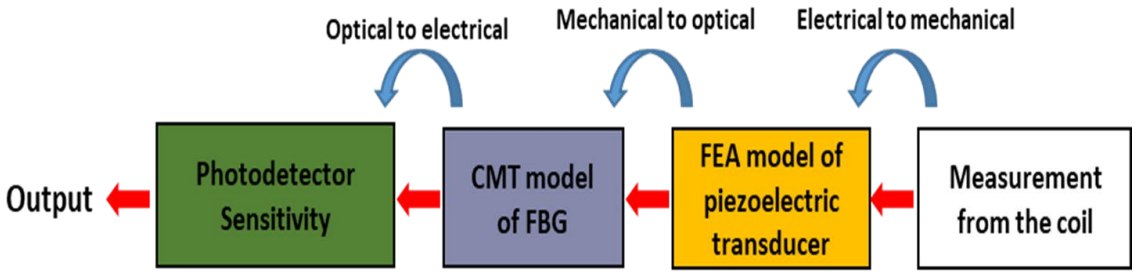

Figure 2-8 Composite model of the acousto-optic sensor.

2.4.1 FBG Model

FBG is manufactured by laterally exposing the core of a single-mode fiber to a periodic pattern of ultraviolet light, which alters the refractive index of the core according to the periodic pattern (Figure 2-10). In essence, FBG is a narrowband dielectric mirror with peak reflection occurring at the Bragg wavelength

$$\lambda_{Bragg} = 2n_{eff}\Lambda \tag{8}$$

Where n_{eff} is the effective refractive index of the fiber core and Λ is the grating period. π-phase shifted FBG (πFBG) has a jump in the periodicity in the middle of the grating. In essence, this discontinuity separates the grating into two highly reflective mirror

resulting in a high-quality factor Fabry Perot like cavity. This introduces a sharp notch in the middle of the reflection spectrum FBG (at λ_{Bragg}) resulting in steeper side slope. The spectrum difference and sensitivity comparison between a standard FBG and πFBG is shown in Figure 2-9 , enabling higher sensitivity. We used πFBGs for higher SNR measurements.

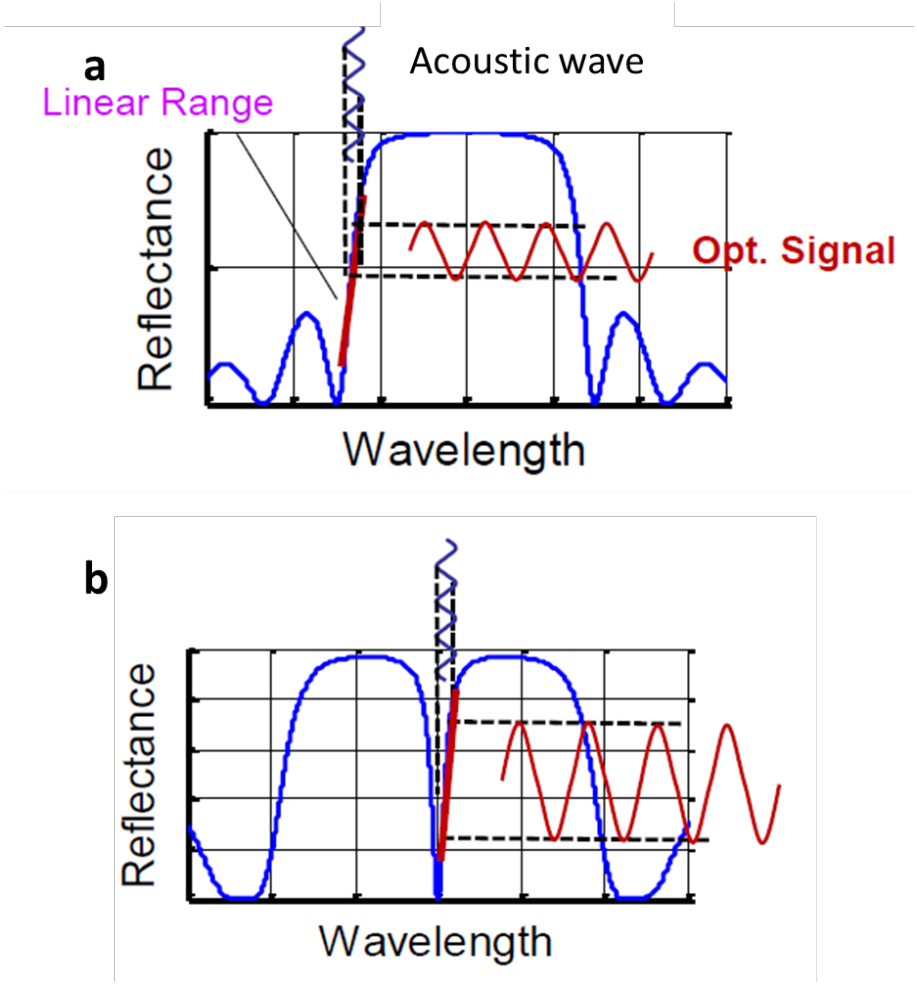

Figure 2-9 Reflectance spectrum and sensitivity difference between a) standard FBG and b) a π phase shifted FBG.

Reflection spectrum of the πFBG can be calculated using a coupled mode theory and transfer matrix method [119], [120]. πFBG with a total length of L is divided into smaller uniform sections with length of (Fig. 1a). Relations between forward-going modes, A_i, and backward-going modes, B_i, before and after each section can be represented by a 2x2 transfer matrix T_i.

$$\begin{bmatrix} A_i \\ B_i \end{bmatrix} = T_i \begin{bmatrix} A_{i-1} \\ B_{i-1} \end{bmatrix} = \begin{bmatrix} T_{11} & T_{12} \\ T_{21} & T_{22} \end{bmatrix} \begin{bmatrix} A_{i-1} \\ B_{i-1} \end{bmatrix} \tag{9}$$

Where T_i is defined as

$$T_{11} = cosh(\gamma_B \Delta z) - i\frac{\hat{\sigma}}{\gamma_B} sinh(\gamma_B \Delta z) \tag{10}$$

$$T_{12} = -i\frac{\kappa}{\gamma_B} sinh(\gamma_B \Delta z) \tag{11}$$

$$T_{21} = T_{12}* \tag{12}$$

$$T_{22} = T_{11}* \tag{13}$$

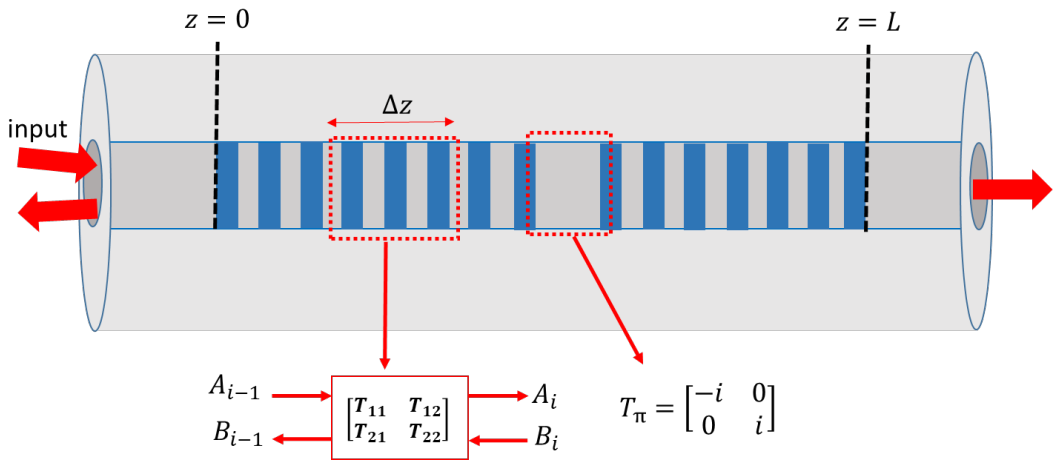

Figure 2-10 Schematic of a πFBG depicting transfer matrix method.

In Eq. (3) and (4), $\hat{\sigma}$ is dc self-coupling coefficient, κ is ac coupling coefficient and $\gamma_B = \sqrt{\kappa^2 - \hat{\sigma}^2}$. Coupling coefficients for FBG is given as follows

$$\hat{\sigma} = \delta + 2\pi n(z)/\lambda \tag{14}$$

$$\kappa = \pi n(z)/\lambda \tag{15}$$

Where $\delta = 2\pi n_{eff}(1/\lambda - 1/\lambda_D)$ is detuning parameter, λ wavelength and $\lambda_D = 2n_{eff}\Lambda(z)$ is design wavelength and n is local refractive index. A single transfer matrix $T(\lambda)$ can be defined for the overall grating by multiplying individual transfer matrices T_i at each wavelength. Phase shift in the grating can be introduced into the model by

$$T_\pi = \begin{bmatrix} -i & 0 \\ 0 & i \end{bmatrix} \lambda \tag{16}$$

Hence the system matrix T will become

$$\begin{bmatrix} A_{(z=L)} \\ B_{(z=L)} \end{bmatrix} = T_M \cdot T_{M-1} \cdots T_\pi \cdots T_2 \cdot T_1 \begin{bmatrix} A_{(z=0)} \\ B_{(z=0)} \end{bmatrix} = T \begin{bmatrix} A_{(z=0)} \\ B_{(z=0)} \end{bmatrix} \tag{17}$$

Where $A_{(z=0)}$ and $B_{(z=0)}$ are complex modes at the start of the grating, $A_{(z=L)}$ and $B_{(z=L)}$ are complex modes at the end of the grating and $M = L/\Delta z$. Lastly, by applying boundary conditions $A_{(z=0)} = 1$ and $B_{(z=0)} = 0$ are in Eq. 10, amplitude and power reflection coefficients can be calculated as $\Gamma(\lambda) = -T_{21}/T_{22}$ and $r = |\Gamma(\lambda)|^2$ respectively.

When the πFBG is impinged by an acoustic wave, refractive index n and grating period Λwill change due to elasto-optic effect. Normalized refractive index Δn and relative grating period changes $\Delta\Lambda$by an acoustic wave with pressure field $(z,)$ can be expressed as follow

$$\frac{\Delta n(z,t)}{n_{eff}} = n^2 \frac{P(z,t)}{2E}(1-2\nu)(2P_{12}+P_{11}) \tag{18}$$

$$\frac{\Delta\Lambda(z,t)}{\Lambda} = -\frac{P(z,t)}{E}(1-2\nu) \tag{19}$$

where P_{11} andP_{12} are elements of the strain-optic tensor, E is Young's modulus and ν is Poisson's ratio. Since coupling coefficients $\hat{\sigma}$ and κ depend on refractive index n and grating period Λ, new reflection spectrum of the grating can be calculated by plugging Eq.

(11) and (12) into (7) and (8). When choosing Δz, acoustic wavelength and grating length should be taken into consideration such that $\Lambda \ll \Delta z \ll \lambda_{acoustic}$ where $\lambda_{acoustic}$ is acoustic wavelength inside the fiber in order to satisfy uniformity assumption.

2.4.2 Piezoelectric Model

FEA is used for modelling of the piezoelectric transducer and pressure calculations within the optical fiber. Optical fiber is modelled as a silica cylinder in COMSOL Multiphysics platform since the mechanical properties of both core and cladding of the fiber are the same Figure 2-12. The piezo-electric transducer was constructed within the piezoelectric module of COMSOL.

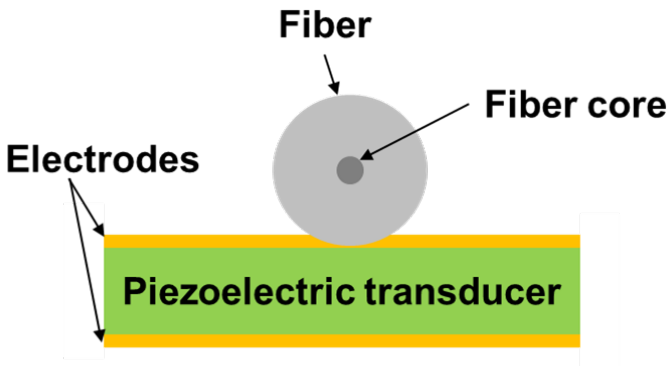

Figure 2-11 FEA model of piezoelectric transducer and optical fiber with FBG embedded in its fiber core.

Voltage output from the antenna and the input impedance of antenna are used as input to the piezoelectric model. The coupling between the piezoelectric transducer and the optical fiber is simulated via a Hertzian contact with no losses. Losses was added to the piezoelectric transducer model to account for fabrication imperfections and loading of the

piezoelectric transducer by glue used for attaching the optical fiber. In order to minimize the acoustic wave reflections at the fiber ends, a low reflecting boundary condition is applied on both fiber ends. The pressure field in the core of the fiber induced by the external acoustic wave is calculated and inserted as *P(z,t)* into eq. (11) and (12), shown in Figure 2-12. Note that, any arbitrary pressure field distribution can be used as an input for the model as long as Δz is adequately smaller than smallest acoustic wavelength.

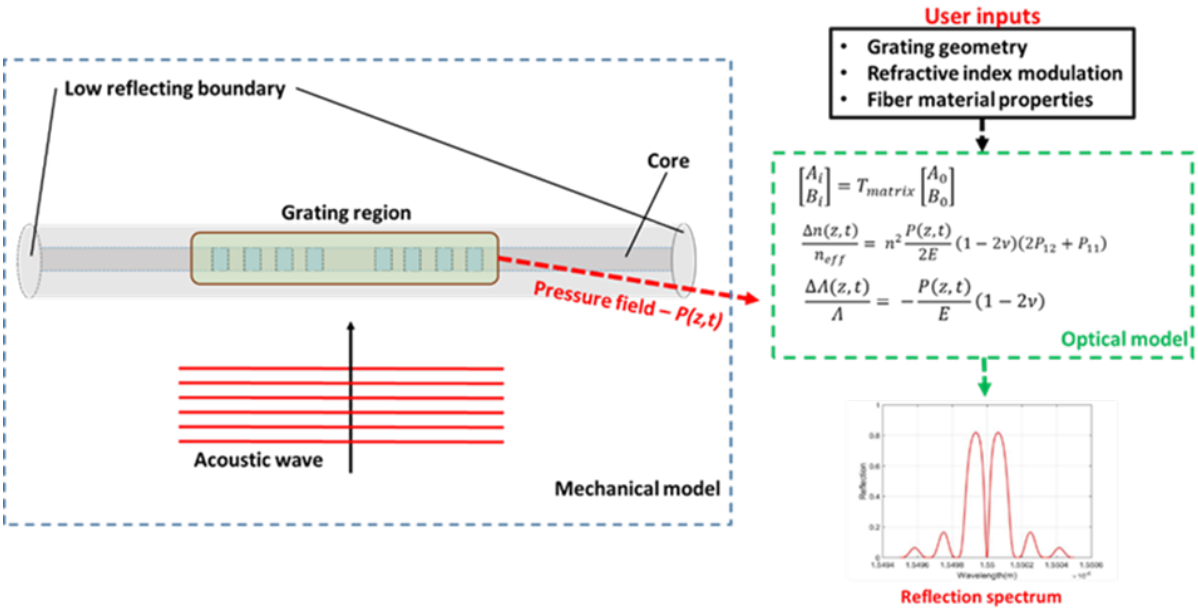

Figure 2-12 Piezo electric model used for the stress/strain distribution on the optical fiber core region of the FBG grating.

2.4.3 Simulations

Initially, we used the FBG model for the design of different FBGs. As high performance opto-electronics are readily available for 1550nm wavelength due to its

extensive use in telecommunication, Bragg wavelength for all the FBGs was set at 1550nm. Intrinsic parameters of a fused silica optical fiber are used for all the simulations.

Shorter grating length is desired for especially device tracking in order to reduce the size of the sensor. However, as there is a compromise between the grating length and the sensitivity of the FBGs. Three different π-FBGs with different grating lengths are given in Figure 2-13. The performance of the FBG is substantially is reduced with shorter grating length of 4mm. Even though, 16mm grating length provides the steepest side slope, we think the packaging of such a sensor will be a challenge. Thus, we opted for a grating length of 8mm as a good compromise between sensitivity and size.

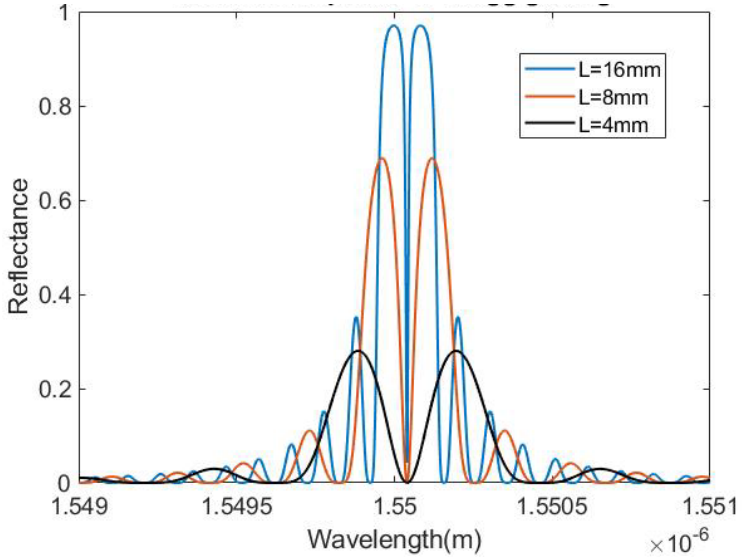

Figure 2-13 Simulation of reflection spectrums of π-FBGs for grating lengths of 4mm, 8mm and 16mm.

A uniform FBG and phase shifted FBG was simulated with the same design parameters. A comparison of the reflection spectrum of those FBGs are given in Figure 2-14. The side slope of the phase shifted FBG is steeper than standard FBG as expected. Since high SNR is required for both device tracking and RF field sensing, we have chosen a phase shifted FBG topology. We simulated and designed two π-FBGs with the following parameters, given in Table 2-1.

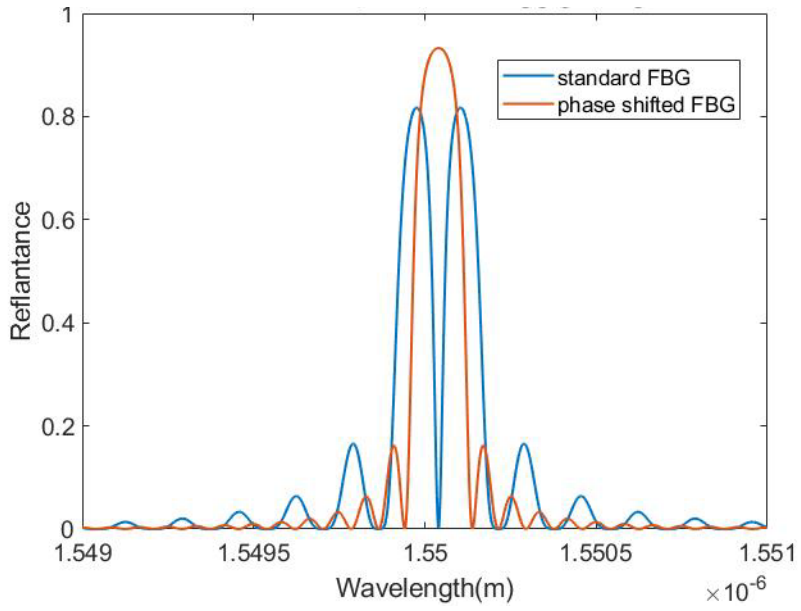

Figure 2-14 Simulation of reflection spectrums for a standard and phase shifted FBG.

.

Table 2-1 Simulation parameters for π-FBG-1 and π-FBG-2.

	π-FBG-1	π-FBG-2
Grating type	π-phase shifted	
Bragg wavelength	1550 nm	
Bandwidth (FWHM)	2 pm	0.4 pm
Grating length	8 mm	8 mm
Refractive index modulation	3.7×10^{-6}	4.85×10^{-6}
P11	0.113	
P12	0.252	
Poisson's ratio	0.25	
Cladding diameter	125 μm	
Young's modulus	70 GPa	
Λ	528nm	
Δz	10 μm	
$\lambda_{acoustic}$	94 μm – 250 μm	

Ideally, very narrow notch widths are desired for higher sensitivity, however fabrications of sub-pm notch width FBGs are very challenging. Thus, spectral bandwidth of the center notch of the π-FBGs were designed as 2 pm (250 MHz) in π-FBG-1 for easier fabrication and 0.4 pm (50 MHz) in π-FBG-2 for higher sensitivity. In uniform FBGs, bandwidth and refractive index modulation are linearly proportional, an example simulation is given in Figure 2-15. However, bandwidth and refractive index modulation have an exponential relationship. Refractive index modulation of 3.7×10^{-6} is required for π-FBG-1 and refractive index modulation of 4.85×10^{-6} is required for π-FBG-2. Even though, the bandwidth is 5 times narrower in π-FBG-2, refractive index modulation is only increased by 1.31.

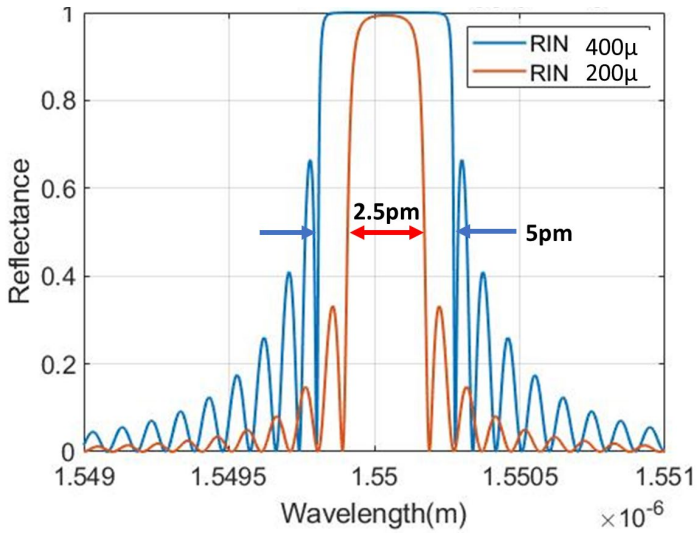

Figure 2-15 A comparison between bandwidth two uniform FBGs with different refractive index modulations (RIN).

Reflection spectrums for π-FBG-1 and π-FBG-2 around the central notch are given in Figure 2-16. Side slope of π-FBG-2 is 5 times steeper than side slope of π-FBG-1. Thus, a factor 5 increase in sensitivity is expected when π-FBG-2 is used.

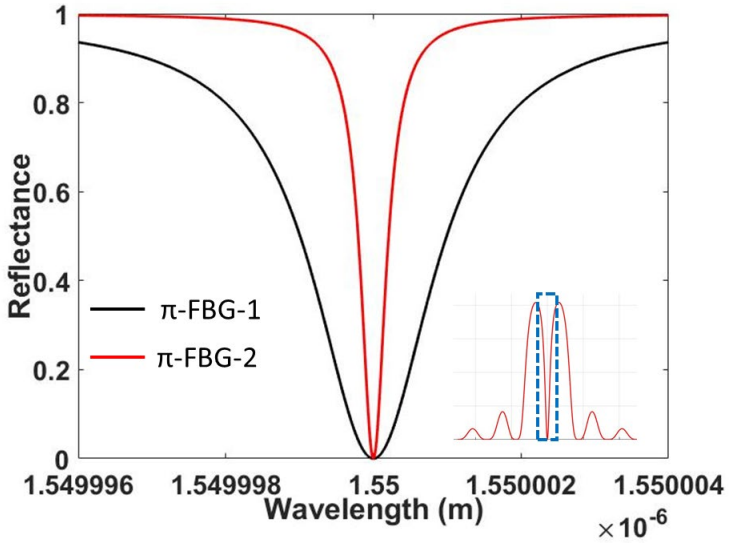

Figure 2-16 Reflection spectrums of π-FBG-1 and π-FBG-2 around the central notch.

The pressure sensitivity of the FBG sensors are calculated by using applying a uniform pressure across the grating length. Optical modulation depths of 3.2% and 1.59% per kPa are calculated for π-FBG-1 and π-FBG-2. Time domain simulation results for an input pressure field of 1kPa at 63.86MHz are shown in Figure 2-17.

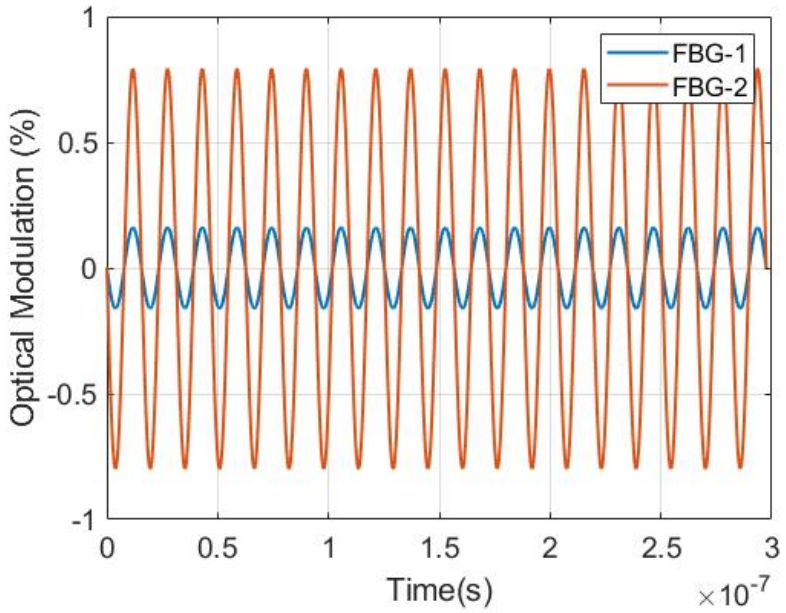

Figure 2-17 Time domain simulation results for π-FBG-1 and π-FBG-2 when an input pressure field of 1kPa at 63.86MHz is applied.

A summary of calculated pressure sensitivities for π-FBG-1 and π-FBG-2 is given in Table 2-2. Note that, the output voltage of the photodetector is assumed 10V at the maximum reflectance.

Table 2-2 Pressure sensitivity of the FBG sensors for 10V maximum output voltage

FBG type	Pressure sensitivity
π-FBG-1	16 mV/kPa
π-FBG-2	79 mV/kPa

The piezoelectric model is first used for impedance calculation of the piezoelectric crystals. A comparison between simulation results and measurements of an unloaded PZT5A crystal with a size of 1mm x 2mm are given in Figure 2-18. Impedance measurements of the actual transducer is used for determining and fine tuning of the loss parameters in COMSOL. Multiple peaks in the measurements are mostly caused by backing material. The higher capacitance in the imaginary part is caused by the improper calibration of the network analyzer as we don't have a calibration kit suitable for the testing of this kind of devices.

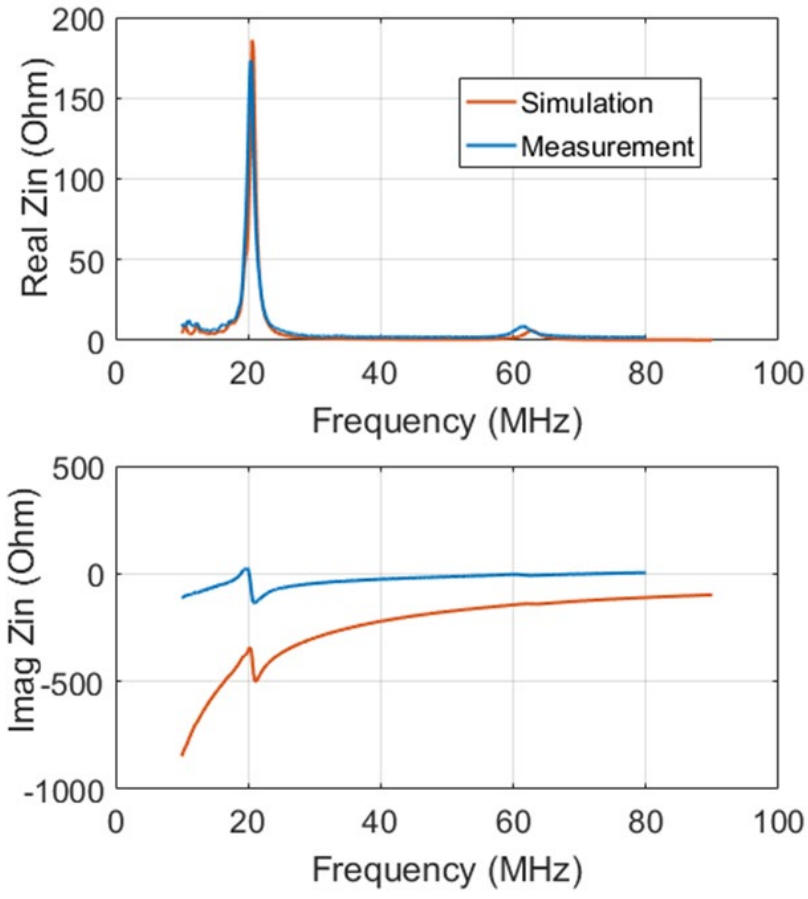

Figure 2-18 Simulated and measured input impedance of an PZT5A crystal.

Then, the pressure coupling from the piezoelectric transducer to fiber optic was simulated. Typical pressure distribution within optical fiber – piezoelectric transducer assembly due to acoustic waves generated by the piezoelectric transducer with pressure distribution along the red line passing through the fiber core is given in Figure 2-19. Note that the pressure at the fiber core is lower than the maximum pressure.

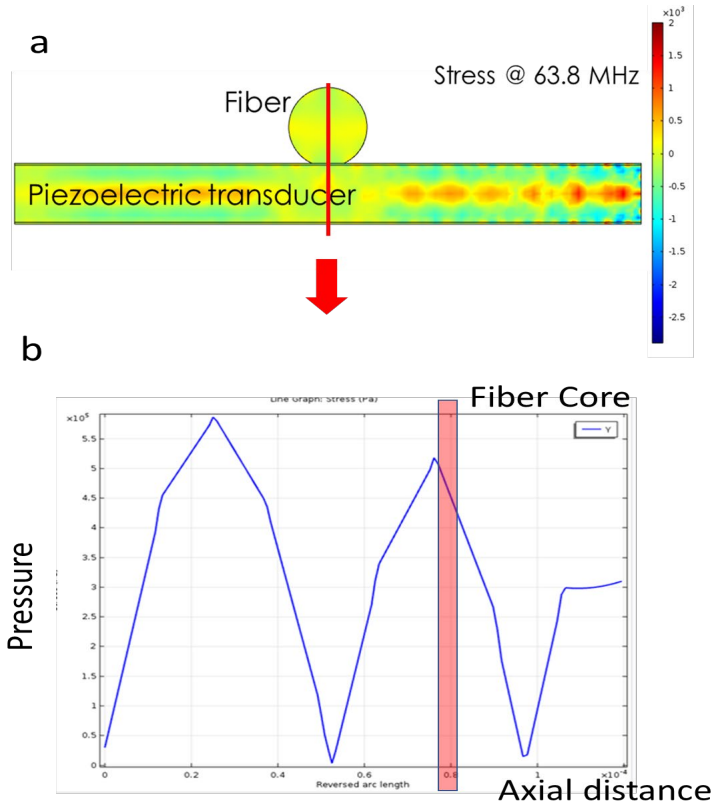

Figure 2-19 a) Typical pressure distribution within the optical fiber – piezoelectric transducer assembly due to acoustic waves generated by the piezoelectric transducer. b) Pressure distribution along the red line passing through the fiber core. Note that the pressure at the fiber core is lower than the maximum pressure.

As in can be seen in Figure 2-19a, only small portion of the piezoelectric transducer is touching optical fiber, thus most of the input power is wasted. Instead of using a bulk piezoelectric material, a piezoelectric thin film can be coated on the optical fiber, schematic is shown in Figure 2-20. This way, pressure field generated by the piezoelectric transducer can be coupled to the FBG more efficiently. Moreover, the size of the acousto-optic modulator will be further reduced to the size of the optical fiber, 125 μm in diameter.

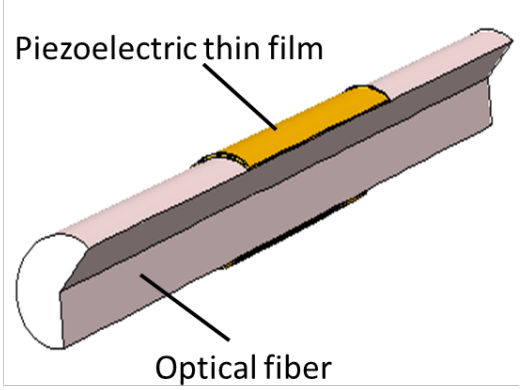

Figure 2-20 Schematic of an acousto-optic modulator coated with thin film piezoelectric transducer.

The model is used for the simulation of an acousto-optic modulator coated with thin film piezoelectric transducer, shown in Figure 2-21.

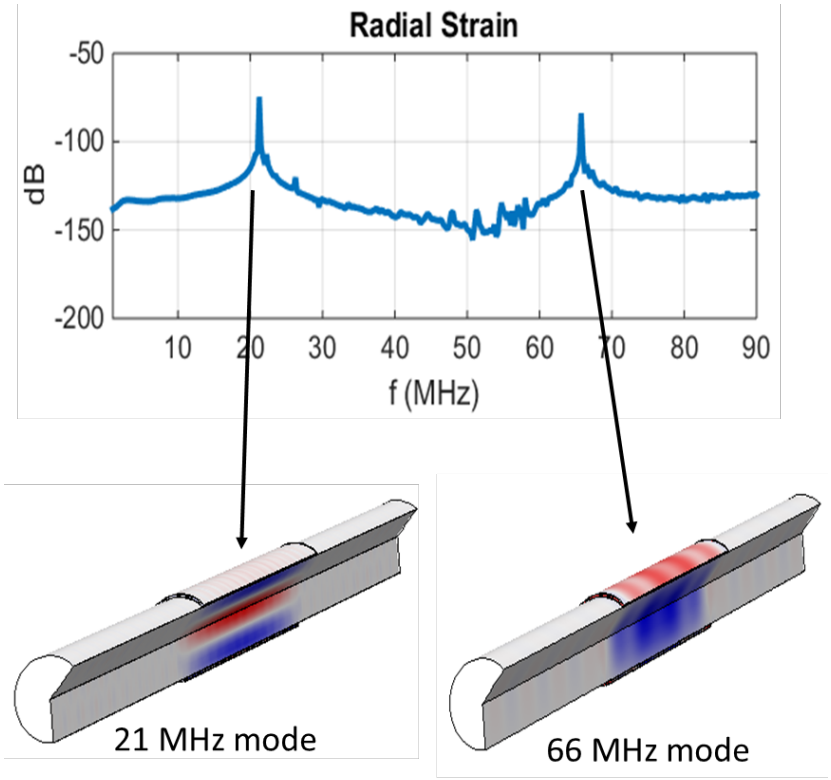

Figure 2-21 Simulation result showing multiple mechanical resonances for an optical fiber with a thin ZnO piezoelectric layer.

There are two distinct modes with resonances at 21MHz and 66MHz which are closer to Larmor frequencies of 0.55T (23.6MHz) and 1.5T MRI (63.86MHz) systems. The resonance frequency easily tunable by adjusting the piezoelectric layer thickness and optical fiber diameter. An optimized acousto-optic is designed using the model and the stress distribution along the fiber core for a thin film ZnO coated optical fiber optimized for 63.86 MHz is given Figure 2-22.

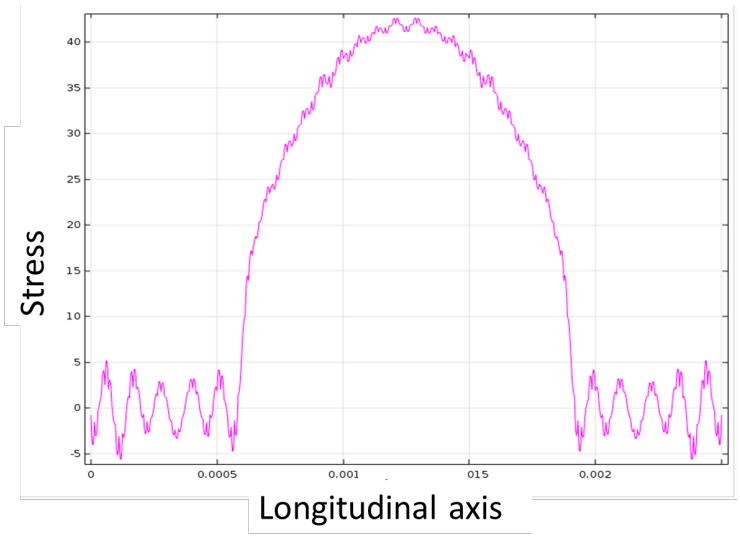

Figure 2-22 Stress distribution along the fiber core for a thin film ZnO based acousto-optic modulator optimized for 63.86 MHz.

Simulation results shows that a maximum pressure of 55 kPa is generated at the fiber core when an input of 1V is applied across a bulk $LiNbO_3$ piezoelectric transducer at 63.86MHz. However, an optimized acousto-optic sensor with a thin film ZnO coating will generate 4.3 MPa at the fiber core resulting in a 2 orders of magnitude sensitivity improvement. A summary of the electro-mechanical conversion rates for the acousto-optic modulator with bulk and optimized thin film coated piezoelectric transducers is given in Table 2-3.

Table 2-3 Electro-mechanical conversion rates for the acousto-optic modulator with bulk and optimized thin film coated piezoelectric transducers at 63.86 MHz

Transducer configuration	Electro-mechanical conversion rate
Bulk piezo ($LiNbO_3$)	55 kPa/V
Optimized thin film (ZnO)	4.3 MPa/V

A gain for the acousto-optic modulator can be calculated combining the pressure sensitivity of the FBG sensors and the electro-mechanical conversion rates of the piezoelectric-FBG pair. A summary of acousto-optic conversion gains for the acousto-optic modulator in different combinations of FBG sensors and piezoelectric transducers is given in Table 2-4.

Table 2-4 Acousto-optic conversion gains for the acousto-optic modulator in different combinations of FBG sensors and piezoelectric transducers.

	π-FBG-1	π-FBG-2
Bulk piezo ($LiNbO_3$)	1.76 V/V	8.75 V/V
Optimized thin film (ZnO)	137.6 V/V	683.7 V/V

2.5 Summary

This chapter introduced FBG based acousto-optic modulators as a transduction mechanism between an antenna and the optical fiber. Working principle of the acousto-optic modulator is explained. A model for the acousto-optic sensor is developed and effects of various design parameters on the sensor performance are investigated through simulations. Hence, aim D is achieved and feasibility of aim C2 is shown.

The major points of this chapter are listed as follows:

- Proposed sensor system consists of four main components: an antenna to receive RF signal; a piezoelectric transducer to convert electrical signal to acoustic waves; an FBG sensor embedded in an optical fiber for acousto-optic modulation; and backend optoelectronics (light source and photodetector) for converting optical signal to electrical signal. The resonant nature of the piezoelectric transducer can be used to increase overall SNR of the system while limiting the bandwidth.
- Side slope read-out scheme can be used for detecting small pressure amplitudes at high frequencies.
- A hybrid model of the acousto-optic modulator is developed. A numerical model of FBG is derived using coupled mode theory and transfer matrix methods whereas piezoelectric transducer is modeled using FEA. Models are coupled through pressure field at the fiber core.
- Effect of different parameters on FBG design is investigated through simulations. As phase shifted FBGs resulted in higher sensitivities, π-FBGs

with bandwidths of 0.4pm and 2pm are designed. Optical modulation depths of 3.2% and 1.59% per kPa are calculated for FBGs, respectively.

Pressure fields within the FBG induced by bulk and thin film piezoelectric transducers are simulated. 2 orders of magnitude sensitivity improvement is achieved by optimizing the thin film piezoelectric transducers for Larmor frequency.

CHAPTER 3. PROTOTYPING AND CHARACTERIZATION OF THE ACOUSTO-OPTIC MODULATOR

3.1 Overview

Working principle of the acousto-optic sensor was presented in the previous chapter with a model of the sensor in order to optimize the sensor for different applications. This chapter focuses on the sensor prototype and its characterization. First, the specifics of sensor prototype and components are given. The back-end opto-electronics used for optical read out are explained in detail. Then, the model is verified through sensitivity and linearity analysis. Lastly, noise analysis of the acousto-optic modulator is performed.

3.2 Acousto-optic Modulator Prototype

Proof of concept prototypes were built for two different field strength MRI scanners: a prototype 0.55 Tesla MRI scanner (Aera, Siemens Healthineers Erlangen) and clinical 1.5 Tesla MRI scanner (Aera, Siemens Healthineers Erlangen). The Larmor frequencies are 23.65MHz for 0.55T scanner and 63.86 MHz for 1.5T scanner. The prototype consists of two main systems; an acousto-optic modulator probe and a back-end optoelectronic system for system control and MRI integration. Overall system schematic is given in Figure 3-1.

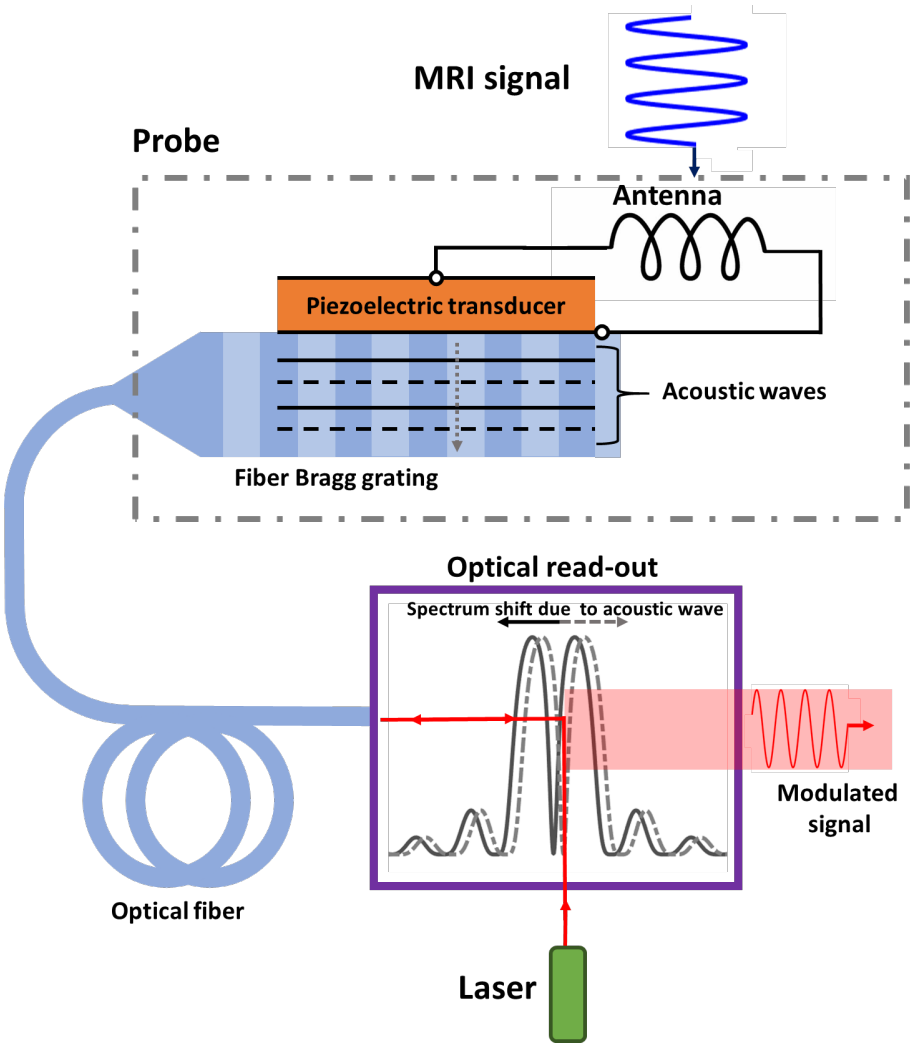

Figure 3-1 Schematic of the whole sensor system with distal end probe and the optical read-out unit.

3.2.1 Acousto-optic Probe

Acousto-optic probe consists of a receiver antenna for RF signal pickup, a piezoelectric transducer and a FBG sensor for acousto-optic modulation. Fig. 2(b) illustrates the acousto-optic probe designed for the prototype.

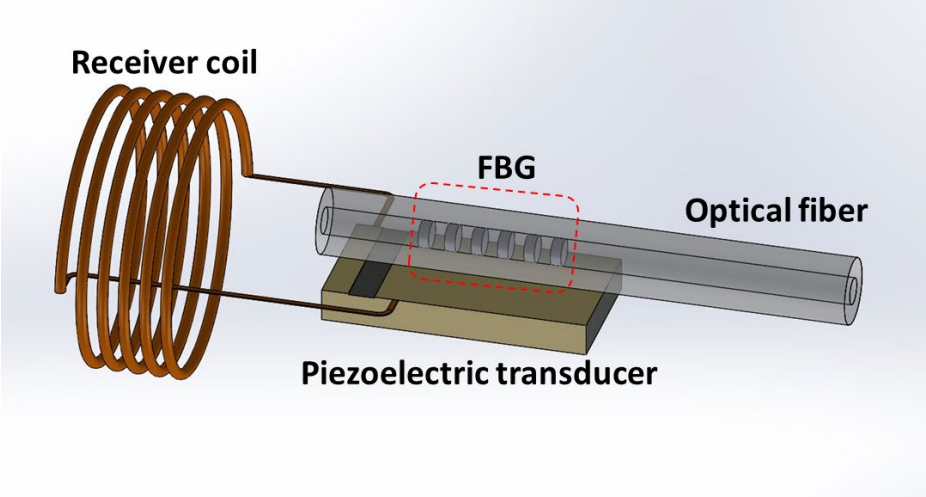

Figure 3-2 illustration of the acousto-optic probe showing receiver coil, piezoelectric transducer and FBG sensor.

Piezoelectric transducers have highest electro-mechanic coupling efficiency when operated at around their resonance frequency [121]. Resonance frequency of thickness mode piezoelectric transducers are determined by their thickness, which is around 20-30 micrometre range for common piezoelectric materials for 63.86 MHz. Since this is difficult to fabricate and handle mechanically, a commercially available 100-µm thick piezoelectric transducer (Boston Piezo Optics Inc., MA, USA). The measured electrical impedance of the particular piezoelectric transducer is shown in Figure 3-3, which clearly shows the first and third harmonic mode resonances. Note that, these piezoelectric transducers are custom made and there is a huge variety between the sensors resulting in resonance and impedance variations up to ±15%. Piezoelectric transducers with first resonances around 23 MHz are used for 0.55T scanner and piezoelectric transducers with a resonance frequency of 21 MHz are used at its third harmonic resonance frequency of around 63 MHz for 1.5T

scanner. Electro-mechanic coupling efficiency is significantly reduced when the piezoelectric transducer is driven at its third harmonic.

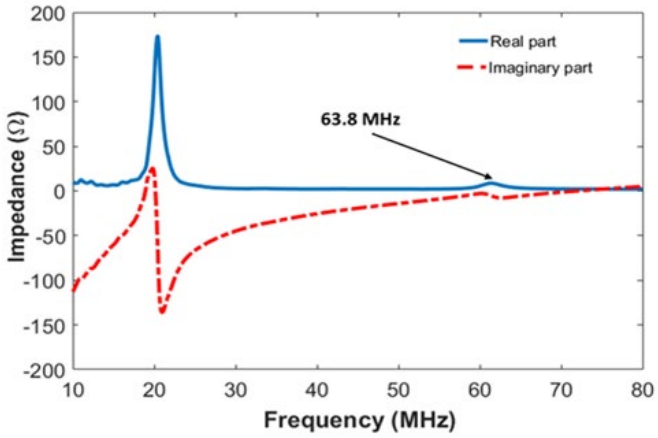

Figure 3-3 Measured electrical input impedance of the PZT5A piezoelectric transducer used for 1.5T MRI system.

Two types of piezoelectric transducers were used; PZT5A and $LiNbO_3$. The width of the piezoelectric transducers is 1mm and length of 2mm and 5mm were used. 5mm transducer allows easier fabrication due to its larger size. A wrap around electrode configuration was used so that bottom side of the piezoelectric transducer can be attached onto flat surface. All components at the probe end are held together by a printed circuit board (PCB) piece for easy handling. The electrodes were connected to connections on the PCB via gold wire bonds, shown in Figure 3-4.

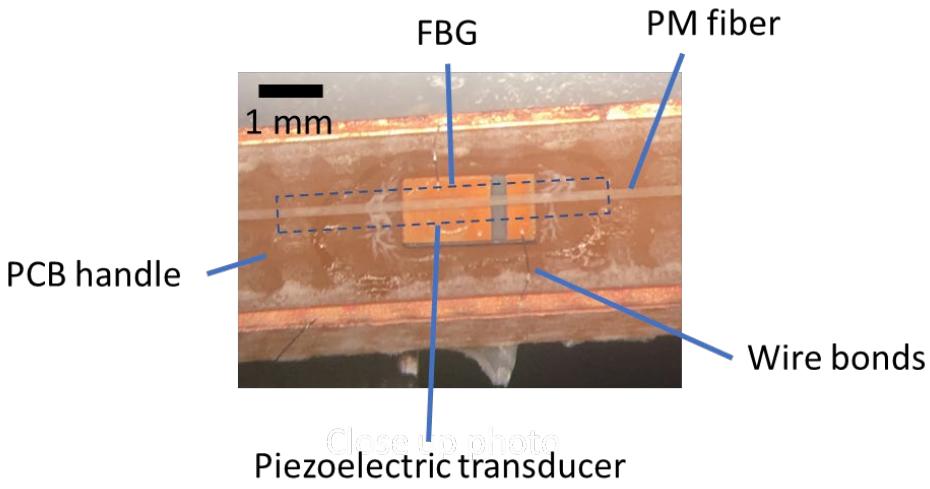

Figure 3-4 Close up photo of the acousto-optic modulator assembly on the PCB handle.

Acoustic waves created by the piezoelectric transducer are coupled to FBG sensor via a rigid, Hertzian contact; FBG section of the fiber is attached to the piezoelectric transducer with low viscosity cyanoacrylate (3M Company, MN, USA). Bragg wavelength is chosen as 1550 nm because of its extensive use in telecommunication. In order to increase sensitivity, π phase shifted FBG was used in this study [114], [122], [123]. Both of the phase shifted FBGs designed in Chapter 2 are fabricated and used in the prototype (Teraxion Inc., Quebec, Canada). The single mode optical fiber used at the distal end is a single mode polarization maintaining fiber with a cladding diameter of 125 µm and acrylic protection layer of 250 µm. Overall grating length for both πFBGs are 8 mm with 2 pm or 250MHz (π-FBG-1) and 0.4 pm or 50MHz (π-FBG-2) notch bandwidth at FWHM. The πFBGs were fabricated on a polarization maintaining (PM) fiber so that there are two Bragg wavelengths due to slightly different refractive index in the slow axis and fast axis of PM

fiber. In this work, only the slow axis mode was excited with a laser source polarized in slow axis.

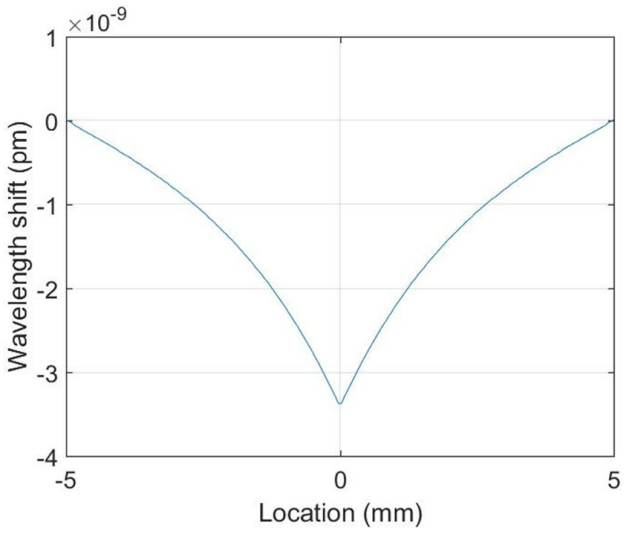

Figure 3-5 Sensitivity of π-FBG along the fiber length with phase shift location at 0mm.

The sensitivity of the phase shifted FBG changes along the grating length; most sensitive at the phase shift with decaying sensitivity towards the edge of the grating. Sensitivity pattern of a π phase shifted FBG is simulated in the model, shown in Figure 3-5. Thus, location of the piezoelectric transducer is crucial. An assembly rig with mechanical translation stage was used for precise alignment of the FBG and the piezoelectric transducer, shown in Figure 3-6. The piezoelectric transducer on a PCB holder is attached to a 3 axis translational stage whereas the optical fiber is attached to a rotational stage. Alignment is monitored by a microscope. Maximum mechanical coupling

between the FBG and the piezoelectric transducer is assured by scanning the FBG area for maximum optical output when the piezoelectric transducer is driven constantly.

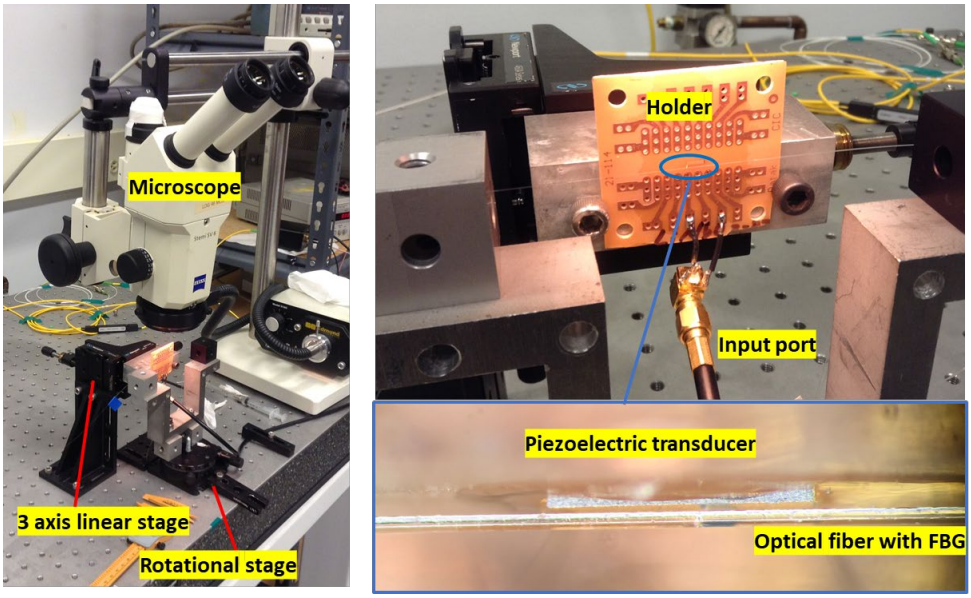

Figure 3-6 Alignment rig used for the assembly of acousto-optic modulator

Receiver antenna can be either a short dipole or loop antenna depending on the application. Short dipoles are more sensitive to electric fields, thus more suitable for SAR measurement. Loop antennas are sensitive to magnetic field and mostly used in in device tracking application for iMRI in various sizes and configurations. There are multiple antenna designs used with acousto-optic sensor. The details of the antennas will be given in the Chapter 4 and Chapter 5. In general, short dipole antennas were fabricated on a FR4 type printed circuit board (PCB). Single loop antennas were also fabricated on a PCB whereas multi turn coils were hand wound with 30 AWG insulated copper wire.

Figure 3-7 shows the schematic of the packaging of the acousto-optic sensor for MRI testing where the FBG section of the optical fibre is contained in a rigid glass tubes

with electrical and optical connections are provided on opposite ends. The sensor is connected to different receiver coils for testing and comparison to conventional coax cable connected active markers.

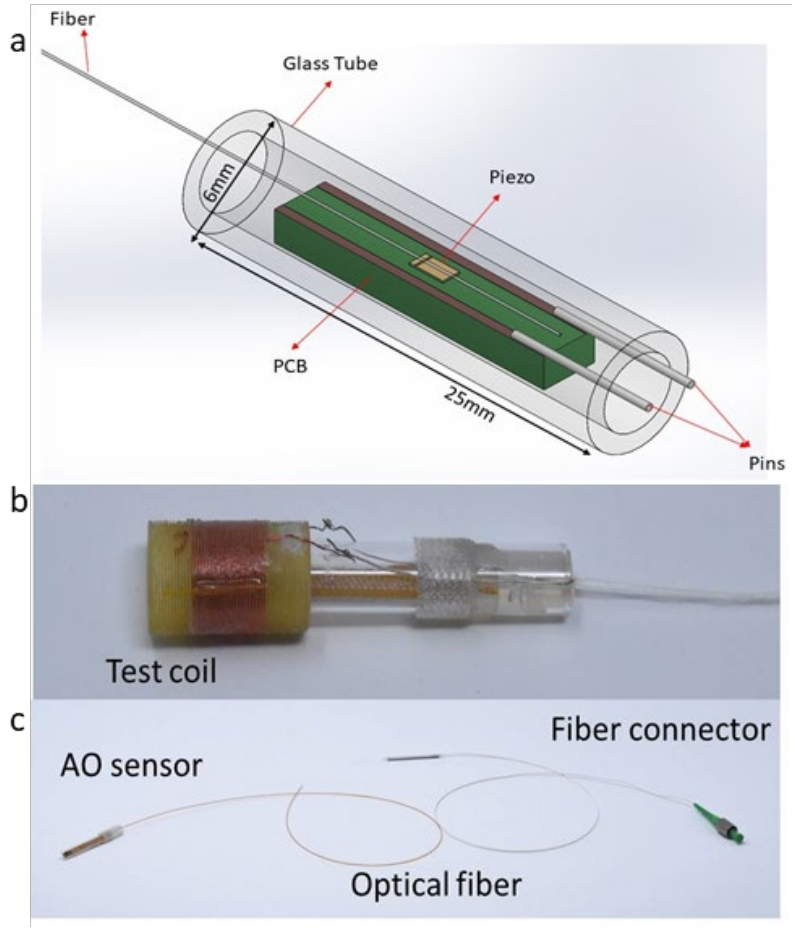

Figure 3-7 a) Schematic of the packaging of the AO sensor where the FBG section of the optical fiber is contained in a rigid glass tubes with electrical and optical connections are provided on opposite ends. b) The sensor connected to a test coil. c) Fully packaged sensor interfaced with an optical fiber.

3.2.2 Back-end Optoelectronics

Back-end optoelectronic system handles the read-out from the acousto-optic probe. Back-end optoelectronics schematic is given in Figure 3-8. A tuneable laser source (NKT Photonics, Denmark) provides a narrow linewidth, less than 1 kHz, laser light. One-way optical isolator is employed in order to prevent reflected light from FBG to go back into laser cavity. A three-way optical coupler separates laser light going into the probe end and reflected light from probe end. Reflected light with its intensity modulated around the Larmor frequency from the FBG is captured by a high trans-impedance gain InGaAs photo detector with 125MHz bandwidth (New Focus Model 1811, CA, USA).

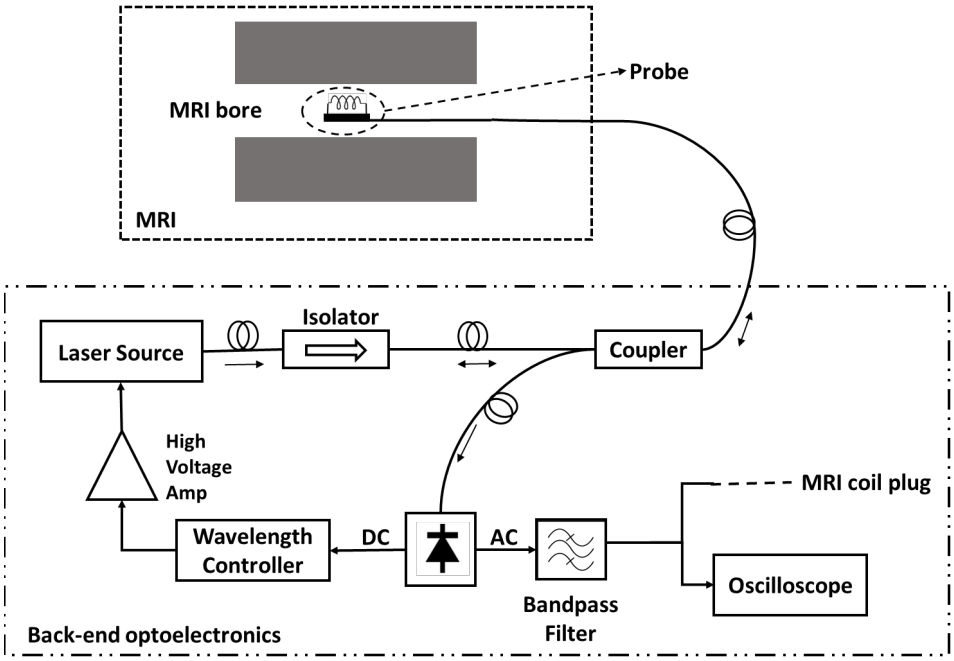

Figure 3-8 Schematic overview of the test setup.

Gradient magnetic field change creates acoustic noise up to 1.5 kHz due to Lorentz forces created on the gradient coils [124]. Since FBG sensor is sensitive to any elastic wave

induced on the fiber, the acoustic noise also modulates the reflected light from the FBG. AC output from the photodetector is filtered with a band-pass filter to reject the AC signal caused by the acoustic noise. Filtered AC signal is analysed with an oscilloscope. AC signal is also fed back into coil plug of MRI system, which is used for visualization of the interventional device.

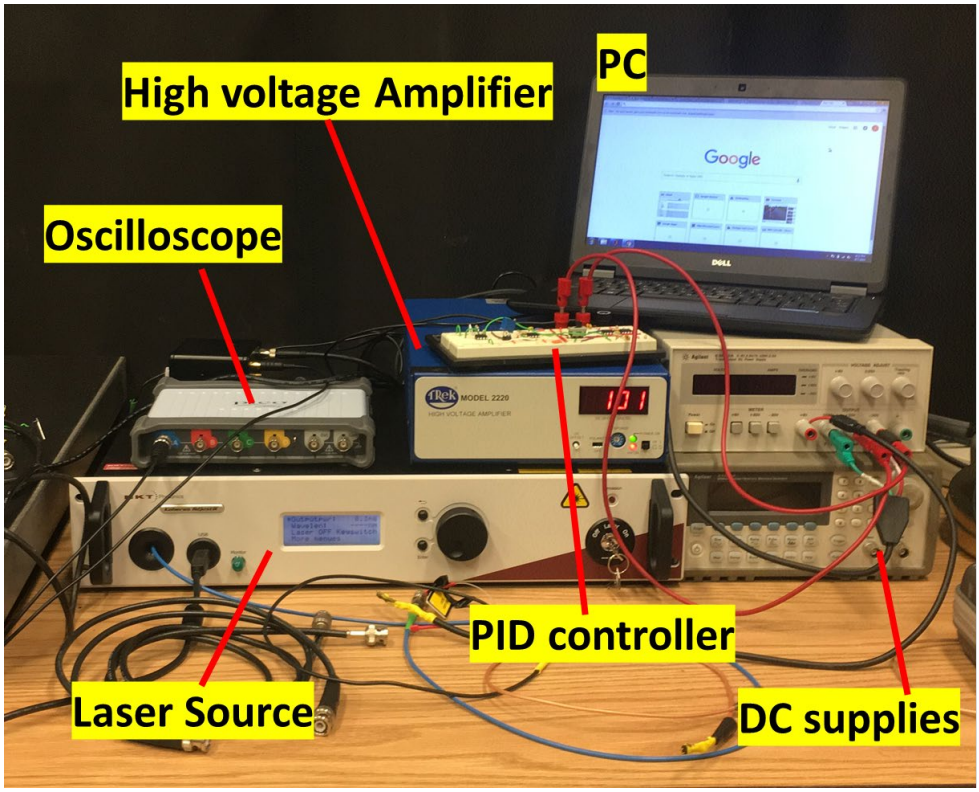

Figure 3-9 Photo of the back-end optoelectronics

Middle section of the side slope in the notch of FBG spectrum offers a linear operating region. Therefore, it is crucial to ensure laser wavelength is kept in the linear operating region of the FBG spectrum. Wavelength of the FBG can shift due to operating conditions such as temperature and mechanical load on FBG as well as high amplitude acoustic noise. Thus, a wavelength controller was designed based on an op-amp

proportional-integral derivative (PID) controller. Details of the wavelength controller is given in Appendix A.

Wavelength controller can track wavelength changes up to 20 kHz, which covers most of the acoustic noise due to gradient fields. Note that, wavelength change created by mechanical loading and temperature changes on the FBG sensor has much lower frequency and are readily adjusted for by the controller. In the experiments, the bias point on the side slope was set to 50% of the maximum reflection.

3.3 Characterization

The prototype was characterized through sensitivity and linearity tests in lab environment. We also validated the model by comparing the reflection spectrums of the fabricated gratings with simulations as well as pressure sensitivity.

3.3.1 Spectral Response of the FBG

The reflection spectrum of the FBGs were measured with the wavelength sweep function of the laser source around the Bragg wavelength. Bragg wavelength of each πFBG was tracked by adjusting the temperature of the laser. Then, spectrum of the πFBGs were measured by sweeping the laser source using the piezo-electric wavelength tuning mode of the laser around the Bragg wavelength. Note that, measured reflection spectrums are normally not centred around 1550nm due to fabrication tolerances. Thus, the measured reflection spectrums were shifted to 1550nm in order to compare the spectrum shape with the simulations. The spectrum shape is more critical than the absolute Bragg wavelength since readout is carried on the side slope of the center notch.

Figure 3-10 shows the reflection spectrum of π-FBG-1around the center notch. The reflection spectrum of the π-FBG-1 is in good agreement with the simulation results around the Bragg wavelength. Towards the edges, the measured spectral response is slightly deviating from the simulation results. Since the read out is performed at 50% bias and the optical modulation is usually small, the deviation at the edges will not have significant effect.

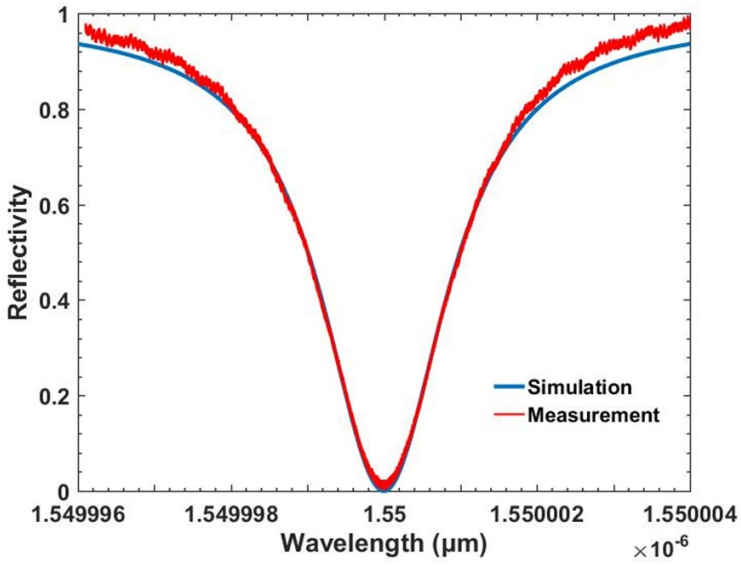

Figure 3-10 Reflection spectrum of π-FBG-1 around the center notch

Figure 3-11 shows the reflection spectrum of π-FBG-2 around the center notch. Similarly, the reflection spectrum of the π-FBG-2 close to simulation results except the notch shape is a little distorted. It should be noted that fabrication of πFBGs with a notch bandwidth of 0.4pm is very challenging, and ideal behavior is not expected.

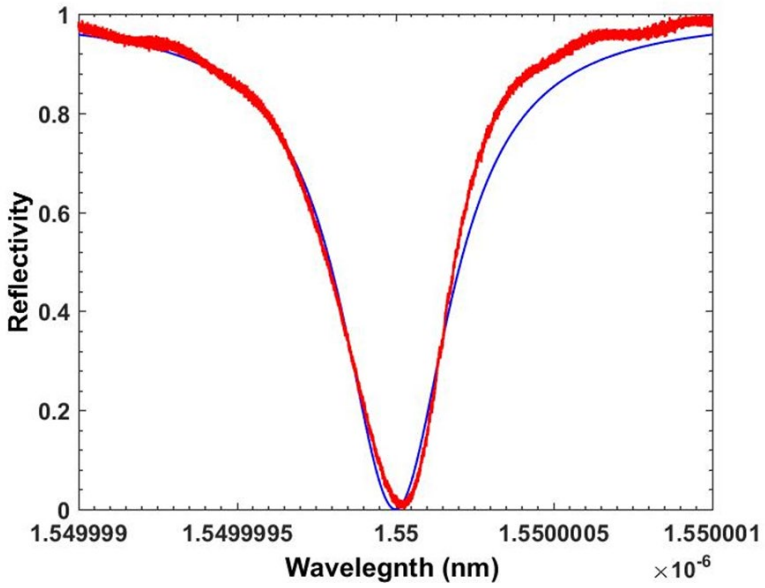

Figure 3-11 Reflection spectrum of π-FBG-2 around the center notch

3.3.2 Sensitivity of the FBG to Acoustic Waves

We characterized the sensitivity of the gratings to acoustic pressure (and resulting strain) by exciting them using a piezoelectric transducer immersed in water. Water immersion ensures uniform pressure distribution over the FBG region of the fiber. Figure 3-12 shows the components of the experimental set-up used for the sensitivity testing of the acousto-optic sensor.

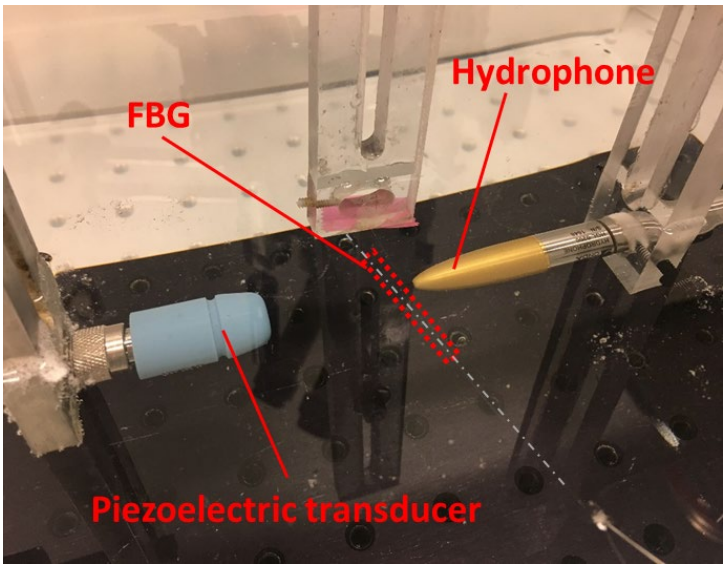

Figure 3-12 Experimental set-up for pressure sensitivity. The hydrophone is placed at the FBG location for pressure calibration

The πFBG is immersed in water at the focal region of a piezoelectric transducer (Panametrics Model A306S) with a center frequency of 2.25 MHz. In water, acoustic wavelength at 2.25MHz is 666 μm, which is more than twice the diameter of the fiber (125 μm), thus a uniform ultrasound generated strain over the radial thickness of the grating is achieved. This is further validated via FEA simulation; a fiber model was placed into water and excited with a point pressure source away from the fiber and the radial pressure distribution was investigated. The simulation results showed a continuous and uniform pressure field with 85% of the surrounding pressure field amplitude within the optical fiber, shown in Figure 3-13.

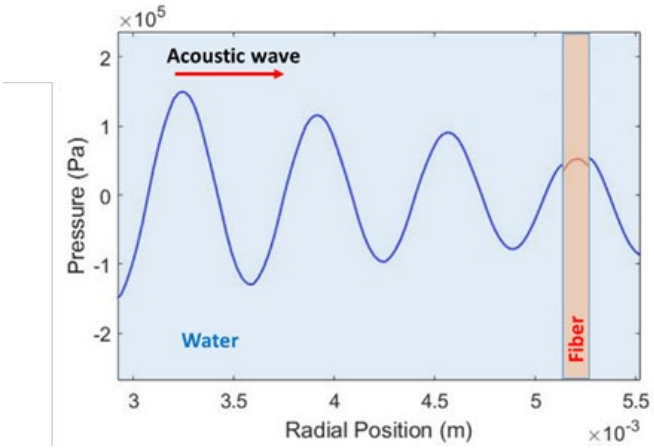

Figure 3-13) FEA simulation showing pressure distribution inside the FBG and the surrounding water in the axial direction. Note that the pressure field inside the fiber is 85% of the surrounding pressure field.

The acoustic pressure produced by the transducer at the same location was measured using a calibrated hydrophone (ONDA Model HGL0200). An input signal of 10 cycle tone burst with 10Vpp amplitude was used for acoustic wave generation which resulted in 107kPa peak pressure around the fiber, corresponding to 91kPa peak pressure at the fiber core.

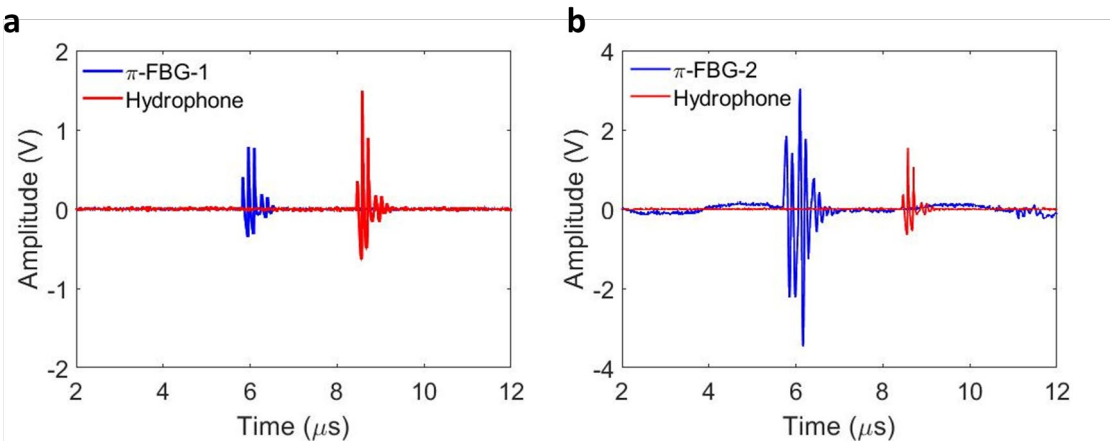

Figure 3-14 Pressure field captured by π-FBG-1 (a) and π-FBG-2 (b) with the hydrophone measurement. The time delay between the FBG and hydrophone signals is due to the ~4mm distance between them.

Laser intensity was adjusted such that the photodetector output is 10V when maximum reflection is achieved from the gratings. For the same pressure field measured by the hydrophone, π-FBG-1 generated 1.1V output whereas π-FBG-2 generated 7.3V output (Figure 3-14). Therefore, the pressure sensitivity of the sensors can be calculated as **80 mV/kPa** for π-FBG-2 and **12 mV/kPa** for π-FBG-1. A comparison between the simulated and measured pressure sensitivities is provided in Table 3-1. Note that the measured sensitivities are approximately half of the simulated values. This discrepancy mostly due to fabrication tolerances; variations among piezoelectric transducers and lossy mechanical coupling between the FBG and the piezoelectric transducer. These variations will be substantially reduced with thin film configurations.

Table 3-1 Simulated and measured pressure sensitivity of the FBG sensors

	Simulation	Measurement
π-FBG-1	16 mV/kPa	12 mV/kPa
π-FBG-2	79 mV/kPa	80 mV/kPa

3.3.3 Linearity Analysis

Although both normal and phase shifted FBGs have been used as acousto-optic sensors with the side slope detection method, large portion of the slope of the spectrum has been assumed linear in the previous studies [106], [112]–[114]. This assumption is valid when the sensitivity of the FBG is relatively low and acousto-optic modulation is very small. However, when the sensitivity and strain levels are high, effect of non-linearity becomes prevalent in the form of sensitivity variations to amplitude and phase. Several groups [125], [126] have studied the linearity of Fabry-Perot based optical fiber sensors, which incorporate the side slope detection method. On the other hand, linearity analysis for FBG sensors are limited in the literature.

Since image formation in MRI is achieved by frequency and phase encoding, the linearity of the FBGs is very crucial in such applications, especially phase. In terms of phase sensitivity, mili-radian range phase stability is needed for acceptable image quality [127]. Each phase-encoding step usually takes an entire MR excitation step and takes up

significantly longer times than frequency encoding leading to build up of any non-linearity in phase. Moreover, high levels of acoustic noise and temperature changes under MRI further accentuates the problem as FBGs are inherently sensitive to all strain and temperature changes. In order to characterize FBG response in such dynamically challenging environments and highly sensitive applications requiring a detailed analysis of linearity and sensitivity of FBG sensors with FBG side slope read-out are required.

We investigated the linearity of the FBG by inspecting amplitude and phase sensitivity with respect to reflectivity level on the side slope. These experiments were carried out at 23.6 MHz, the Larmor frequency of the prototype 0.55T MRI system in which the subsequent imaging experiments were conducted. To record the sensitivity variation, the bias point on the side slope was slowly changed from minimum reflection to maximum reflection while using a continuous wave acoustic excitation. This configuration was also simulated using the acousto-optic modulator model. The resulting pressure distribution in the core of the fiber was used for time domain simulations in the optical model described above.

Amplitude sensitivity of the FBG sensors were calculated by taking the first derivative of the output signal with respect to bias as measured in Figure 3-10 and Figure 3-11. Moreover, the model was used for time domain simulations. A time domain pressure signal at 23.6 MHz with an amplitude of 1kPa was used as the input to the model and the corresponding optical modulation is calculated at different bias points. Simulation results were normalized to the experimental results for better comparison and amplitudes were presented in arbitrary units (AU) as the absolute amplitude values were not of interest for

this study. Moreover, pressure output from the piezoelectric transducer was kept such that the optical modulation does not exceed 1% in order to ensure linearity across the spectrum.

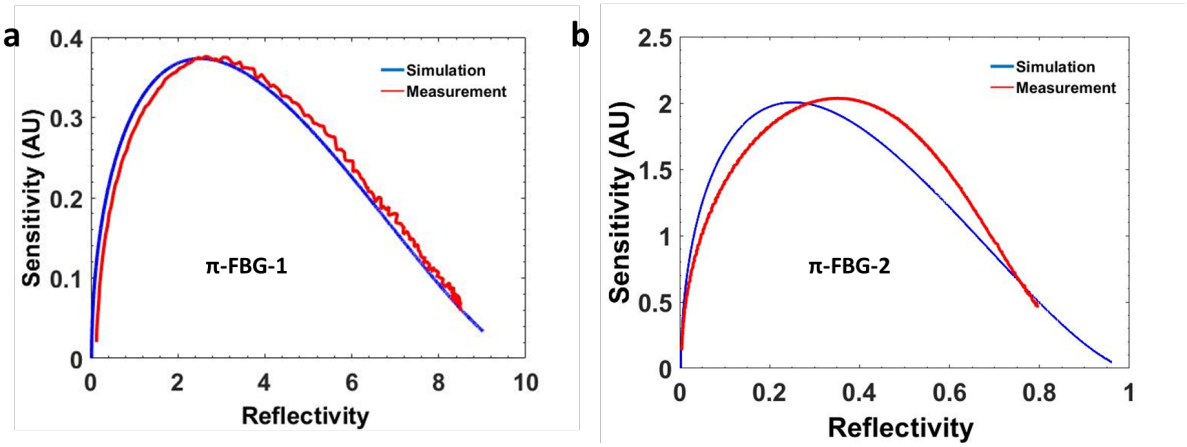

Figure 3-15 Pressure sensitivity of π-FBG-1 (a) and π-FBG-2(b) with respect to reflectivity on the side slope.

As seen in Figure 3-15, simulation results are in good agreement with the experimental results. Maximum sensitivity is observed around 25% bias on the side slope rather than 50% as reported earlier by [113]. In π-FBG-2, the experimental data shows that the maximum sensitivity is observed around 35% rather than 25% due to the fabrication tolerances. Maximum sensitivity of FBG-2 is 5.7 times greater than π-FBG-1, which is comparable to the hydrophone measurements reported in the previous section; sensitivity of π-FBG-2 was 6.6 times larger than π-FBG-1. Moreover, amplitude linearity is observed only at a limited range around the 25% bias rather than 20-80% as assumed by [106]. Sensitivity is within 1% of its maximum value from 21% to 29% bias. Thus, unwanted bias change on the side slope should be kept under 8% for a maximum amplitude variation of 1%. Note that the response of the FBG sensors becomes unreliable under 5% and above

80% bias as the reflectivity curve becomes noisy and signal levels are significantly reduced.

Phase response of the FBG sensors were tested using the same set-up. A continuous wave excitation at 23.6 MHz was used as the input and the optical signal and the input signal was recorded at different bias points. Then the phase difference between the input signal and the optical signal was calculated. Similarly, simulations were performed at 23.6 MHz with an 1kPa pressure input then the phase difference between the pressure input and the modulated optical signal was calculated for different bias points.

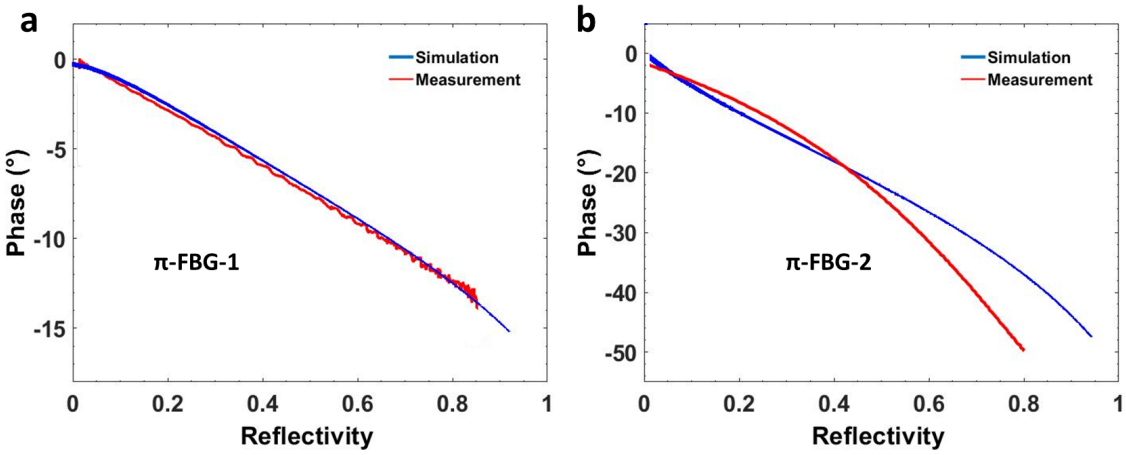

Figure 3-16 Phase change with respect to reflectivity on the side slope for π-FBG-1 (a) and π-FBG-2 (b).

A linear relation between the bias point and the phase was observed between 5% and 80% reflectivity (Figure 3-16). Simulation and experimental results are in good agreement except for π-FBG-2. There is a less then 4° deviation from the simulations up to 50% bias, then the difference becomes more pronounced. As discussed above, this discrepancy can be attributed to the non-ideal fabrication tolerances. The phase changes

0.165° per 1% bias change for π-FBG-1, whereas phase changes 0.48° per 1% bias change for π-FBG-2 up to 50% reflectivity. Highly phase sensitive MRI applications requires the unwanted phase due to bias change to be strictly monitored and corrected in order to minimize image distortion. Phase correction can be achieved using proper phase shifting electronics. A demonstration of phase correction artefact correction in real-time is presented in Chapter 5.

3.3.4 Frequency Response

The acousto-optic sensor introduced in this work has limited bandwidth due to the resonant nature of the piezoelectric transducer. Frequency response of the sensor around its first resonance is given in Figure 3-17.

The sensor has a bandwidth of 3 MHz at FWHM around 22.5 MHz. The limited operational bandwidth of the sensor will limit its use in some applications where the frequency of the RF field either has a wide range or is unknown. However, this sensor is suitable for MRI applications where the operating frequency is known and has a narrow range. For a 100kHz frequency bandwidth, the sensor has a relative standard deviation of 1.9% at 63.86 MHz. Note that, frequency bandwidth of RF signals in MRI usually does not exceed few kHz.

Moreover, the center frequency, bandwidth and the sensitivity of the sensor can be adjusted by using different piezoelectric crystals. High quality factor piezoelectric crystals will have higher sensitivity with limited bandwidth whereas low quality factor piezoelectric crystals will have lower sensitivity with broader bandwidth. The center frequency can be

adjusted by changing the thickness of the piezoelectric crystal. Thus, the magnetic field sensor can be optimized for the specific MRI system and application.

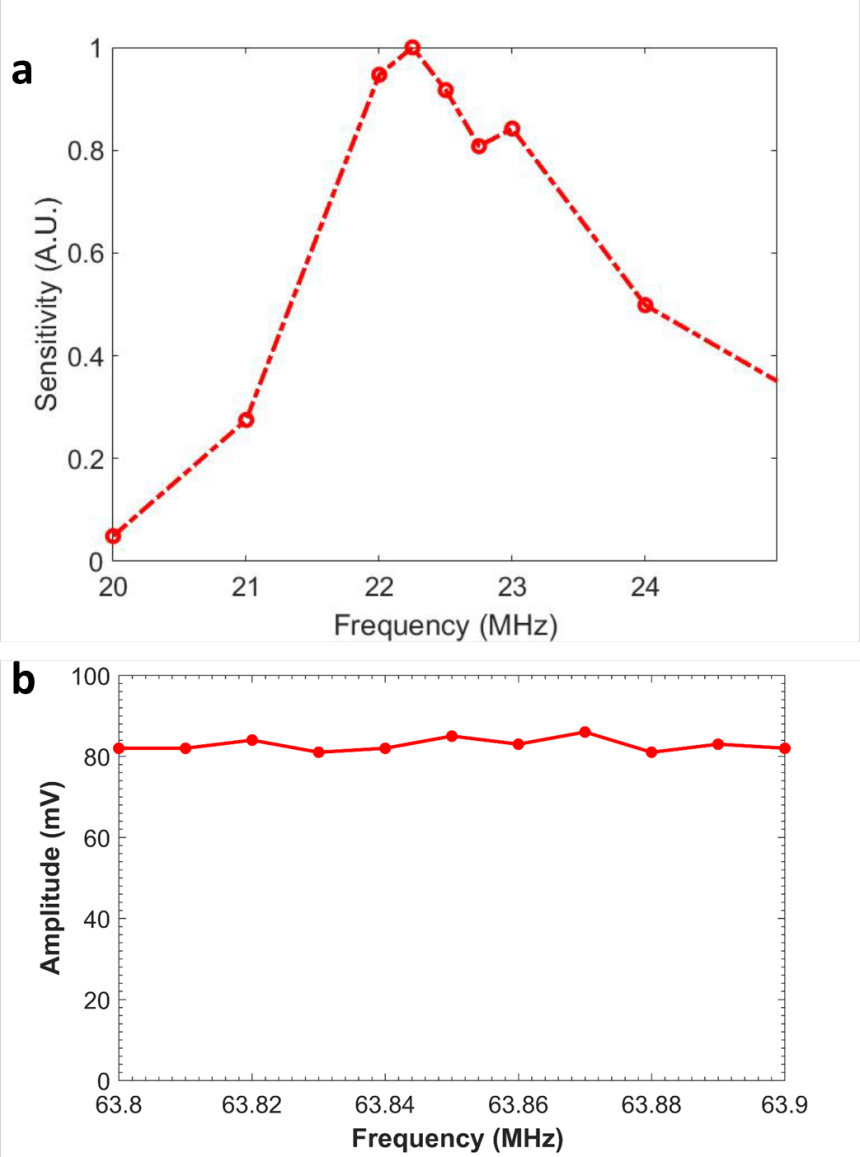

Figure 3-17 Frequency response of the acousto-optic sensor for a) 0.55 T MRI system and b) 1.5T MRI system

3.3.5 Noise Analysis

There are three noise sources present in the acousto-optic modulator: photodetector, laser and piezoelectric transducer.

Photodetector noise has three components: thermal, shot and amplifier noise [128]. Thermal noise is generated by the load resistor in the photodetector. Power spectral density of thermal noise, $N_{PD,thermal}$, is expressed as

$$I_{PD,thermal} = \sqrt{4kTB/R} \tag{20}$$

where k is the Boltzmann's constant, and T is the absolute temperature, B is bandwidth and R is input resistance of the amplifier. The spectral density of the thermal noise is independent of the frequency, also known as a white noise. Shot noise caused by statistical the nature of photodetection. The photocurrent fluctuates as the result of the discrete photon arrival. Power spectral density for shot noise is given

$$I_{PD,shot} = \sqrt{2qB(i_p + i_d)} \tag{21}$$

where q is the electron charge, i_p is induced photocurrent and i_d is dark current. Shot noise is also a white noise and the noise and depended on light intensity. In a photodetector, an electrical preamplifier has to be used immediately after the photodiode to amplify the photocurrent signal and convert it into an electrical voltage. Preamplifier noise is expressed

as in input rms noise, $I_{PD,amp}$, and given for the particular preamplifier. The total photodetector noise, $I_{n,PD}$, can be expressed as the summation of the noises;

$$I^2{}_{n,PD} = I^2{}_{PD,thermal} + I^2{}_{PD,shot} + I^2{}_{PD,amp} \tag{22}$$

Manufacturers usually provides noise equivalent power (NEP) which is the minimum optical power required for an SNR of 1. Using NEP, the voltage and current equivalent noise can be calculated as

$$I_{n,PD} = NEP \cdot \Gamma \cdot \sqrt{B} \tag{23}$$

$$V_{n,PD} = I_{n,PD} \cdot Z_{TIA} \tag{24}$$

where Γ is photodetector responsivity and Z_{TIA} is preamplifier transimpedance gain.

The particular photodetector has a fairly flat noise spectrum at frequencies higher than 10 MHz. NEP is given as $22.5\ pW/\sqrt{Hz}$, Γ is given as 1A/W and the transimpedance amplifier has a gain, Z_{TIA}, of 40 V/mA. Thus, voltage noise amplitude of the photodetector is calculated as $2.52\ \mu V/\sqrt{Hz}$.

Similar to a photodetector, a single mode laser source will have shot noise and electronics related noise. Electronics related noise is usually caused by fluctuations in the pump current. Pump current fluctuations usually die in kHz ranges [129]. Shot noise is related to the discrete emission of the photons from the laser. A good laser will be designed

shot noise limited. Laser noise is usually characterized with relative intensity noise (RIN) which is expressed as

$$RIN = 2 \cdot \frac{hc}{\lambda P}\sqrt{B} \tag{25}$$

where *h* is Planck's constant, c is speed of light, λ is wavelength and P is optical laser power [130]. RIN is a relative power noise normalized to the average power level. Thus, equivalent noise at the photodetector output cause by the laser can be calculated as

$$V_{n,laser} = RIN \cdot \Gamma \cdot Z_{TIA} \tag{26}$$

Laser has a wavelength of 1550nm. During the experiments, laser intensity was adjusted to 3.9mW output power such that the photodetector output is 10V when maximum reflection is achieved from the gratings. Therefore, RIN is calculated as 0.066 $pW/\sqrt{Hz}$ and $V_{n,laser}$ is calculated 2.63 pV/$\sqrt{Hz}$.

Noise of piezoelectric transducer is purely related to thermal noise and expressed as

$$V_{Piezo,thermal} = \sqrt{4kTBR} \tag{27}$$

Thus, equivalent piezo noise at the photodetector output can be determined using previously calculated acousto-optic conversion gains and input resistance of the piezoelectric transducers. The particular piezoelectric transducers used in the sensor have an input resistance range from 100 Ω to 4 kΩ. Using the worst case scenario, R = 4 kΩ and

acousto-optic conversion gain of 8.75V/V, the equivalent piezo noise at the photodetector output is calculated as $71.2\ \mathrm{nV}/\sqrt{Hz}$.

The overall noise of the acousto-optic modulator can be calculated by summind the power spectral densities of photodetector, laser and piezo noise;

$$V^2{}_{noise,total} = V^2{}_{n,PD} + V^2{}_{n,laser} + V^2{}_{n,piezo} \tag{28}$$

Note that, the photodetector noise has the largest noise by far and dominates the overall noise. Thus, the acousto-optic modulator noise can be approximated as $2.52\ \mu\mathrm{V}/\sqrt{Hz}$. Actual spectral noise density of the acousto-optic modulator was also calculated by determining the spectral density of the output signal without any electrical input to the piezoelectric transducer. The voltage equivalent peak to peak noise of the acousto-optic modulator is measured as $\underline{\mathbf{5.6\ \mu V/\sqrt{Hz}}}$ that is slightly more than the calculated noise. The difference between the calculation and the measurement is acceptable as given NEP of the photodetector is an estimated average value.

The output of the acousto-optic sensor starts to saturate at 8V. Thus, the dynamic range of the acousto-optic modulator can be calculated as $117\mathrm{dB}/\sqrt{Hz}$.

3.4 Summary

This chapter explained the details of the acousto-optic modulator. Working principle of the acousto-optic modulator is explained. Detailed sensor characterization and analysis are performed and model is further validated through various experiments (aim D). Lastly, noise analysis of the acousto-optic modulator is performed.

The major points of this chapter are listed as follows:

- A prototype acousto-optic modulator is fabricated with the previously designed FBGs, π-FBG-1 and π-FBG-2, and a $LiNbO_3$ bulk piezoelectric transducers. The alignment of piezoelectric transducer on the FBG sensor should be carefully performed as the phase shifted FBGs are most sensitive at the center.
- A wavelength controller based on a PID controller needed to developed to track the Bragg wavelength which changes over time due to external stress or temperature change.
- Spectral response of the designed FBGs closely matching with simulation results. π-FBG-2 with 0.4pm bandwidth has a slight mismatch as it is challenging to manufacture FBGs with sub-pm bandwidth.
- Pressure sensitivities were calculated as 80mV/kPa for π-FBG-2 and 12mV/kPa for π-FBG-1, which are approximately half of the simulation results. These variations expected to be reduced with thin film configurations. Moreover, highest sensitivity was observed at 25% the bias point, unlike widely accepted 50%.

- A linear relation between the phase and bias point was observed: the phase changes of 0.165° per 1% bias change for π-FBG-1 and phase changes 0.24° per 1% bias change for π-FBG-2. This unwanted phase due to bias change needs to be corrected for device tracking application.
- The noise of the acousto-optic modulator is dominated by the photo-detector noise and measured as $\mathbf{5}.6\ \mu V/\sqrt{Hz}$ which results in a dynamic range of 117dB/$\sqrt{Hz}$. Thus, aim C1 is achieved.

CHAPTER 4. RF FIELD SENSING

4.1 Overview

The acousto-optic modulator part of the sensor was characterized in the previous chapter. This chapter focuses on the characterization of the sensor with different antennas for RF field sensing. The sensor was tested in a transverse electromagnetic (TEM) cell which generates uniform electric and magnetic fields. The sensor was tested for magnetic field sensing with loop antennas and for electric field testing with short dipole antennas as well as using the piezoelectric transducer as a parallel plate antenna. Lastly, temperature sensing capability of the sensor was demonstrated.

4.2 Experimental Set-up

Uniform electric field (E field) and magnetic field (B Field) needs to be generated for the testing of acousto-optic sensor for RF field measurements [131]. RF emission and sensing tests are typically carried out in well calibrated anechoic chambers, using antennas to generate RF fields or pick up the radiated signals. Due to bandwidth limitations, several antennas are required to generate uniform fields. Furthermore, it requires much space and the cost of the equipment for a standard conformant setup is immense. As an alternative, transverse electromagnetic (TEM) cells have been used for testing of electronic devices for electromagnetic compatibility (EMC).

4.2.1 TEM Cell

A TEM cell can be used for accurate and homogeneous electro-magnetic field generation from DC to few hundred MHz [132], [133]. TEM cells are consists of a septum and ground walls, shown in Figure 4-1. TEM cells are in essence, large waveguides with transmission lines being parallel plates. TEM cells are usually matched and terminated with an 50 Ohm load resistance.

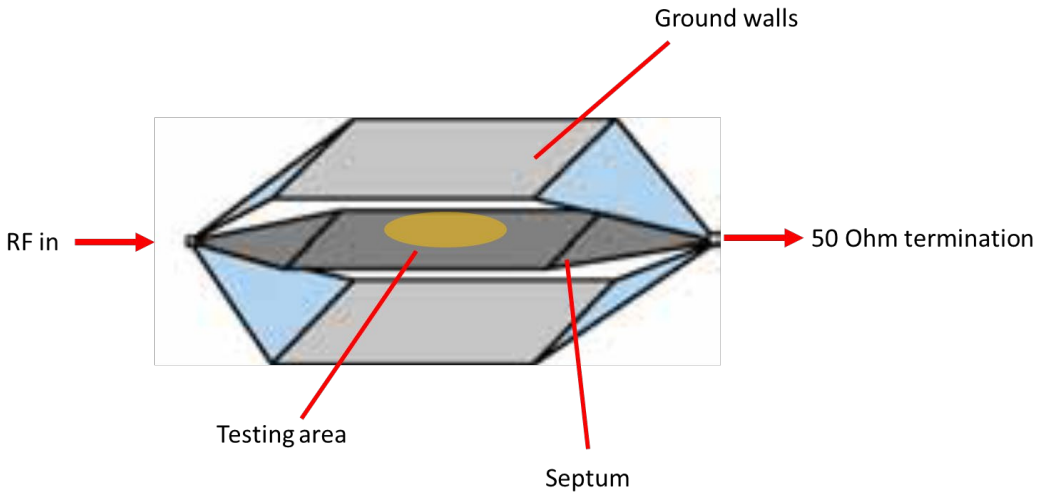

Figure 4-1 Schematic of an TEM cell showing its components.

A TEM cell can generate an average E field at the testing area which is the center of septum and between septum and ground walls is given as:

$$E = \frac{V}{d} C_e = \frac{\sqrt{pZ_o}}{d} C_e \tag{29}$$

where V is the rms input voltage, d is the distance between the septum and the ground walls, p is the RF power and Z_o is the characteristic impedance of TEM cell, usually 50 Ω,

and C_e is a correction factor for the specific TEM cell geometry. In order to achieve the desired characteristic impedance, the dimensions of the TEM cell should be calculated accordingly [134].

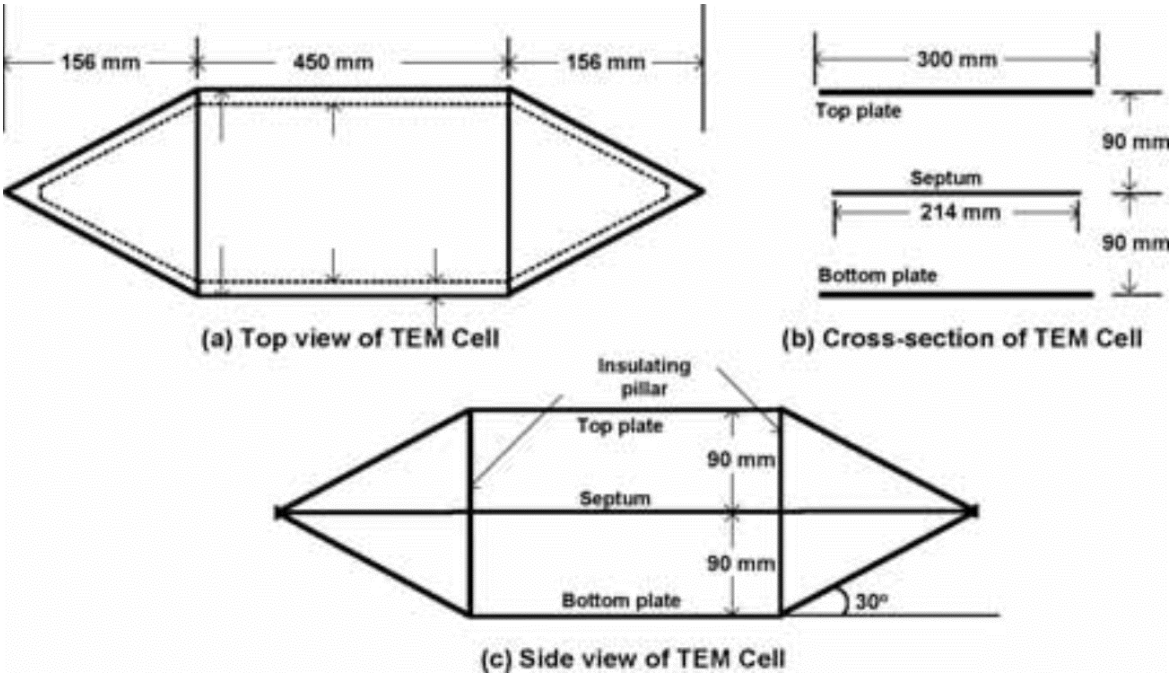

Figure 4-2 Open TEM cell prototype dimensions.

We constructed a TEM cell with thin aluminium sheets using the dimensions and geometry given in Figure 4-2. The constructed TEM cell can be seen in Figure 4-3.

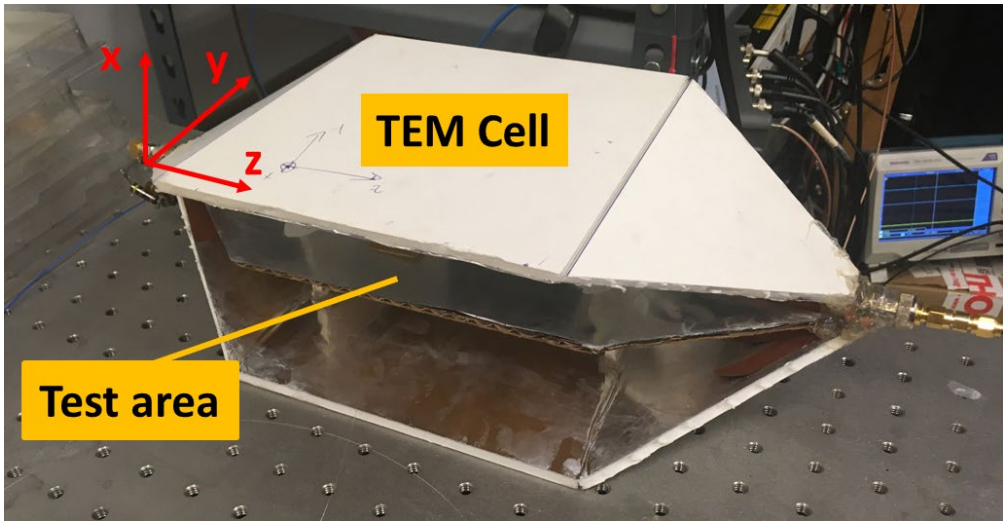

Figure 4-3 Constructed TEM cell with characteristic impedance of 50 Ω

The TEM cell has a characteristic impedance of 50 Ω from DC to 40 MHz. The signal generator can generate $5V_{rms}$ at 23.65 MHz. The TEM cell has a septum height of 5cm and C_e of 1.2. Thus, an E field of 120V/m can be generated in the test area. Similarly, the B field in the testing area is calculated at 190nT. The generated fields were further characterized with commercially available an E field probe (Beehive 100D) and an B field probe (Beehive 100B) with measured E field of 120V/m and B field of 188nT.

4.3 Magnetic Field Sensing

RF field has an electric and magnetic field component. According to Maxwell equations, when RF field is in the far field and propagating through a homogeneous media with a zero current density (J), the relationship between the magnetic fields and electric fields is given as;

$$B = \frac{1}{c_0}\,\hat{k} \times E \tag{30}$$

where c_0 is speed of light and $\hat{k}$ is the unit vector in the propagation direction. However, this relation does not hold in the near field, especially when the medium is inhomogeneous. RF fields in MRI are usually in near field and the human body has complex electromagnetic properties, thus the electric and magnetic components of the electromagnetic field need to be measured separately [135].

4.3.1 Fiber Optic Sensors for Magnetic Field Measurement

Most of the fiber optic magnetic field sensors falls into four categories; Faraday effect, ampere force, magneto-strictive materials or magnetic fluids. In Faraday type fiber optic magnetic sensors, circular birefringence induced in the fiber by the external magnetic field is exploited [136]. Even though Faraday type sensors offer compact and robust sensing mechanisms, they suffer from low sensitivity. Ampere force type fiber optic sensors are coated with conductive materials in order to drive current over the fiber and the strain induced by the Ampere law is detected [137]. Ampere force type sensors can be only used for DC to low frequency applications and they disturb the electromagnetic field. Magneto-strictive type sensors utilizes external magneto-strictive elements which induces strain under magnetic field [138]. These sensors suffer from undesired hysteresis and low magnetic sensitivity as well as low frequency operation. Lastly, in the recent years, magnetic fluids, that refractive index of the fluid is sensitive to magnetic field, have been used for magnetic field sensing [139]. Like magneto-strictive materials, magnetic fluids also suffer from hysteresis.

Alternatively, small loop antennas can be used as magnetic sensors. However, loop antennas require conductive electric connections which acts like an antenna resulting in magnetic field distortion, current surge and loss of signal coming from the loop antenna. In order to overcome these problems, we used the acousto-optic modulator to convert the electrical signal from the loop antenna into optical signal to be carried by optical fibers.

4.3.2 Acousto-optic Probe for Magnetic Field Measurements

The magnetic field sensor is based on a small loop antenna coupled to the acousto-optic modulator, shown in Figure 4-4.

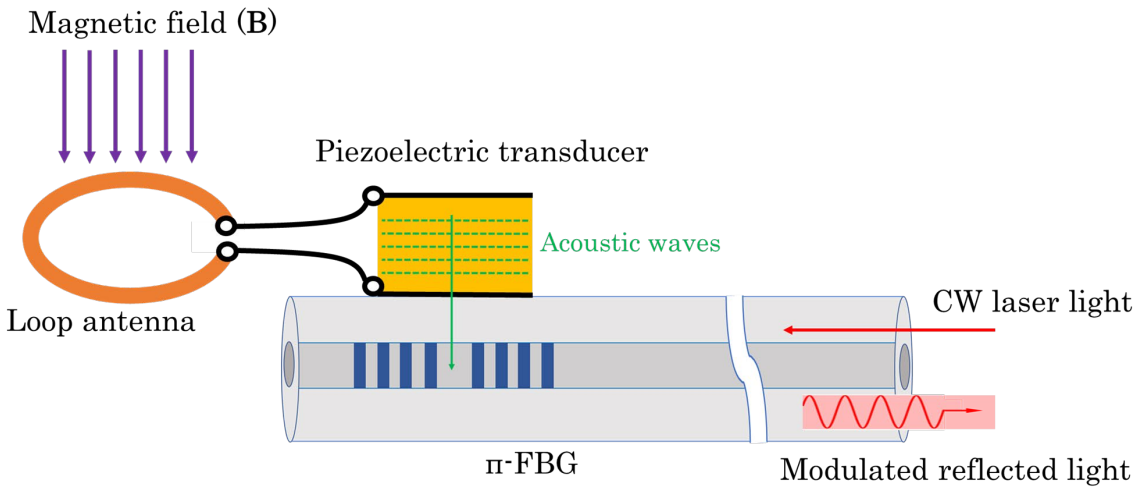

Figure 4-4 Schematic of the acousto-optic modulator with the loop antenna for magnetic field measurements.

A loop antenna is considered small when its diameter is much smaller than the wavelength in the medium (i.e diameter $< \lambda/10$). When a loop antenna is electrically small,

the current within the loop can be approximated as being constant along the loop. Thus, the impedance of a small loop is inductive resulting in the small loop antennas being only sensitive to magnetic field component of the electromagnetic wave. The time varying magnetic field, B, going through a conductive loop induce a voltage due to Faraday's law of induction (31). Voltage (V) induced on the coil is a function of time varying magnetic field (B), angle between the magnetic field and loop axis (θ) and loop geometry; area (A) and number of turns (N).

$$V = 2\pi NAfB\cos\theta \tag{31}$$

The sensor output is proportional to the magnetic field as; the induced voltage (V) is linearly dependent on the magnetic field and the strain generated in the fiber by the piezoelectric transducer is proportional to V. The sensitivity of the sensor can be optimized by changing the loop geometry. Larger loops will yield higher sensitivity whereas smaller loops will have better spatial resolution. Sensitivity can be increased by increasing number of turns (N) while keeping the spatial resolution small.

The wavelength in the human body (λ) can be calculated using (32),

$$\lambda = \frac{c_0}{f\sqrt{\varepsilon_r \mu_r}} \tag{32}$$

where c_0 is speed of light in vacuum, f is frequency of RF field, ε_r is relative permittivity of average human body, μ_r relative permeability of average human body. c_0 is $2.99 \times 10^8\ m/s$, average ε_r is 80 and μ_r is 1 for an average human body. Thus, the

wavelength is approximately 140cm for 0.55T MRI, 52cm for 1.5T MRI, 26cm for 3T MRI and 11cm for 7T MRI systems. In order to assure the loops are electrical small, loop diameters were kept under 1cm. Three single loop antennas were milled out of PCB boards with three different loop diameters: 2mm, 4mm, 8mm. The overall sensor size is determined by the loop antenna as it is the largest component and can be stacked with the acousto-optic modulator when a small sensor footprint is desired. A photo of the tested sensor with 2mm diameter loop antenna is given in Figure 4-5.

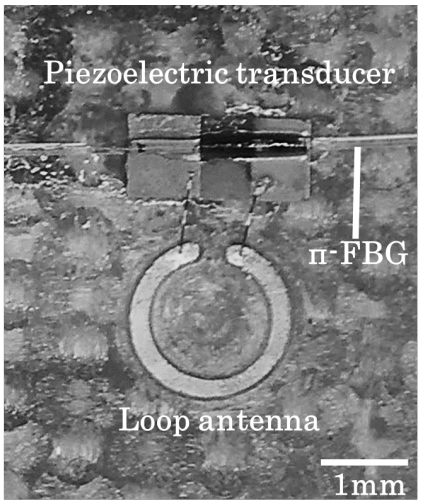

Figure 4-5 Close up view of the tested magnetic field sensor with 2mm dimeter loop antenna.

The magnetic field experiment set-up with TEM cell can be seen in Figure 4-6. The read-out scheme is the same side slope detection as explained in the Chapter 2. Maximum laser power was set so that the photodetector output is 10V and the side slope bias was set to 5V. The TEM cell was driven at 23.65 MHz which simulates a 0.55T MRI system.

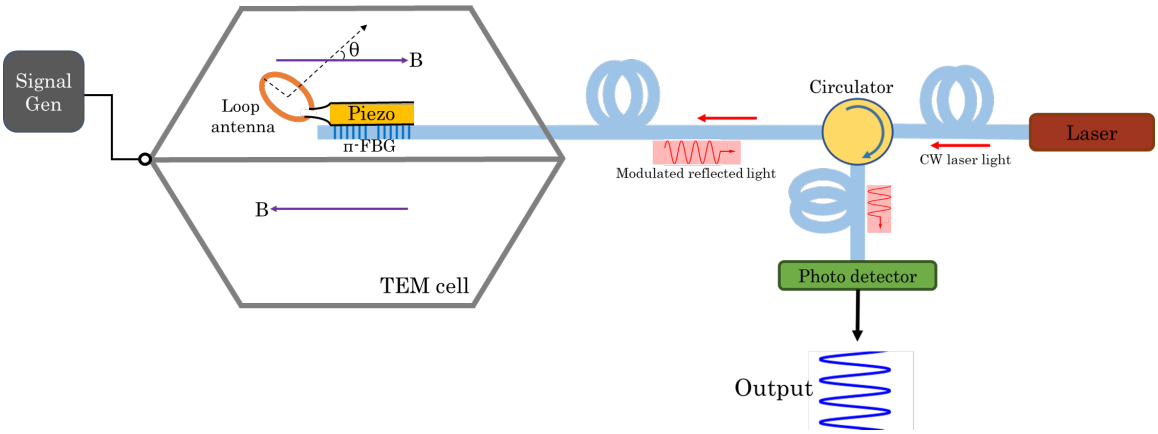

Figure 4-6 Experimental set-up for magnetic field testing with TEM cell.

4.3.3 Sensitivity

The magnetic field inside the TEM cell was changed from 0 nT to 188 nT by adjusting the input voltage to the TEM cell. Output voltages of the sensor with different size loop antennas; 2mm, 4mm and 8mm, are given in Figure 4-7. The output voltage responses are linear with respect to the magnetic field, as the theory.

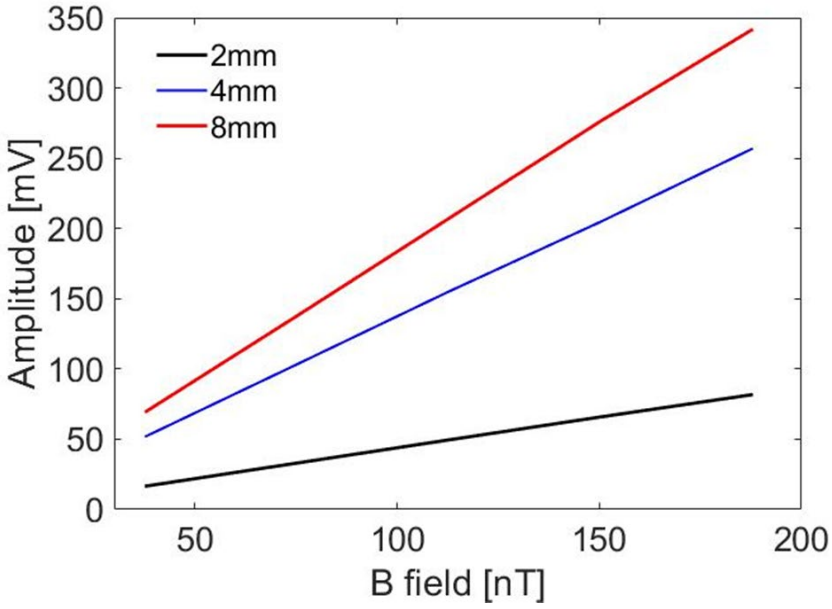

Figure 4-7 Sensitivity of different size loops for varying magnetic fields.

A summary of magnetic field sensitivity and dynamic range for different size loops are given in Table 4-1. Sensitivity of the sensors are measured as 1.84 mV/nT, 1.36 mV/nT and 0.44 mV/nT for loop antenna diameter of 8mm, 4mm and 2mm, respectively. According to eq. (31), the sensitivity should increase linearly with the area of the loop. However, the sensitivity is increased by a factor of 3.1 between 2mm to 4mm loop diameter and 1.35 between 2mm to 4mm loop diameter as opposed to a factor of 4. This could be caused by the phase change of magnetic field inside the TEM cell with respect to spatial position. As the loop size gets larger, the effect of destructive interreference of the magnetic field would be more pronounced. Once each sensor is characterized, this should not be a problem as the individual sensor response is highly linear over the tested magnetic field, as seen in Figure 4-7.

Table 4-1 Summary of magnetic field sensitivity and dynamic range for different size loops.

Loop diameter	Sensitivity	Minimum detectable magnetic field	Dynamic range (bandwidth100kHz)
2 mm	0.44 mV/nT	25.4 pT/√Hz	8nT- 18.2μT
4 mm	1.36 mV/nT	8.2 pT/√Hz	2.6nT-5.9μT
8 mm	1.84 mV/nT	6.1 pT/√Hz	1.9nT-4.35μT

The noise floor is measured at 5.6 μV/√Hz for this particular acousto-optic modulator. Thus, the minimum detectable magnetic fields for each sensor configuration are calculated as 6.1 pT/√Hz, 8.2 pT/√Hz and 25.4 pT/√Hz for loop diameters of 8mm, 4mm and 2mm respectively. As the sensor starts to saturate around 8V, the dynamic range of the sensor was calculated as 117dB for a bandwidth of 1Hz. For a typical MRI system, the maximum bandwidth of the B1 field will not exceed 100kHz. Thus, the measurable magnetic field range calculated as 1.9nT- 4.35μT, 2.6nT-5.9μT and 8nT-18.2μT for loop diameters of 8 mm, 4 mm and 2 mm respectively. Considering the B1 field strength is usually in μT range, a sensor with smaller size antenna would be more suitable such as the 2mm loop antenna for magnetic field measurements under MRI. The 2mm sensor has a comparable performance (dynamic range of 25.4pT-18.2μT) to a similar size commercial

probe (Speag H1TDS time domain H field probe with a dynamic range of 0.4pT-1.25μT that is widely used in MRI applications.

4.3.4 Directivity

The directivity of the magnetic sensor is important to determine individual vector components of the B field. Orthogonal loops can be used to measure the vector components of B field if the sensor is directional. Radiation patter of a small loop antenna is given in Figure 4-8.

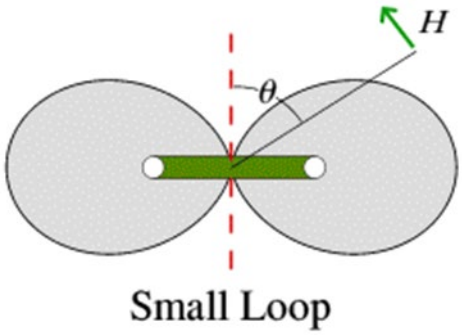

Figure 4-8 Radiation pattern of a small loop antenna.

The directivity of the sensor was measured by attaching the sensor on a rotational stage and SNR measurements were taken every 15°. The directivity of the sensor is determined by the cross-sectional area of the loop antenna perpendicular to the magnetic field, thus the sensor directivity is a function of $cos\theta$ as stated in eq. (31). Both measured and calculated directivity of the sensor are given in Figure 4-9. The measurement results match well with the calculations when the loop was facing the magnetic field vector,

around 0° rotation. However, as the rotation angle, θ, is increased, the measured directivity deviated from the theory slightly. This might be caused by a slight misalignment between the center of the rotational stage and the loop antenna axis. The difference between the measurement and theory is less than 0.1.

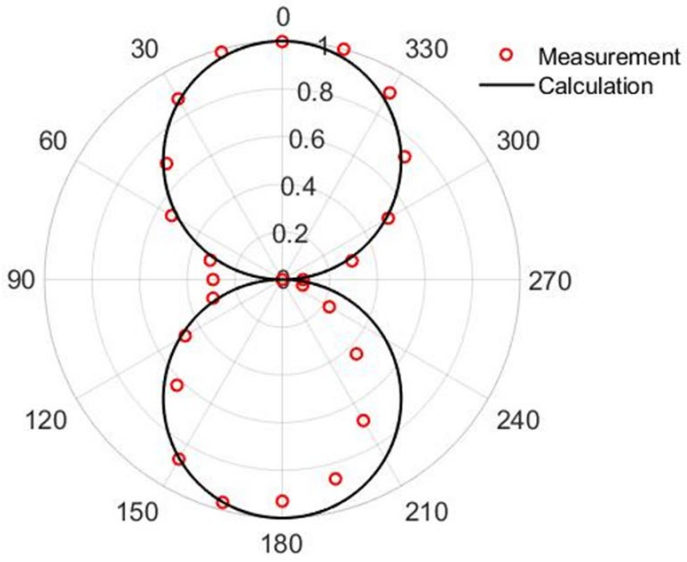

Figure 4-9 Directivity pattern of the magnetic field sensor.

The sensor is most sensitive when the B field is perpendicular to the loop antenna. Sensor output has two orders of magnitude difference for perpendicular and longitudinal B fields. Thus, the sensor is directional and suitable for measurement of the vector components of B field.

4.3.5 Repeatability

The acousto-optic sensor was tested for repeatability and hysteresis. The sensor was fixed in the testing area of TEM cell and multiple measurements were taken: 5 consecutive measurements followed by 5 measurements every 10 minutes. Relative standard deviations

(Relative StD) were calculated for output of 10 measurements, a summary is given in Table 4-2. Relative StD for 2mm and 4mm loops were measured below 1% for 10 measurements per sensor. 8mm loop has slightly higher relative StD at 1.72% which might be caused by the B field non-uniformity in TEM cell over 8mm. Moreover, hysteresis was not observed during the experiments. Thus, the fiber optic magnetic field sensor offers repeatable and reliable measurements.

Table 4-2 Relative standard deviations for magnetic field sensor for 10 measurements.

Loop diameter	2 mm	4 mm	8 mm
Relative StD	0.97 %	0.85 %	1.72 %

4.4 Electric Field Sensing

Tissues only absorb the E field component of the RF field. Thus, accurate measurement of E field is crucial in order to better understand the RF field – tissue interaction and assure patient safety. Traditionally, E field sensors are either based on short dipole antennas or electro-optic crystals. Fiber optic E field sensors can be both implemented with short dipole antennas or electro-optic crystals. An overview of different E field sensors is given in section 1.3.1.1.

4.4.1 Acousto-optic Probe for Electric Field Measurements

In a similar fashion, short dipole antennas are only sensitive to E field. The fiber optic electric field sensor is based on a short dipole antenna coupled to the acousto-optic modulator, shown in Figure 4-10.

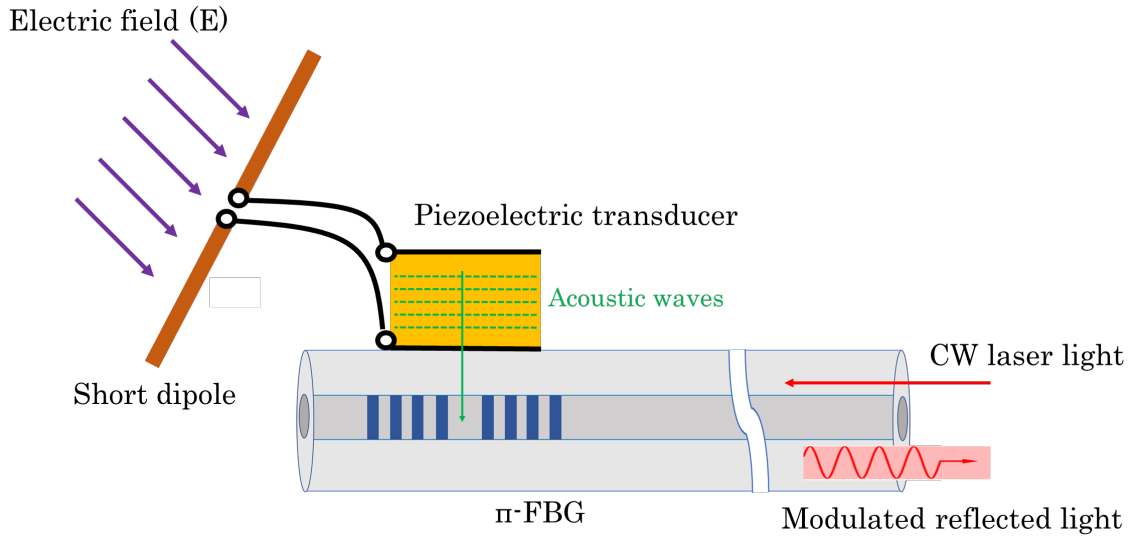

Figure 4-10 Schematic of the acousto-optic modulator with the short dipole antenna for electric field measurements.

A dipole antenna is considered short when its length is much smaller than the wavelength in the medium (i.e d < λ/10). The impedance of a short dipole antenna is capacitive; thus, the small loop antennas are only sensitive to electric field component of the electromagnetic wave. The time varying electric field, E, induces a voltage between the ports of a short dipole. Open circuit voltage (V_{oc}) induced on the dipole is a function of time varying electric field (B), angle between the electric field and dipole axis (θ), dipole half length (h) and frequency.

$$V_{oc} \approx hE \sin\theta \tag{33}$$

The sensor output is proportional to the electric field as; the induced voltage (V) is linearly dependent on the electric field, the strain generated in the fiber by the piezoelectric transducer is proportional to V and spectrum shift due to the acoustic wave is proportional to the strain. The sensitivity of the sensor can be optimized by changing the dipole length. Longer dipoles will yield higher sensitivity whereas shorter dipoles will have better spatial resolution. Three short dipole antennas were milled out of PCB boards with three different dipole lengths: 8mm, 16mm, 32mm. A photo of the tested sensor with 16mm dipole antenna is given in Figure 4-11.

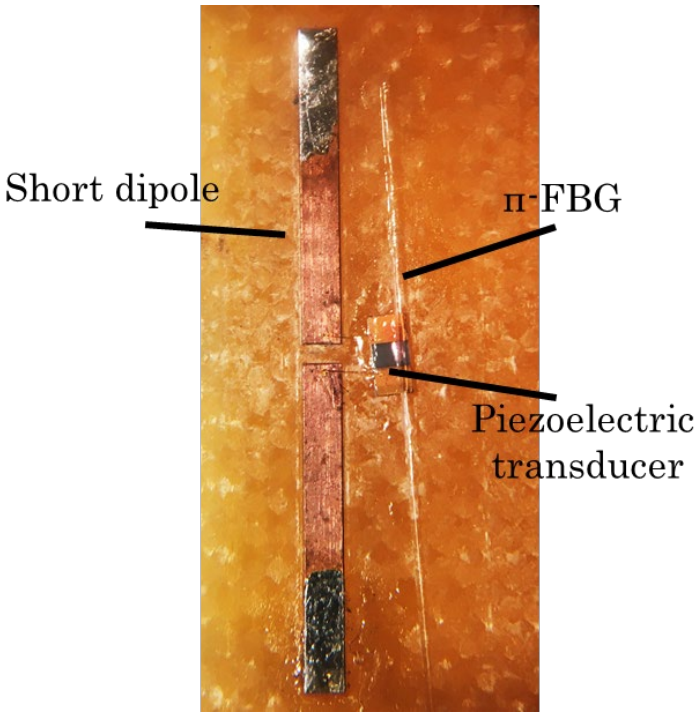

Figure 4-11 Close up view of the tested electric field sensor with 2mm dimeter loop antenna.

The electric field experiment set-up with TEM cell can be seen inFigure 4-12. The read-out scheme is the same as the magnetic field measurements.

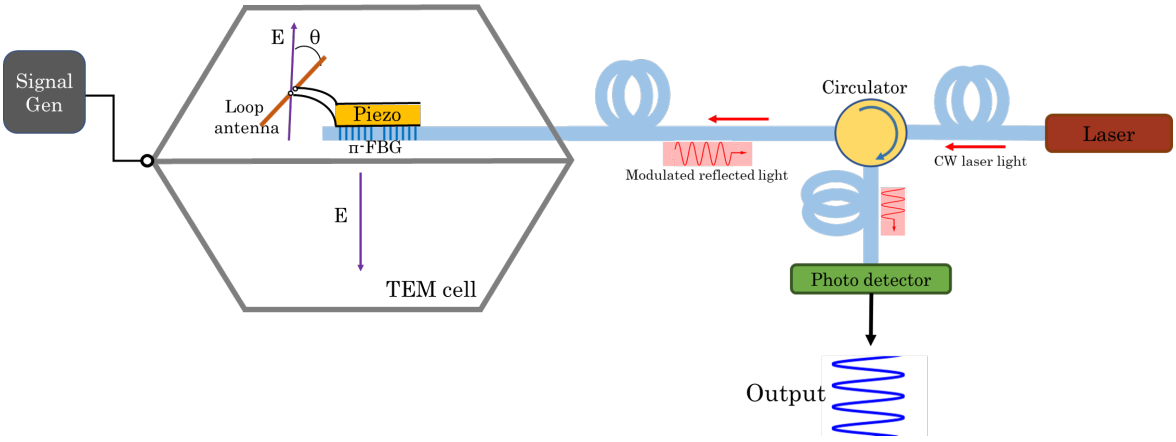

Figure 4-12 Experimental set-up for electric field testing with TEM cell.

4.4.2 Piezoelectric Transducer as an Electric Field Sensor

Piezoelectric transducer generates acoustic waves due to the electric field generated between the electrodes induced by an external voltage. So far, we have been using the antenna output as the input voltage to the piezoelectric transducer. However, the need for antenna can be eliminated; the external electric field on the piezoelectric transducer will induce a voltage drop between the electrodes, illustrated in Figure 4-13. In other words, the electrodes of piezoelectric transducer will act like a parallel plate antenna.

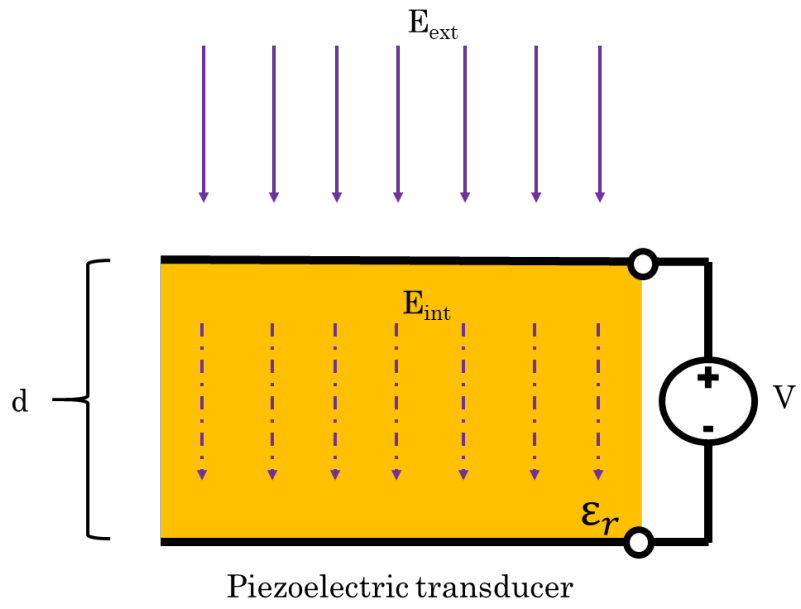

Figure 4-13 Piezoelectric transducer as a parallel plate antenna.

An external E field, E_{ext}, will result in an internal E field, $E_{int} = E_{ext}/\varepsilon_r$, inside the piezoelectric transducer. Therefore, the induced voltage across the electrodes will be

$$V = E_{int} \cdot d = \frac{E_{ext} \cdot d}{\varepsilon_r} , \tag{34}$$

where d is the thickness of the piezoelectric transducer. Note that, the dielectric constant of piezoelectric materials is quite high, air gapped parallel plates will have higher sensitivity then a piezoelectric transducer. Since a piezoelectric transducer with lower dielectric constant will have higher induced voltage, we used $LiNbO_3$ ($\varepsilon_r = 85$) for this application instead of PZT5A ($\varepsilon_r = 1900$). Same E field measurements as the short dipole antenna are performed with this sensor.

4.4.3 Sensitivity

The electric field inside the TEM cell was changed from 0 V/m to 120 V/m by adjusting the input voltage to the TEM cell. Output voltages of the sensor with different size loop antennas; 8mm, 16mm and 32mm, as well as without an antenna are given in Figure 4-14. The output voltage responses are linear with respect to the electric field.

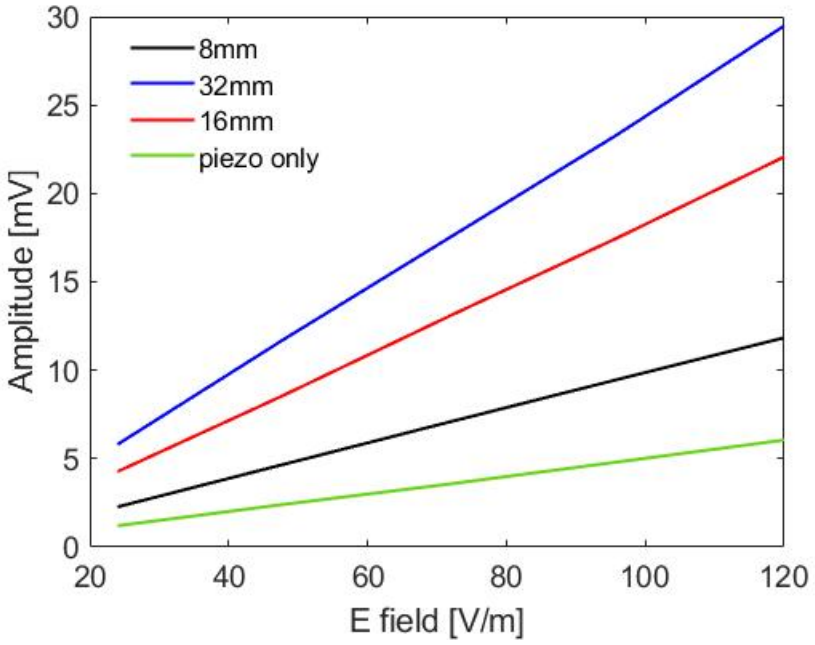

Figure 4-14 Sensitivity of different size dipoles for varying electric fields.

A summary of electric field sensitivity and dynamic range for different size loops are given in Table 4-3. Sensitivity of the sensors are measured as 98 µV/V/m, 183 µV/V/m and 246 µV/V/m for dipole lengths of 8mm, 16mm and 32mm, respectively and 50 µV/V/m for piezo only acousto-optic sensor. According to (33) and (34), the sensitivity should increase linearly with the dipole length. However, the sensitivity is increased by a factor of 1.35 from 16mm to 32mm dipole length and a factor of 1.87 from 8mm to 16mm dipole

length as opposed to expected factor of 2. This could be caused by the phase change in the magnetic field inside the TEM cell with respect to position. As the dipole size gets larger, the effect of destructive interreference of the electric field would be more pronounced. Once each sensor is characterized, this should not be a problem as the individual sensor response is highly linear over the tested magnetic field.

Table 4-3 Summary of electric field sensitivity and dynamic range for different size loops

Loop diameter	Sensitivity	Minimum detectable magnetic field	Dynamic range (bandwidth100kHz)
8 mm	98 μV/V/m	110 mV/m/√Hz	34 V/m- 81 kV/m
16 mm	183 μV/V/m	61 mV/m/√Hz	19 V/m- 43 kV/m
32 mm	246 μV/V/m	45 mV/m/√Hz	14 V/m- 32 kV/m
$LiNbO_3$ only	50 μV/V/m	224 mV/m/√Hz	70 V/m- 160 kV/m

The noise floor is measured at 5.6 μV/√Hz for this particular acousto-optic modulator. Thus, the minimum detectable electric fields for each sensor configuration are calculated as 110 mV/m/√Hz, 61 mV/m/√Hz and 45 mV/m/√Hz respectively. As the sensor starts to saturate around 8V, the dynamic range of the sensor is obtained as 117dB for a bandwidth of 1Hz. For a typical MRI system, the maximum bandwidth of the RF field will not exceed 100kHz. Thus, the measurable electric field range calculated as 34 V/m- 81

kV/m, 19 V/m- 43 kV/m and 14 V/m- 32 kV/m for dipole lengths of 8 mm, 16 mm and 32 mm respectively and 70 V/m-160 kV/m for piezoelectric transducer only configuration. Even though, when the acousto-optic modulator without any antenna has lower sensitivity, it might be preferable due to smaller sensor size and better spatial resolution. All the acousto-optic E fields sensor configurations have better performance than a similar size commercial probe (Speag E1TDS time domain E field probe) with a dynamic range of 2V/m-1kV/m for 1Hz bandwith that is widely used in MRI applications.

4.4.4 Directivity

The directivity of the electric field sensor is important to determine individual vector components of the RF field. Orthogonal dipoles can be used to measure the vector components of RF field if the sensor is directional. Radiation patter of a short dipole antenna is given in Figure 4-15.

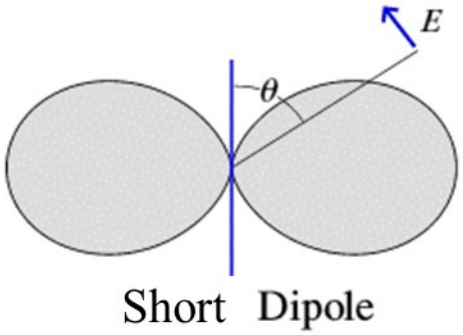

Figure 4-15 Radiation pattern of a short dipole antenna

The directivity of the sensor was measured by attaching the sensor on a rotational stage and SNR measurements were taken every 15°. The directivity of the sensor is

determined by the angle between the dipole and the E field vector. Both measured and calculated directivity of the sensor are given in Figure 4-16.

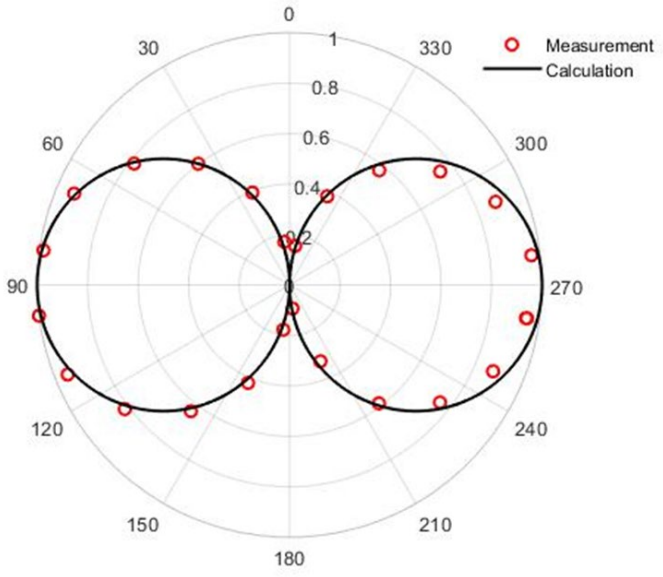

Figure 4-16 Directivity pattern of the electric field sensor.

The sensor is most sensitive when the E field is along the dipole length or perpendicular to the piezoelectric transducer. Sensor output has two orders of magnitude difference for perpendicular and longitudinal E fields. Thus, the sensor is directional and suitable for measurement of the vector components of E field.

4.4.5 Repeatability

The acousto-optic sensor was tested for repeatability and hysteresis. The sensor was fixed in the testing area of TEM cell and multiple measurements were taken: 5 consecutive measurements followed by 5 measurements every 10 minutes. Relative StD were calculated for output of 10 measurements, a summary is given in Table 4-4. Relative StD

for all sensor configurations were measured below 1% for 10 measurements per sensor. Moreover, hysteresis was not observed during the experiments. Thus, the fiber optic electric field sensor offers repeatable and reliable measurements.

Table 4-4 Relative standard deviations for electric field sensor for 10 measurements.

Dipole length	8 mm	16 mm	32 mm	$LiNbO_3$
Relative StD	0.63 %	0.46 %	0.78 %	0.23 %

In order to use the acousto-optic E field sensor for SAR measurement in biological tissues, following formula can be used for the conversion;

$$\mathrm{SAR} = \frac{\sigma\,|E|^2}{2\rho}\ \ [\mathrm{W/kg}]\ , \tag{35}$$

where σ is the electric conductivity of the tissue in S/m, ρ is tissue density in kg/m^3 and E is the induced rms electric field.

4.5 RF Field Mapping on a Pacemaker Lead Model

The motivation for the development of the acousto-optic RF field sensors is to measure the local RF hot spots on implants to prevent RF induced heating. We tested the sensor platform in both magnetic field and electric field sensor configurations on a pacemaker lead model to map the RF field distribution.

The pacemaker lead model is constructed using a long14 AWG copper wire with 1mm thick polymer insulation. A short, 2 mm section of the wire is exposed to simulate the end of an open pacemaker lead. A schematic of the test set-up is given in Figure 4-17. The pacemaker lead model is immersed in a large grounded saline filled tank and driven by an RF signal at 23.65 MHz to simulate RF induced field by a 0.55T MRI scanner. Acosuto-optic sensor was scanned over the wire in both configurations: as a magnetic field sensor with an 8mm dimeter coil and as an electrical field sensor without any attached. As a reference, measurements with a commercial magnetic field probe (Beehive 100A) and a commercial electric field probe (Beehive 100D) were taken.

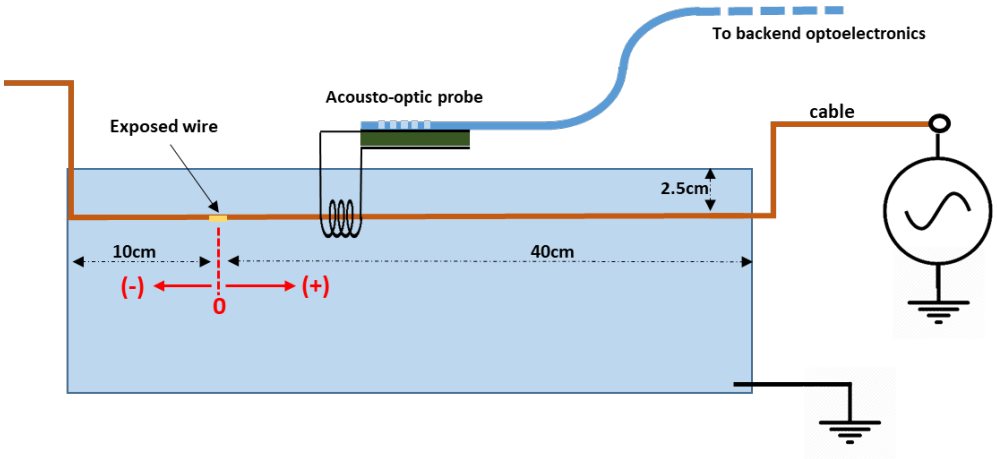

Figure 4-17 Experimental set-up for RF field mapping on a pacemaker lead model with acousto-optic probe.

The acousto-optic sensor in both magnetic field sensor and electric field sensor configurations as well as the commercial magnetic field sensor depict the local RF field variation at the exposed wire location with excellent correlation, shown in Figure 4-18. The commercial electric field sensor do not has adequate sensitivity to pick up reasonable E

field around the wire. Additionally, there was a strong coupling between the test set-up and the coax cable of the commercial E field sensor. It should be reminded that electromagnetic interference is not an issue with the optical fiber transmission.

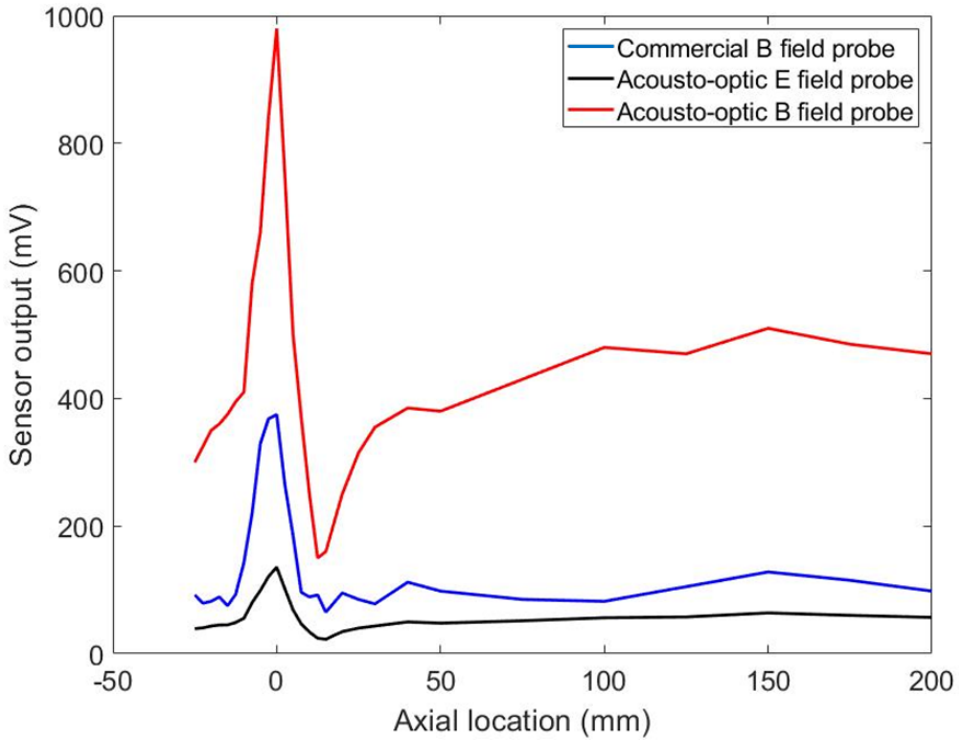

Figure 4-18 RF signal amplitude recorded on the acousto-optic sensor and reference commercial B field sensor as a function of distance on the wire. The exposed location is at the origin.

This experiment shows that the acousto-optic sensor can map the distribution of the induced RF field along an implant or on the human body for local SAR measurements as MRI dosimeter. Moreover, this platform can be used for the MRI safety evaluation of medical implants using the ISO 10974 standard [95] required by the FDA. It also shows that E field measurement at a single point on a conductor may not provide accurate

information on RF induced heating a long conductor. This spatial variation along conductive implant components becomes more important with smaller RF wavelengths related to emerging high field MRI scanners such as 3T, 7T and 11.4T [140].

4.6 Temperature Sensing with FBG

Temperature elevation can be measured rather than SAR (E field) measurement since the primary safety concern is RF induced heating. SAR measurement is used for MRI dosimetry as it is invasive to measure the temperature inside the body [141]. As mentioned earlier, FBG based sensors are widely used for temperature measurements by monitoring the slow shifts in the FBG spectrum, [82]. To demonstrate this capability using the same FBG sensors used for RF signal sensing, the π-FBG-2 grating was immersed in a water bath which slowly heated by a hot plate. Then, we measured the spectrum shift of the Bragg wavelength due to rising water temperature. Figure 4-1 shows that the local temperature around the FBG location can be measured using the slowly varying controller error signal in the wavelength controller. Temperature sensitivity of 10pm/^{o}C is observed from 25^{o}C to 50^{o}C.

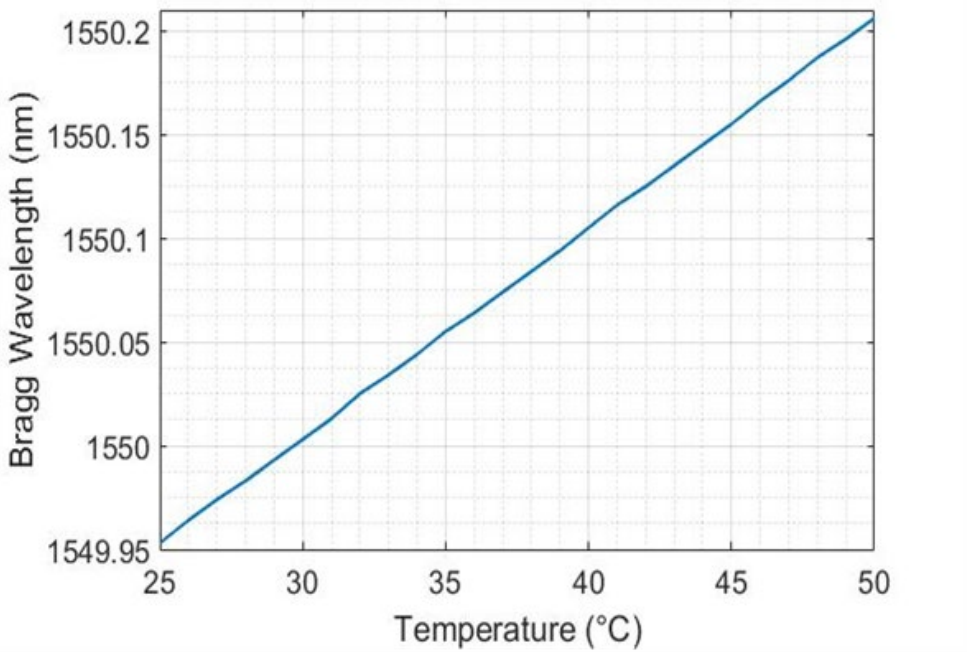

Figure 4-19 Bragg wavelength shift due to temperature change.

Therefore, using a calibration curve, the same acousto-optic sensor can be used as a multi-parameter RF safe active marker to monitor the local temperature as a slowly varying time signal while providing position tracking using the RF signal, which can be used in catheter based thermal/cyro ablation procedures.

4.7 Summary

This chapter was focused on the RF field sensing capabilities of the acousto-optic sensor. Detailed characterization tests were carried out with different antenna configurations. Sensitivity, directivity and repeatability tests were conducted for both E field sensors and B field sensors. RF field mapping on a pacemaker lead model was performed. Lastly, temperature sensing capability of the FBGs were demonstrated.

The major points of this chapter are listed as follows:

- Electric field sensing was achieved with short dipole antennas as well as using the piezoelectric transducer itself as a parallel plate antenna. Several antenna sizes were tested for sensitivity, directivity and repeatability. Sensitivity of 246μV/V/m and dynamic range of 0.224 V/V/m-160 kV/m were achieved, which is better than industry standard MRI dosimetry probe (Aim A1).
- Magnetic field sensing was achieved with small loop antennas. Several antenna sizes were tested for sensitivity, directivity and repeatability. Sensitivity of 1.84mV/nT and dynamic range of 25.4pT-18.2μT were achieved, which is better than industry standard MRI dosimetry probe (Aim A2).
- Moreover, excellent directivity and repeatability of both magnetic and electric field sensors was observed. (Aim A4)
- RF field mapping on a pacemaker lead model was performed. This experiment shows that the acousto-optic sensor can map the distribution of the induced RF field along an implant or on the human body for local SAR measurements as MRI dosimeter. (Aim A3)
- Temperature sensing capability of the FBGs was demonstrated. Feasibility of using the same acousto-optic sensor as a multi-parameter RF safe active marker to monitor both the local temperature and local SAR is shown. (Aim C6)

CHAPTER 5. DEVICE TRACKING UNDER MRI

5.1 Overview

The acousto-optic sensor was characterized for electric field and magnetic field measurements in the previous chapter. This chapter focuses on the use of acousto-optic modulation for device tracking. Small size multiturn loop antennas are used for localization. The acousto-optic sensor is integrated on catheters and tested in both phantom and animal studies for visibility.

5.2 Acousto-Optic Sensor Configuration for Device Tracking

Loop antennas have been used as active markers for device tracking. Thus, we tested the device tracking capability of the acousto-optic sensor with loop antennas. The small loop antennas have low sensitivity; thus, they will pick up MRI signals only in the immediate vicinity when placed inside the body. If the output of the loop antenna is connected to the MRI coil thus, in other words, if the loop antenna is used as receive only imaging coil, the constructed image will be that of the location of the coil. It will show up as a point marker in the MRI image when only the signal from the loop antenna is highlighted. A schematic overview of the acousto-optic tracking sensor with coil antenna and its connection with the MRI scanner is given in Figure 5-1.

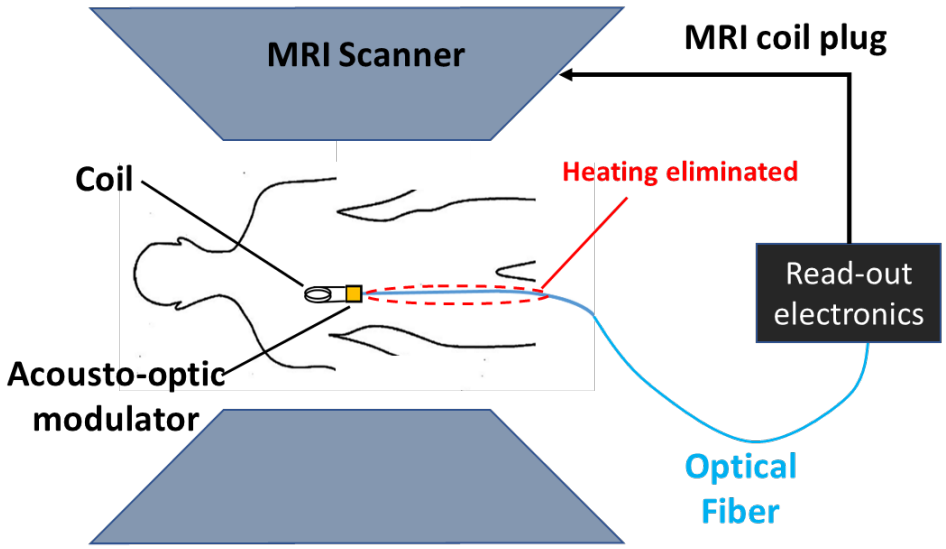

Figure 5-1 Schematic overview of the acousto-optic marker: an acousto-optic modulator converts the local MR signal received by the coil into optical signal, optical signal is carried out by a fiber optic to the read-out electronics which is connected to the coil plug of MRI as a separate channel.

Acousto-optic modulator with both 250MHz (π-FBG-1) and 50 MHz (π-FBG-2) bandwidth FBGs are used for MRI testing for device tracking purposes. Smaller size antennas are desired for better spatial localization. In order to increase SNR while keeping the size of the antenna small, multi turn loop antennas in solenoid form were used. 30 AWG insulated copper wire was wound into a tight-pitched solenoid coil with various diameters and number of turns. The acousto-optic sensor connected to a test coil with a diameter of 8mm and 12 turns is shown in Figure 5-2. Obviously, this coil used for calibration purposes and it is not suitable for actual device tracking due to its size.

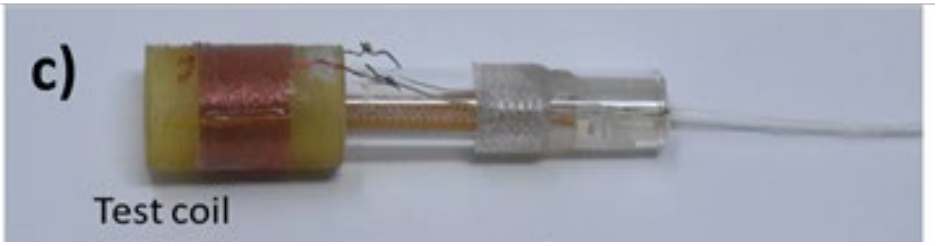

Figure 5-2 Acousto-optic sensor connected to a test coil with a diameter of 8mm and 12 turns.

8 F (2.4mm diameter) catheter blanks were used for in-vivo device tracking. The 30 AWG wire was hand wound to the distal end of the catheter blank and secured with minute amount of cyanoacrylate (super glue). Since the package of the acousto-optic modulator is relatively larger, the acousto-optic modulator was placed at the proximal end of the catheter. Very thin heat shrink tube is used for isolation and securing of the wire connection between the coil and the acousto-optic modulator. Distal end of a sample catheter with 8 turn single coil is shown in Figure 5-3. Note that, size of the package is determined by the glass tube housing rather than acousto-optic modulator itself.

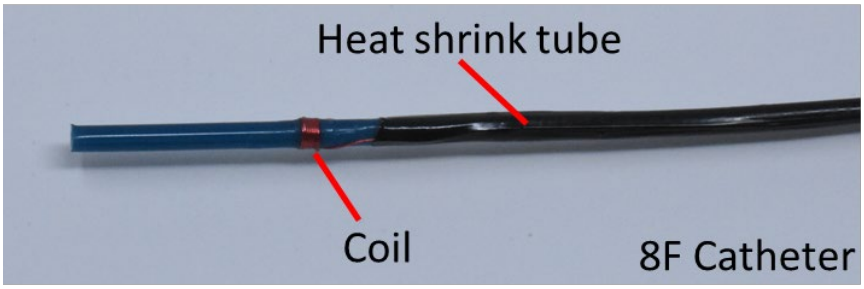

Figure 5-3 Distal end of a sample 8F catheter with 8 turn single coil.

5.3 Phantom Experiments

5.3.1 Sensor Characterization with RF Transmit Signal

In order to investigate the feasibility of device tracking, the acousto-optic sensors were used with RF transmission signal for signal analysis and functionality tests as RF transmission signal is much higher (~10^9) than the MRI signal emitted by the tissue. Moreover, the acousto-optic based sensors were also compared with conventional active markers; identical coils with cable connections matched to 50 Ω. MRI phantoms mimicking electromagnetic properties of tissues were used as the testing environment. A photo of the system inside MR room is provided in Figure 5-4. Note that photo detector and laser source are located in the control room, the received MR signal is carried out from the acousto-optic marker to photo detector by optical fiber.

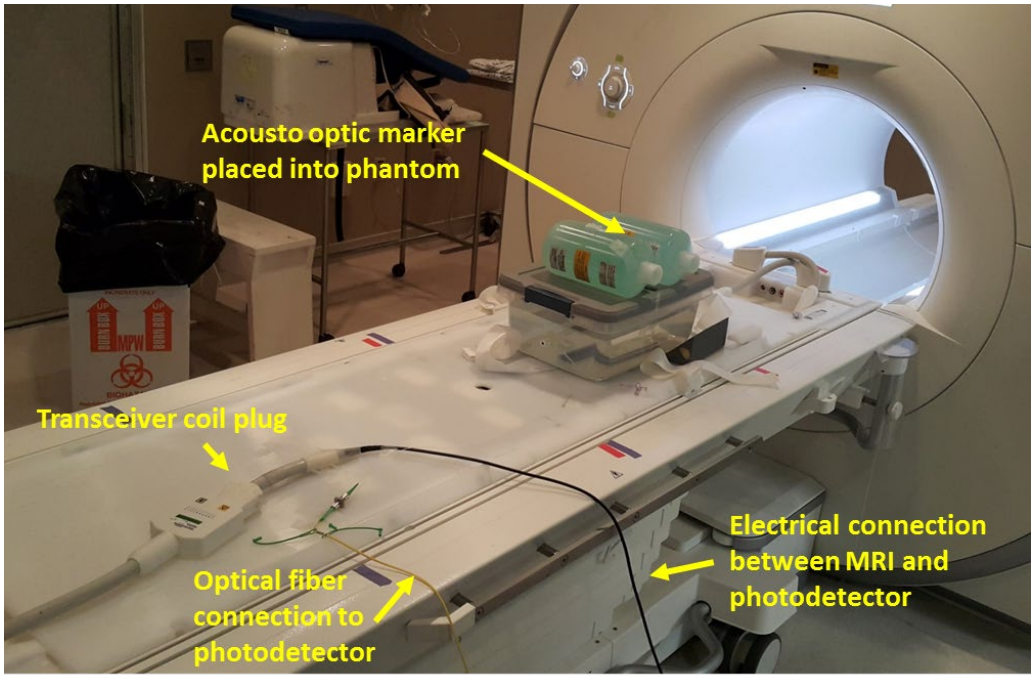

Figure 5-4 A photo of the system inside MR room.

5.3.1.1 Testing with 1.5T MRI Scanner

Acousto-optic sensor with π-FBG-1 was tested under a clinical 1.5T MRI scanner (Siemens Aera, Siemens Healthineers). Figure 5-5 a shows the AC signal at the output of photodetector and conventional active marker for RF transmit signal of an spin echo sequence. Acousto-optic sensor has a peak amplitude of 1.72 V whereas conventional marker has a peak amplitude of 50.7 V, which is 30 dB higher than acousto-optic sensor. However, when the frequency spectrum is analysed with normalized amplitudes,Figure 5-5 b; there is only 10 dB difference between signal to noise ratios (SNR) for a bandwidth of 100 kHz. SNR values are calculated as 57dB for the prototype and 67dB for the conventional active marker.

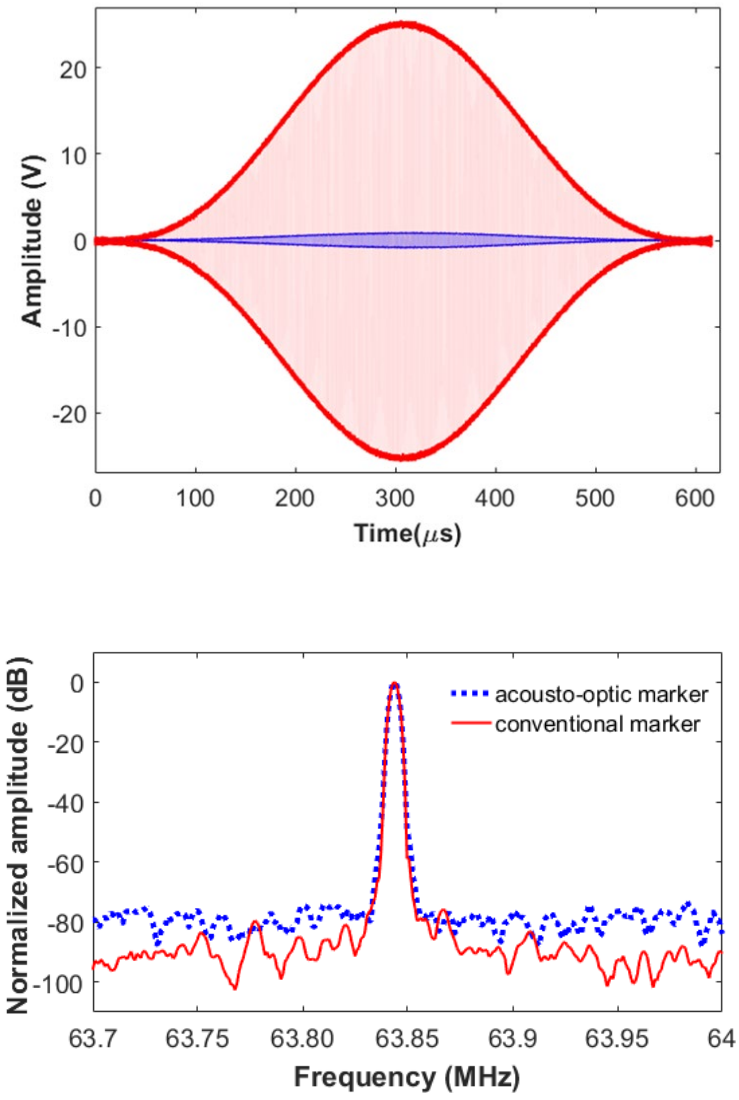

Figure 5-5 Comparison of π-FBG-1 based acousto-optic sensor output and conventional marker for a spin-echo RF transmit signal in time domain (top) and frequency domain (bottom).

The prototype was further tested for linearity. Flip-angle is an important parameter to improve image contrast during MRI and it is directly proportional to the received RF signal amplitude. The prototype was tested for different flip angle values without changing any other MRI parameter. Figure 5-6 compares the output signal from the acousto-optic

sensor for flip angles of 20º and 40 º. The peak frequencies of both signals are exactly the same since the location of the sensor was not changed. The amplitudes are linearly proportional; output for 20° flip angle is 75 mV whereas 40° flip angle results in 148mV.

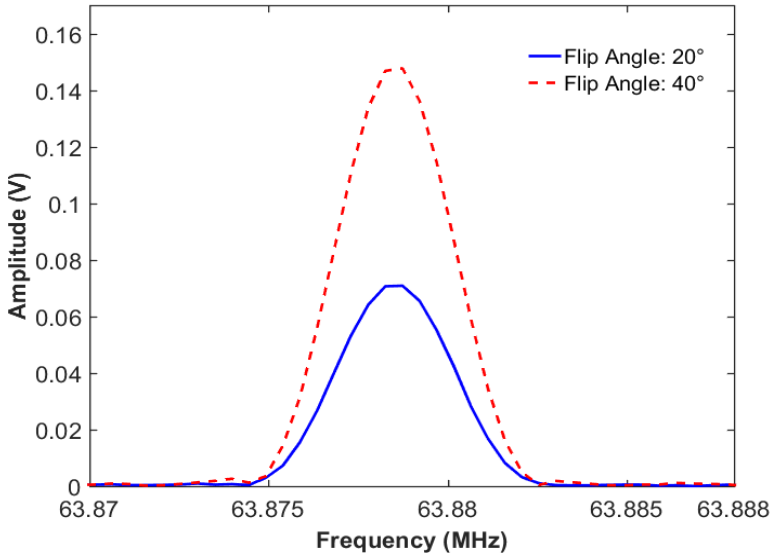

Figure 5-6 π-FBG-1 based acousto optic sensor output for flip angles 20 and 40.

The prototype sensor response was recorded for different flip angles ranging from 2° to 90°, shown in Figure 5-7. Flip angle with respect to sensor signal amplitude is linear with a slope of 3.7mV/°, except for the region where flip angle approaches to 90° and the amplitude of the sensor deviates from the linear region, refer to Chapter 3. In practice, small flip angle operation is favourable since higher flip angle sequences requires more time and elevates SAR values. When the sensor is used for tracking purposes with faster imaging sequences utilizing small flip angles, weak echo signal will not saturate the system.

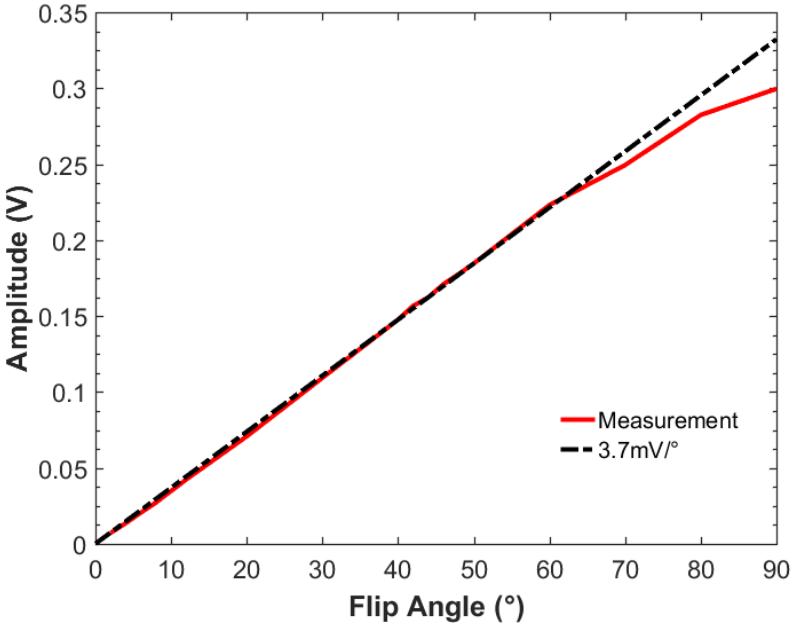

Figure 5-7 π-FBG-1 based acousto-optic sensor output vs flip angle.

Finally, acousto-optic sensor was tested and compared to an active marker for visibility in the MRI setting. A coil antenna a diameter of 3mm and length of 10mm with 40 turns was chosen to compensate for the lower sensitivity of π-FBG-1. A Gradient Echo (GRE) sequence with following parameters was used: Flip Angle, 90°:TR, 150 ms; TE, 3.4 ms for acousto-optic marker and Flip Angle, 15°; TR, 150ms; TE, 3.4 ms for active marker. Acquired MR images can be seen in Figure 5-8. In order to increase the visibility of acousto-optic sensor, an averaging of 32 was used. Locations of acousto-optic sensor and active marker are slightly shifted as both sensors and their corresponding coils were placed in same phantom side by side. MR image of acousto-optic sensor has a lower contrast compared to MR image of active marker due to lower amplitude and SNR. A better performing sensor is required for clinically practical device tracking.

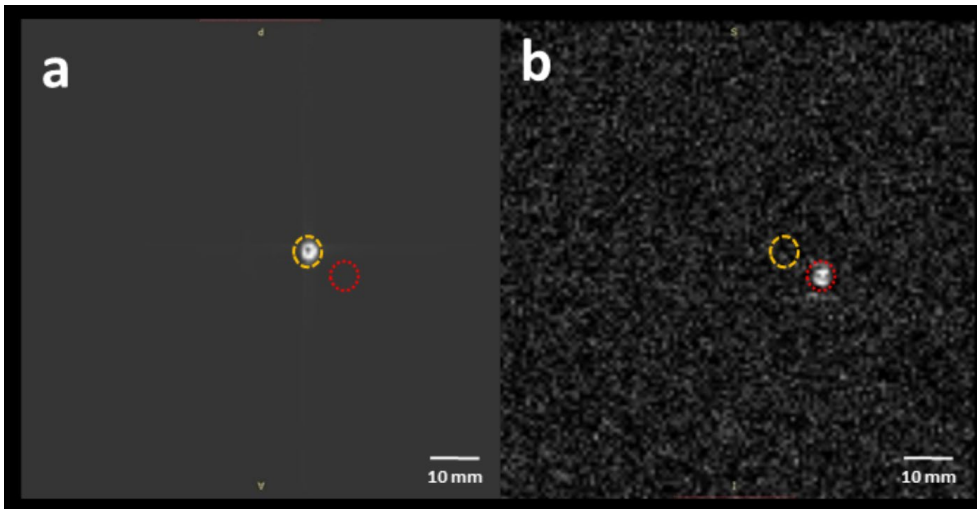

Figure 5-8 MR image of (a) conventional marker, (b) acousto-optic marker using a GRE sequence and the device receiver channel only. Locations of acousto-optic marker and conventional cable connected marker are highlighted with red and yellow circles respectively.

5.3.1.2 Testing with 0.55T MRI Scanner

Acousto-optic sensor with π-FBG-2 was tested under a prototype 0.55T MRI scanner (Siemens Aera, Siemens Healthineers) [142]. Note that, MRI signal level is reduced to lower Larmor frequency (23.65 MHz), however the electromechanical conversion efficiency of piezoelectric transducer is increased as it is operated around its first resonance rather than third harmonic. Moreover, π-FBG-2 is more sensitive than the π-FBG-1.

Figure 5-9 show the AC signal at the output of photodetector active marker for RF transmit signal of a spin echo sequence. π-FBG-2 based acousto-optic sensor output for flip angles 1, 5 and 10. Note that the acousto-optic sensor output starts to saturate after flip

angle of 10. Moreover, the π-FBG-2 based acousto-optic sensor has 16 dB higher SNR compared to a cable connected identical coil.

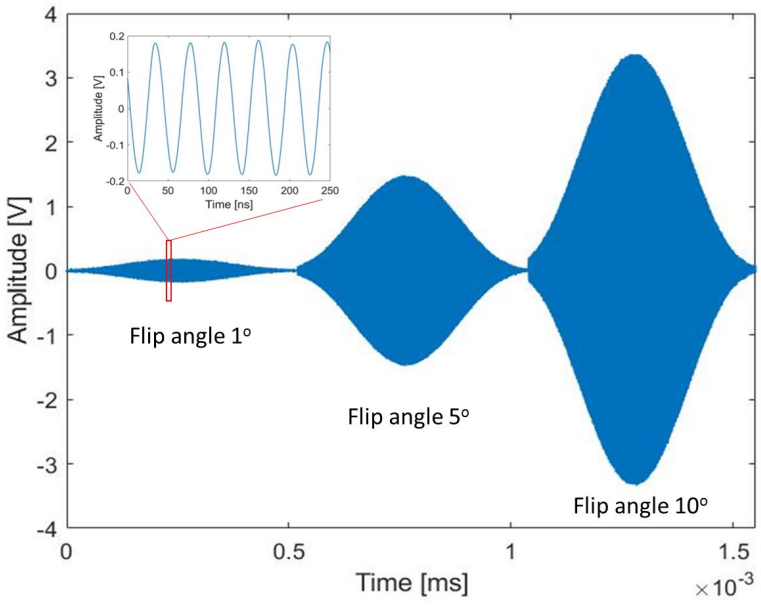

Figure 5-9 π-FBG-2 based acousto-optic sensor output for flip angles 1, 5 and 10. Note that the acousto-optic sensor output starts to saturate after flip angle of 10.

Similar to 1.5T phantom testing, π-FBG-2 based acousto-optic sensor was tested for visibility under MRI. A coil antenna a diameter of 2.4mm with 12 turns was used. A balanced steady state free precession (bSSFP) sequence with following parameters was used: Flip Angle, 90°; TR, 471 ms; TE, 1.7 ms; slice thickness, 10mm; bandwidth, 500 Hz/pixel and matrix size, 128 x 128. Note that, this imaging sequence is very fast (2 frame per second) and used for real time MRI guidance during interventional procedures. Acquired MR image can be seen in Figure 5-10. Note that the visibility is comparable to π-FBG-1 even though a fast imaging sequence is used.

Figure 5-10 MR image the π-FBG-2 based acousto-optic sensor using a fast bSSFP sequence and the device receiver channel only.

5.3.2 Phase Correction of FBG Response

The impact of phase nonlinearity of FBG sensor for position tracking during real-time MRI is observed when the bias point is changed due to finite response time of the wavelength controller. Since π-FBG-2 has higher nonlinearity, it was used to demonstrate and test a phase nonlinearity correction method.

The laser output was adjusted such that the maximum reflection corresponds to 10V voltage at the photodetector output. Bias was set to 4.5V for maximum amplitude sensitivity where the phase sensitivity of the π-FBG-2 is 24°/V. An analog phase shifter (SigaTek Model SF50A2) is used for phase correction. The DC voltage output from

photodetector is used for controlling the phase shifter. Since the phase shifter introduces 18o phase shift per Volt of control voltage input, a gain of 0.75 was applied to the DC voltage output of photodetector for proper phase correction. The schematic of the sensor with phase shifter inside MRI is given in Figure 5-11.

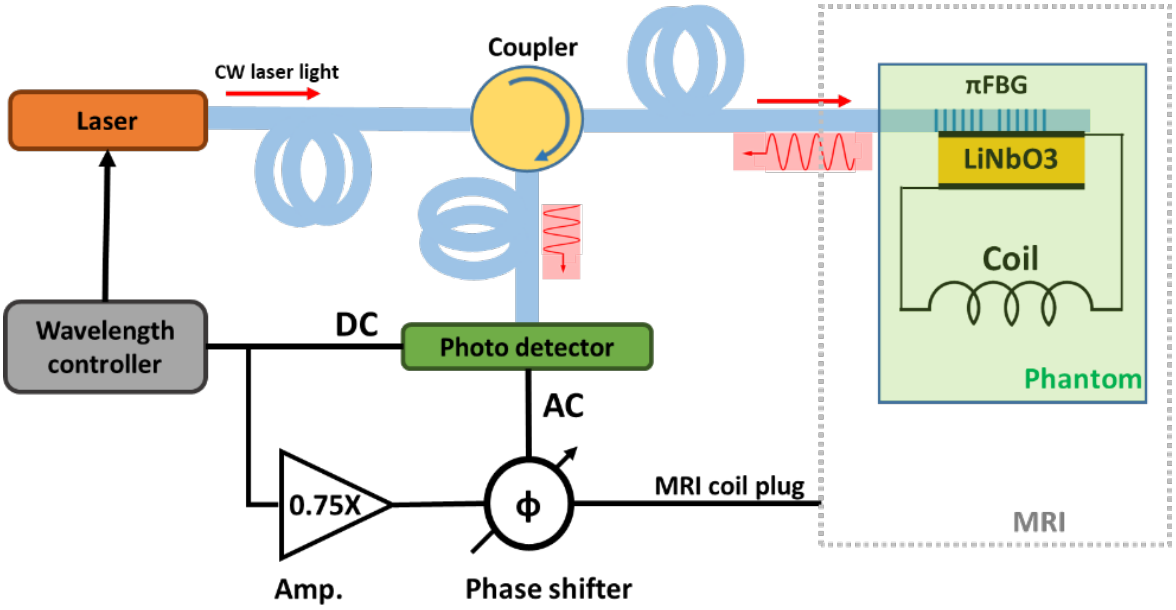

Figure 5-11 Schematic of the sensor with phase shifter inside MRI.

Same bSSFP sequence was used for imaging. Figure 5-12 a shows the MRI image of the acousto-optic sensor without the phase correction has a size of 5.6 mm with severe image distortion at the corners. Moreover, some lines of the coil image were missing which indicates the phase was distorted during the acquisition of MR signal associated with that particular region. On the other hand, as seen in Figure 5-12 b, the image of the coil was uniform with a size of 3.2 mm when phase correction was applied. These results indicate the importance of phase linearity for FBG based position sensing in MRI as predicted by

the careful modelling and characterization results and demonstrate that these artefacts can be corrected in real-time using proper phase shifting electronics.

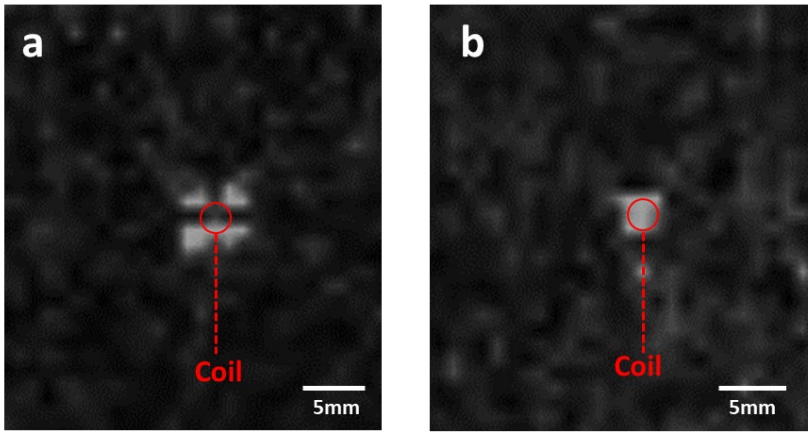

Figure 5-12 Image of acousto-optic sensor without phase correction (a) and with phase correction (b) under MRI.

5.3.3 RF Induced Heating

RF induced heating tests were performed under 0.55T MRI scanner which is relatively safer compared to higher field strength MRI systems. Acousto-optic sensor with a test antenna was placed in an acrylic phantom prepared according to the ASTM F2182 standard. A polyimide port was placed and fixed in contact with the wire using a polyester heat shrink tube. A fiber optic temperature probe (OpSens, Quebec, Canada) was placed inside the polyimide port. The temperature measurement set-up is shown in Figure 5-13. Temperature probe advanced maximally at first and manually pulled back slowly to find the hot spot under MRI. Temperature at the hot spot was recorded 30 seconds before the scan for determining a baseline and during the 180 seconds scans with 45 and 75-degree

flip angles. Moreover, RF induced heating tests were performed on a reference catheter with an identical coil while the device is connected to the scanner.

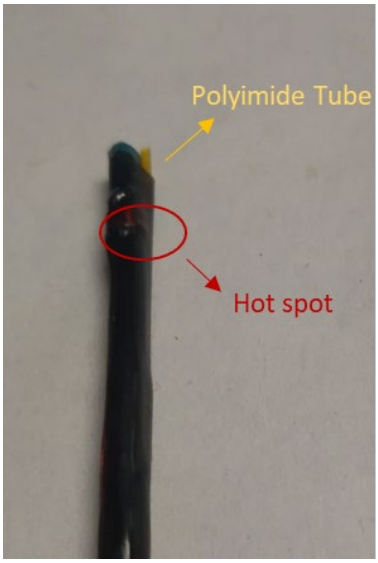

Figure 5-13 Temperature measurement set-up for RF induced heating on the catheter with a single coil antenna.

Temperature rises for both acousto-optic sensor and the reference catheters are given in Figure 5-14. The temperature immediately rises as soon as RF field is turned on and starts to saturate after 60 seconds. Both catheters have the highest temperature elevation for 75° flip angle, as expected. Temperature rises 2.6 ºC in the acousto-optic sensor, whereas reference catheter has a temperature increase of 20.4ºC. In a similar fashion, temperature rise of 0.8 ºC and 6.7ºC are observed on the acousto-optic sensor and reference catheter for 75° flip angle. The acousto-optic sensor reduced RF induced heating by a factor of 8 in this particular sensor configuration. The effect of RF induced heating on the sensor can be further reduced with an optimized antenna and sensor configuration.

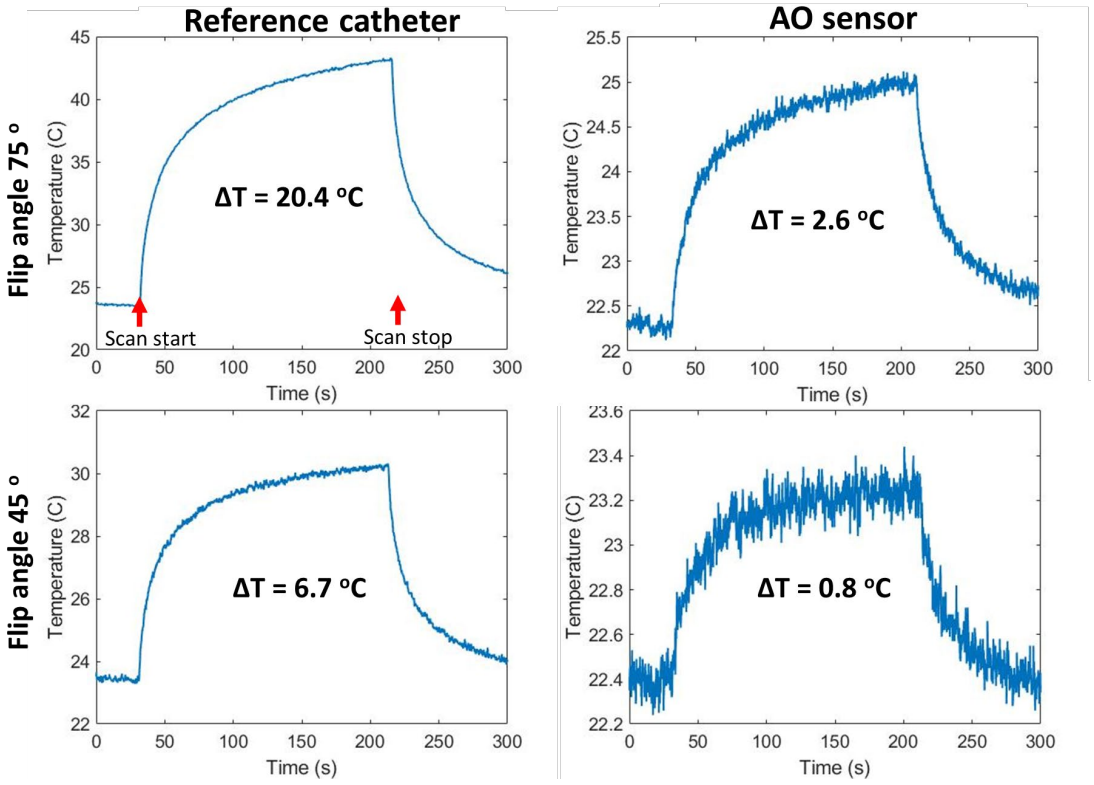

Figure 5-14 A comparison between the acousto-optic (AO) sensor and a reference catheter with cable connection for temperature rise due to RF transmit signal with flip angle of 45° and 75°.

5.3.4 Sensor Operation with Multiple Coils

Position and orientation of the catheter tip are two parameters used for tracking purposes. Position information of distal tip can be obtained from single coil. However, at least two active markers are required in order to get the orientation information of the catheter tip. Orientation information is especially important when catheter is guided through complex tortuous vasculatures.

In the acousto-optic tracking sensor, one way to obtain multiple location information is incorporating multiple coils. A straightforward approach is to use multiple sensors on the same fiber since multiple FBGs can easily be defined on single fiber. However, this approach will make the back-end optoelectronics more complicated as each FBG requires individual laser sources and controller units. Another approach is to connect multiple coils at different locations on the catheter to a single acousto-optic modulator since the modulator has wide enough operation bandwidth and linear response at the low power levels generated by the coils.

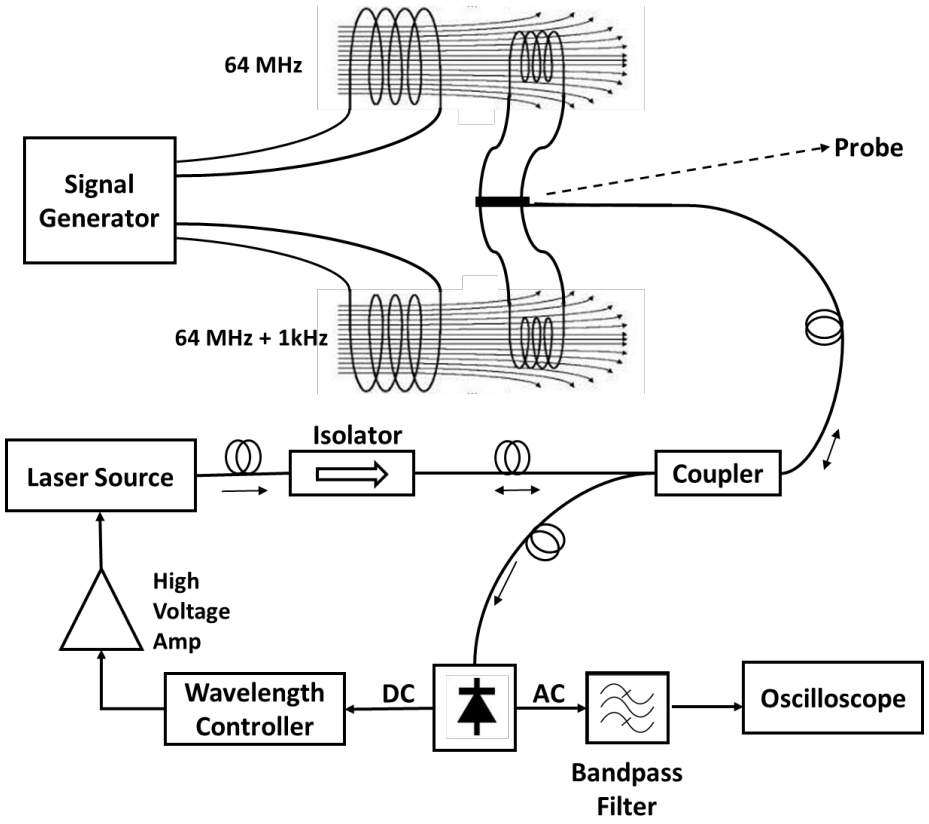

Figure 5-15 Experimental set-up for demonstration of multiple coil capability.

In order to investigate the multiple coil capability of the system, an experimental set-up is prepared as shown in Figure 5-15. Localized echo signals from the surrounding tissue inside the MRI system were emulated with large coils connected to a signal source. Large coils were air coupled to small coils of the probe. Two large coils are fed by the signal generator at the frequencies of 64 MHz and 64.001 MHz. 1 kHz frequency difference corresponds to a distance of 11.7 mm under 20mT/meter gradient field. Figure 5-16 shows the frequency spectrum of the captured signal showing peaks at 64 MHz and 64.001MHz, indicating the feasibility of multiple coil readout.

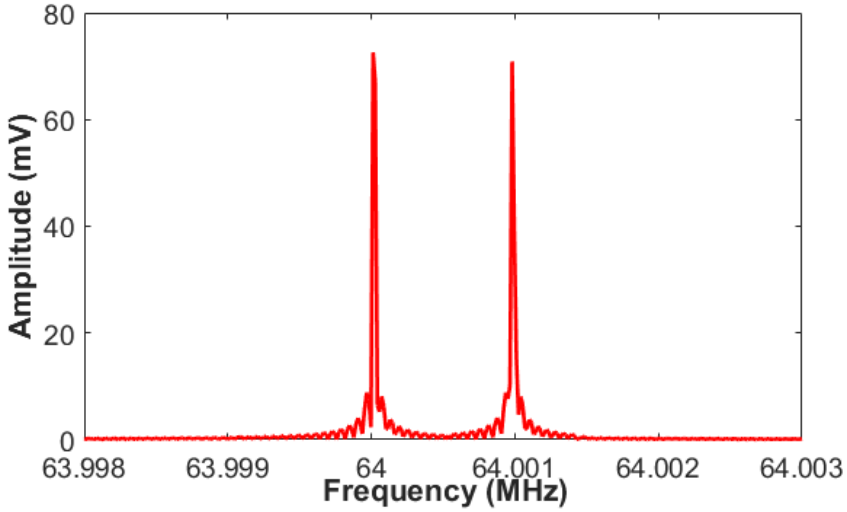

Figure 5-16 Frequency spectrum of the captured signal showing peaks at 64 MHz and 64.001 MHz

Finally, a catheter with two coils was prepared for the demonstration of multiple marker capability of the acousto-optic sensor. The markers are clearly visible in the image obtain by the 0.55T scanner. Distinct images of double coils allow determination of the

direction of the catheter tip in addition to location, which would help orient tools during interventions.

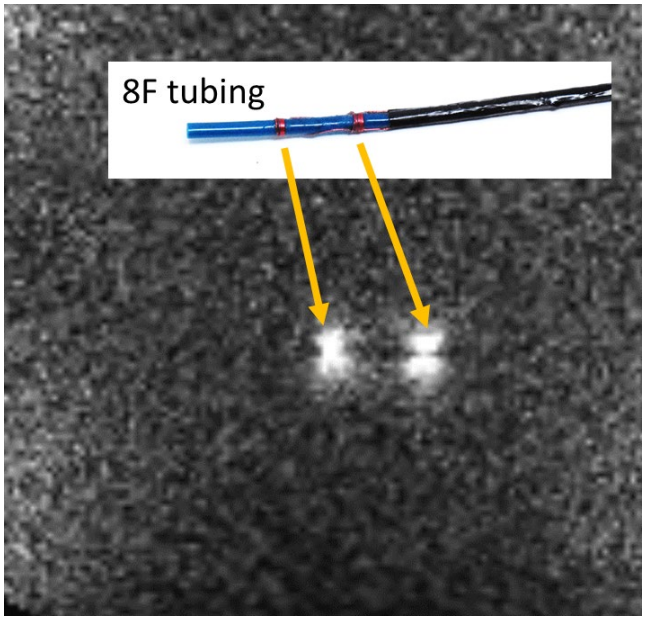

Figure 5-17) Image obtained from the catheter with two coils in MRI phantom using real time bSSFP sequence.

5.4 In-vivo Real Time Catheter Tracking

The acousto-optic sensor with π-FBG-2 was experiments. Large animal experiments were performed under the 0.55T interventional MRI suite. Photo of the interventional suite with a real time display and the test animal inside the 0.55T MRI scanner is shown in Figure 5-18.

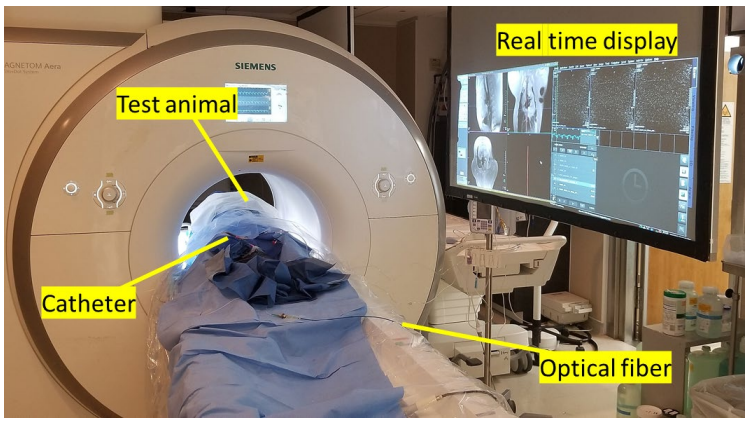

Figure 5-18 In-vivo imaging setup in the interventional MRI suite showing the test animal in the bore of the 0.55T MRI system.

A single coil 8F catheter with acousto-optic sensor was inserted into the femoral artery of an Yorkshire swine and progressed towards the heart. bSSFP sequence with following parameters was used: Flip Angle, 90°; TR, 471 ms; TE, 1.7 ms; slice thickness, 5mm; bandwidth, 500 Hz/pixel and matrix size, 256 x 256. A real-time image captured in two orthogonal planes is given in Figure 5-19. The signal from the acousto-optic sensor plug is overlaid on the relevant cross-sectional images in real-time using red color. The location of the marker is also indicated with a white arrow.

Tracking capability of the sensor was tested by moving the catheter to different locations. The catheter location was monitored through the real-time MRI images while the catheter was moved. Figure 5-20 show the catheter tip at two different locations. It is confirmed that the catheter location can be tracked in real-time using the acousto-optic sensor.

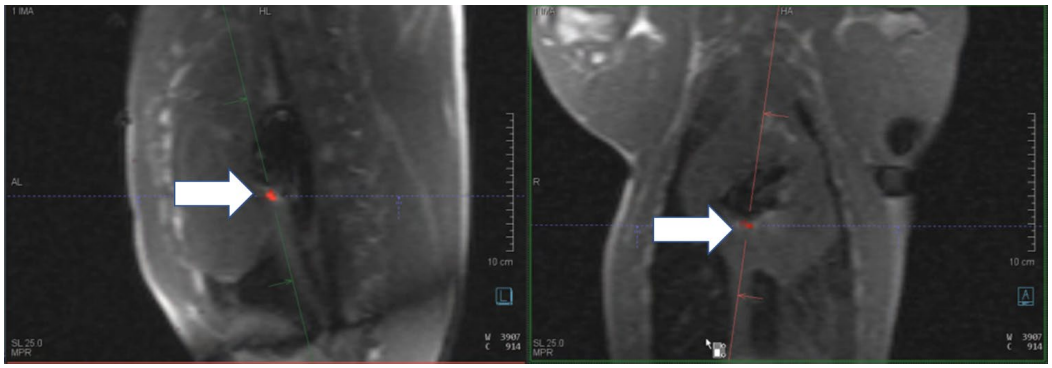

Figure 5-19 Real-time images captured in two orthogonal planes while the catheter tip placed in the heart.

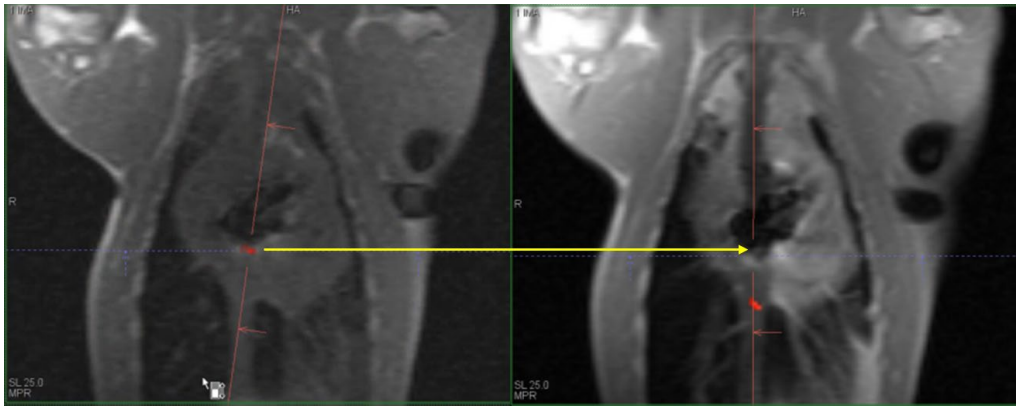

Figure 5-20 Catheter tracking demonstration: the MRI images show the catheter tip at two different locations.

These results, obtained in a challenging, SNR limiting low field MRI system, clearly demonstrate the potential of acousto-optic sensor as an RF safe tracking sensor for interventional MRI.

5.5 Summary

This chapter was focused on the device tracking capabilities of the acousto-optic sensor under MRI. Different acousto-optic sensors were characterized in 0.55T and 1.5T MRI systems for sensitivity and conspicuity. Multiple coil sensing and real-time phase correction was demonstrated. Lastly, catheter tracking capability of the acousto-optic sensor was demonstrated in an animal study. Hence, aim group B and C are achieved.

The major points of this chapter are listed as follows:

- Acousto-optic sensors with coil antennas were characterized in phantom studies with RF transmit signal. Sensor performance at 1.5T was hampered by low FBG sensitivity and reduced piezoelectric transducer performance due to third harmonic operation. On the other hand, in 0.55T system, an SNR improvement of 16dB was achieved by replacing the cable connection with the acousto-optic sensor.
- A phase correction scheme was successfully implemented to prevent image distortion due to phase nonlinearity of the acousto-optic sensor.
- Multiple marker capability of the acousto-optic sensor was demonstrated using a catheter with two coils.
- The acousto-optic sensor reduced temperature rise due to RF induced heating by a factor of 8 with respect to cable connection.
- Tracking of the catheter location was demonstrated in real-time using the acousto-optic sensor with a 0.55T MRI system.

CHAPTER 6. CONCLUSION AND FUTURE WORK

6.1 Conclusion

RF induced heating is a significant safety concern for all MRI procedures; from diagnostic imaging, patients with implants, to interventional procedures. Thus, RF field measurement with high SNR without image distortion and additional RF heating is key for evaluating MRI safety. Moreover, RF safe device tracking sensors are required for real time image guidance during interventional MRI procedures. Sensors with optical fiber transmission lines are desired as fiber optics have intrinsic electromagnetic immunity.

The objective of this research was to develop a sensing platform with optical fiber link for: 1) local RF field sensing for the assessment RF induced heating for diagnostic MRI, 2) device tracking for real time image guidance in interventional MRI procedures. This work introduced an acousto-optic modulator based sensor scheme with high SNR RF field sensing and real time device tracking capability for safer and more effective MRI procedures. All specific research aims given in Chapter 1 were achieved or feasibility was demonstrated through various tests and analysis.

6.2 Contributions

6.2.1 Fiber Bragg Grating based Acousto-optic Modulator

Different antenna topologies have been used in both RF field sensing and device tracking under MRI. In order to eliminate cables required for signal transmission from antenna, a fiber Bragg grating (FBG) based acousto-optic modulation is introduced as a

transduction mechanism. The electrical signal from the antenna is used for acoustic wave generation on the FBG via a mechanically coupled piezoelectric transducer. A highly sensitive transduction mechanism is required for the device tracking application as the available MRI signal to the device tracking sensor is quite low. Resonant nature of the piezoelectric transducer is utilized for increased sensitivity in the expense reduced operational bandwidth. Since RF fields in MRI are in a narrow band around the Larmor frequency, high quality factor piezoelectric transducers with their resonances at the Larmor frequency are desired for maximum sensitivity. Moreover, power up circuits and other complex electronics are not needed leading to a compact sensor package due to the passive operation mechanism of this acousto-optic modulator.

A hybrid model of the acousto-optic modulator is developed for design and optimization of sensors for different applications. A numerical model of FBG is derived using coupled mode theory and transfer matrix methods whereas piezoelectric transducer is modeled using FEA. Models are coupled through pressure field at the fiber core.

Effect of different parameters on FBG design is investigated through simulations. As phase shifted FBGs resulted in higher sensitivities with side slope detection read-out, π-FBGs with bandwidths of 0.4pm and 2pm are designed and later fabricated. Bulk and thin film piezoelectric transducers are investigated for acoustic field generation within the FBG. In the thin film piezoelectric transducer configuration, two distinct modes with resonances are predicted at 21MHz and 66MHz which are closer to Larmor frequencies of 0.55T (23.6MHz) and 1.5T MRI (63.86MHz) systems and can be easily tuned by adjusting layer thickness. A transduction gain of 683.7V/V is calculated for an optimized thin film

piezoelectric transducer coated FBG whereas maximum transduction gain of 8.75V/V is calculated for acousto-optic modulator with bulk piezo at 63.86MHz.

6.2.2 Model Validation Through Sensitivity and Linearity Analysis

A prototype acousto-optic modulator is fabricated with the previously designed FBGs and LiNbO3 bulk piezoelectric transducers. Model was first validated through spectral response of the FBGs which closely match with measured spectrum.

Pressure sensitivities of the FBGs were measured as 80mV/kPa for 0.4pm (50MHz) bandwidth FBG and 12mV/kPa for 2pm (250MHz) bandwidth, which are approximately half of the model predictions. These variations expected to be reduced with thin film configurations. Moreover, highest sensitivity was observed at 25% the bias point on the side slope contrary to widely accepted 50%. A linear relation between the phase and bias point was observed: the phase changes of 0.165^{o} per 1% bias change for 250MHz FBG and phase changes 0.48^{o} per 1% bias change for 50MHz FBG. This unwanted phase due to bias change needs to be corrected for device tracking application where the sensor used for image reconstruction and mili-radian range phase stability is needed for acceptable MRI image quality. Thus, a phase correction method was implemented for device tracking tests.

Lastly, the noise of the acousto-optic modulator is found to be dominated by the photo-detector noise and measured as 5.6 μV/√Hz which results in a dynamic range of 117dB/√Hz.

6.2.3 RF Field Sensing with the Acousto-optic Sensor

The acousto-optic sensor with different antenna configurations were used for RF field sensing. Electric field sensing was achieved with short dipole antennas as well as using the piezoelectric transducer itself as a parallel plate antenna. Several antenna sizes (8mm-32mm) were tested for sensitivity, directivity and repeatability. Sensitivity of 246μV/V/m and dynamic range of 0.224 V/V/m-160 kV/m were achieved. In a similar fashion, magnetic field sensing was achieved with small loop antennas. Several antenna sizes (2mm-8mm) were tested for sensitivity, directivity and repeatability. Sensitivity of 1.84mV/nT and dynamic range of 25.4pT-18.2μT were achieved. Moreover, excellent directivity and repeatability of both magnetic and electric field sensors was observed. These results are better than the industry standard MRI dosimetry probes for the 0.55T MRI system.

RF field mapping on a pacemaker lead model was performed This experiment shows that the acousto-optic sensor can map the distribution of the induced RF field along an implant or on the human body for local SAR measurements as MRI dosimeter. Moreover, temperature sensing capability of the FBGs was demonstrated proving feasibility of using the same acousto-optic sensor as a multi-parameter RF safe active marker to monitor both the local temperature and local SAR is shown.

6.2.4 Real-time Device Tracking under MRI

The acousto-optic modulator with a solenoid coil was used as an MRI marker for device tracking with both 0.55T and 1.5T MRI scanner. The acousto-optic sensor is first calibrated with RF transmit signals. The sensor with 250MHz FBG had a linear response

with respect to flip angle, whereas the sensor with 50MHz FBG output was saturated at flip angles above 10º. The sensor with 250MHz FBG had 10dB lower SNR compared to an identical with cable connection whereas sensor with 50MHz FBG had 16dB higher SNR compared to an identical with cable connection.

Visibility of the sensors were tested first tested in phantoms. Even though, the lower sensitivity sensor was visible under MRI, it required long imaging sequences with averaging. On the other hand, high sensitivity sensor was visible with real time imaging sequences (bSSFP sequence with 2 fps frame rate). In terms of RF safety, temperature increase at the coil, the only conductive part of the acousto-optic sensor, was monitored and less than 3ºC temperature increase was observed for a flip angle of 75º, whereas an identical coil with cable connection had over 20ºC temperature increase. Moreover, visibility of multiple coils on the same acousto-optic sensor was demonstrated for orientation capability. Hence the visibility and safety of the acousto-optic sensor was demonstrated in phantom studies.

Finally, the acousto-optic sensor was integrated on 8F catheter for in-vivo animal experiments. Large animal experiments were performed under the 0.55T interventional MRI suite. A single coil 8F catheter with acousto-optic sensor was inserted into the femoral artery of the animal and progressed into the heart. Tracking capability of the sensor was tested by moving the catheter to different locations and it is confirmed that the catheter location can be tracked in real-time using the acousto-optic sensor. These results, obtained in a challenging, SNR limiting low field MRI system, clearly demonstrate the potential of acousto-optic sensor as an RF safe active marker for interventional MRI.

In conclusion, this study is a unique demonstration of the acousto-optic sensing for different MRI applications. Overall, the sensors developed as part of this dissertation will form a critical step in improving the safety of MRI procedures to enable scanning of implant patients and development of next generation interventional MRI procedures. Some of the results presented in this thesis have been presented at several conferences and published in journal papers [149-150]. Manuscripts are being prepared at the moment for unpublished results and multiple abstracts are accepted for presentation at different conferences.

6.3 Significance and Impact

SAR can be estimated using complex simulations, experimental calorimetry through temperature measurements or scanner power measurements. Computer simulations are not feasible during individual clinical scans due to variation and complexity of human anatomy. Calorimetric methods are applicable with complex phantoms, but not for individual patients, and direct temperature measurements do not provide SAR directly as the local temperature on a patient's body is a complex function of circulation, tissue properties. The SAR concerns are amplified when patients with medical implants, which is a growing patient population. These patients require significantly more time in MRI suites and sometimes not scanned partly due to RF safety concerns. These significant limitations in clinical practice and research can be overcome with the acousto-optic sensor that directly measures E/B-field and temperature. If accurate real time SAR monitoring is achieved with the acousto-optic sensor, MRI sequences can be optimized for each patient. MRI scan times can be decreased by adjusting sequence parameters according to the SAR limits of the particular patient. More importantly, patients with pacemakers and other active

implants, who are currently not accepted for MRI scans, can be accommodated by optimizing the scan parameters to assure the safety of the patient with implant.

In the endovascular image-guided interventions, MRI is advantageous over other commonly-used imaging modalities (e.g., fluoroscopy and CT) due to its non-ionizing radiation characteristic and its ability to provide soft tissue contrast, tissue chemical composition, and functional information, including blood flow velocities, perfusion and diffusion, and tissue metabolomics. In interventional procedures, it is critically important to accurately and rapidly detect the actual location of the endovascular devices or catheters and also the site of the pathology to be treated. Active MR markers incorporate small coils or antennae connected to the scanner on separate channels through long transmission lines for device tracking or profiling purpose. Clinical grade active endovascular catheters and guidewires are nearing clinical reality, but before moving on clinical trials, the RF induced heating risk over long conductor components of the devices needs to be addressed. With increased operation frequency, these problems are more pronounced at high magnetic fields such as in 3T scanners. The acousto-optic sensor can provide efficient, practical and RF safe active markers adaptable to a wide range of available MRI compatible interventional devices which can enable further development and clinical translation of endovascular MRI guided interventions.

6.4 Recommendations for Future Work

The work presented in this dissertation introduced the acousto-optic sensor and demonstrated its feasibility for RF fields sensing and device tracking under MRI. The main motivation of this research is to enable safer and more effective MRI procedures. However,

the work done so far in this thesis work was limited to the simulations and feasibility studies in lab environment for field measurements; demonstration of visibility in phantom and animal studies. Thus, detailed clinical studies with phantom, animal and human models are required to correlate the local field measurements from the acousto-optic sensor and the local SAR. Local SAR mapping on pacemakers in phantom studies and in-situ patient studies are required to assess the capability of the acousto-optic sensor as a safety sensor. Moreover, the acousto-optic MR marker needs to be integrated on different interventional devices and needs to be tested in different applications. All of these tests and applications require high SNR, optimized sensor performance, robust and optimized packaging. The prototypes used in this study were built with mostly readily available components; thus, their performances are less than optimized. The sensor can be improved in multiple areas using the model and analysis tools presented in this work. Moreover, further characterization and testing of the system is required for translation of the research from laboratory to clinical settings.

6.4.1 Model Development for Optimized Antenna Designs

The model of the acousto-optic modulator is developed for FBG – piezoelectric transducer assembly and assumes the antenna as a voltage source. However, impedance of the antenna will affect the power transfer from the antenna to piezoelectric transducer: i.e. the power transfer between a piezoelectric transducer and a short dipole antenna with high impedance will be different than of a small loop antenna with low impedance. More importantly, a good electromagnetic antenna model coupled with acousto-optic modulator model will provide a robust design tool for sensor optimization. More advanced and complex antenna topologies can be implemented for better performance. Even, endoscopic

and intravascular MR imaging [143], [144] can be achieved with high antenna sensitivity and optimized acousto-optic modulator.

6.4.2 Thin Film Piezoelectric Coating on FBG

Piezoelectric thin film coating on the optical fiber provides more efficient pressure field generation and coupling compared to bulk piezoelectric transducers. Moreover, the size of the acousto-optic modulator can be further reduced to the size of the optical fiber enabling easier packaging and integration of the sensor with other devices. An optimized acousto-optic sensor design with thin film ZnO coating was proposed and 2 orders of magnitude sensitivity improvement was predicted with the model.

Even though, thin film deposition of the cylindrical optical fiber is challenging, several fabrication methods of piezoelectric coating on optical fibres has been reported in the literature. Standard micro fabrication techniques can be adopted such as sputtering [104], [145]. Indeed, we have performed some initial depositions trials of Aluminum Nitride (AlN) on optical fiber with low temperature sputtering, Scanning Electron Microscope (SEM) images are shown in Figure 6-1. Initial samples were short pieces of optical fiber since long FBG sensors with connecters could not be placed into the sputtering machine with its current configuration. A custom holder needs to be designed to accommodate the FBG sensors. Alternatively, sol-gel methods can be utilized which has been used on optical fibers [146]–[148] . Special equipment and clean room are not required for sol-gel method, however a thermal treatment (firing process) step is required for polycondensation which might erase or damage the gratings. In both methods,

fabricated devices need to be characterized through electral impedance and optical measurements to tune the material properties and optimize the deposition process.

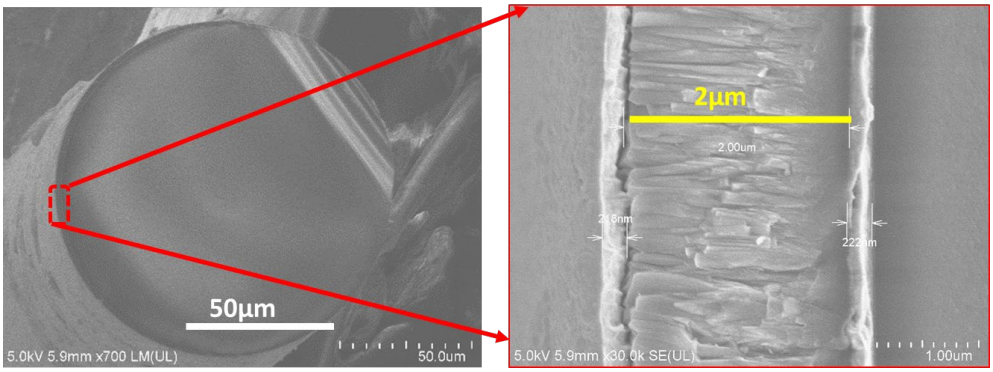

Figure 6-1 SEM images of 2um thick AlN coated optical fibers.

6.4.3 Acoustic Resonator Structures to Improve Sensitivity

Optimized thin film piezoelectric transducer have radial resonances which increases the sensitivity. Similarly, longitudinal resonances can be created by creating a resonant structure along the fiber by introducing geometric discontinuities (reflectors), such as abrupt changes in the optical fiber diameter by a introducing a notch (removal of fiber material) or adding a thick layer, Figure 6-2. These discontinuities result in large reflections creating a resonant cavity and effectively trap the acoustic energy and focus it on the FBG. Quality factor of the resonant structure can be adjusted by the structure shape, size and material selection.

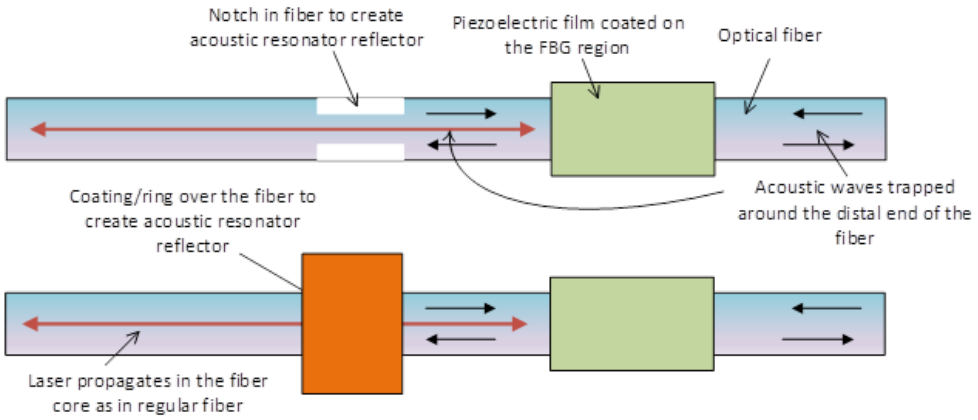

Figure 6-2 Two possible acoustic resonator structures. Top: A notch is formed in the optical fiber close to the FBG region. Bottom: A reflector can also be formed by increasing the diameter of the optical fiber by material deposition or by attaching a ring-like structure.

APPENDIX A. LASER WAVELENGTH CONTROLLER

The importance of the matching between the laser wavelength and Bragg wavelength is stressed many times throughout the thesis. Middle section of the side slope in the notch of FBG spectrum offers a linear operating region and a laser wavelength controller is needed to keep the laser wavelength in the linear operating region of the FBG spectrum. Wavelength of the FBG can shift due to operating conditions such as temperature and mechanical load on FBG as well as high amplitude acoustic noise. Thus, a wavelength controller was designed based on an op-amp proportional-integral (PI) controller, schematic is shown in Figure A-1.

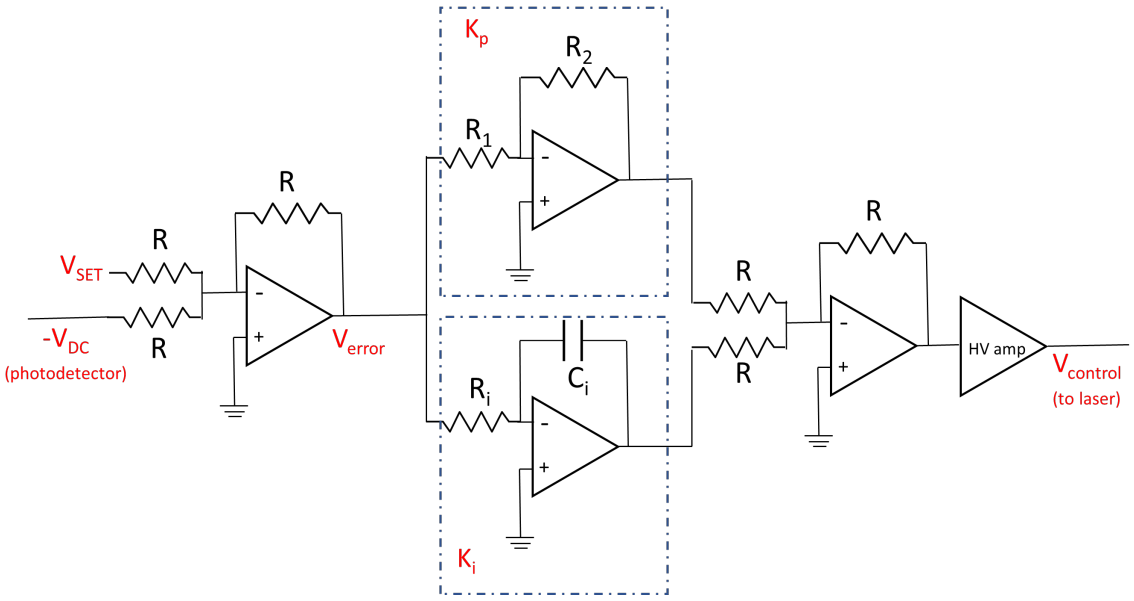

Figure A-1 Op-amp based laser wavelength controller.

The wavelength of the laser source is initially adjusted to desired point on the linear operating region of the FBG via temperature control on the laser source. A triangular wave as a control signal can be used in order to find the center notch of the FBG. The laser wavelength will be passing over the notch many times (100Hz triangular wave gives the optimum result with the current system) which will be easier to observe compared to simply scanning the laser wavelength once. DC output from the photodetector is used to track the power level of the reflected light from FBG. Dynamic changes in the FBG spectrum are tracked via piezoelectric wavelength adjustment channel in the laser source. Wavelength controller compares the DC output level with the set bias value and creates an error signal (V_{error}) in the presence of a mismatch. Error signal is first amplified by a high voltage amplifier (Trek Inc. Model 2205) and then used for driving the piezoelectric actuator of the laser source. The PI controller parameters are initially determined using a Simulink model of the back-end optoelectronics. Moreover, the controller parameters were further fined tuned for each type of FBG sensor. The parameters are calculated using;

$$K_p = \frac{R_1}{R_2} \tag{36}$$

$$K_i = \frac{1}{R_i C_i} \tag{37}$$

Where K_p is proportional gain and K_i is integral gain. Gains of 0.2 and 100 are calculated using the Simulink model for K_p and K_i respectively. Further optimization might be needed for the particular sensor if the ambient acoustic noise is high, i.e. in fast gradient

echo sequences. High quality potentiometers are used for R_1 and R_2 resistors for easy and reliable gain adjustments.

Wavelength controller can track wavelength changes up to 20 kHz, which covers most of the acoustic noise due to gradient fields. The controller speed is limited by the piezo-electric control of the laser. Note that, wavelength change created by mechanical loading and temperature changes on the FBG sensor has much lower frequency and are readily adjusted for by the controller. In the experiments, the bias point on the side slope was set to 50% of the maximum reflection. The controller can be

APPENDIX B. MATLAB CODE FOR FBG MODEL

The following MATLAB scripts were used for FBG model implementation.

MATLAB script for transfer matrix calculation:

```
function [F] = F_matrix(lambda,design_lambda,neff,dn,dn_dc,delta_z)
    % Coupled-mode Theory
    kappa=(pi./lambda)*dn; % AC coupling coefficient
    lambda_detune = 2*pi*neff*(1/lambda-1/design_lambda); % DC coupling coeff.
    sigma_dc = (2*pi./lambda).*dn_dc;
    sigma = lambda_detune + sigma_dc;  % no chirping
    gamma = sqrt(kappa^2-sigma^2);
    % F matrices
    F11 = cosh(gamma*delta_z)-1i*sigma./gamma.*sinh(gamma*delta_z);
    F22 = conj(F11);
    F12 = -1i*kappa./gamma.*sinh(gamma.*delta_z);
    F21 = conj(F12);
    F = [F11 F12; F21 F22];
end
```

MATLAB script for spectrum calculations:

```
function reflection = FBG_spectra(bandwidth, max_stress,lambda_array )
    if bandwidth == 250;
        dn = 37e-5;  % Induced ac index change
    else if bandwidth == 50;
        dn = 48.5e-5;  % Induced ac index change
    else
        disp('choose either 50MHz or 250MHz for FBG bandwith')
    end
    % optical parameters
        L = 8e-3;   % Grating Length (m)
        design_lambda = 1550e-9; %  wavelength (m)
        nco=1.445; % nco-core index
        ncl=1.444; % ncl-cladding index
        dn_dc = 0; %no apodization
        phase = pi; % phase shift
        neff = nco; %effective index
    % Grating parameters
        period_grating=design_lambda/(2*neff); % Grating period
        z_n = floor(L/period_grating/100);
        delta_z = L/z_n; %Length of uniform segment
```

```
z = linspace(-L/2,L/2,z_n);

n_apo = dn*normpdf(z,0,max(z)/3)/max(normpdf(z,0,max(z)/3)); % apodization profile


% mechanical parameters

v_us = 3764;  % speed of sound in the fiber

us_freq = 23.65e6; %acoustic frequency

lambda_us = v_us/us_freq; %acoustic wavelength

E_fiber = 70e9; % Young modulus of fiber

phase_us = pi/2; % Phase of acoustic wave

Vpoisson = 0.25; % Poisson ratio

P11 = 0.113; % Acousto-optic coefficents

P12 = 0.252;

% Pressure distribution – choose one option below

stress = max_stress*ones(size(z)); % uniform field

stress = zeros(size(z)); % no input field

stress(57-10:93-10) = max_stress; % pressure on a selected area on the FBG

stress = max_stress * sin(2*pi/lambda_us*z+phase_us); % acoustic wave along the fiber length
```

```
        % Induced refractuve index changes due to pressure

        n_elasto = nco^3*stress*(1-2*Vpoisson)*(P11 + 2*P12)/(2*E_fiber); % elaso-
optic effect

        z_geo = -(1-2*Vpoisson)*period_grating*stress/E_fiber; % geometric effect


%FBG spectrum calculation

        reflection = zeros(length(lambda_array),1);

        transmission = zeros(length(lambda_array),1);

        F = eye(2);
for ii = 1:length(lambda_array)

        lambda = lambda_array(ii);

         for kk = 1:z_n

                dn_us =  n_elasto(kk)+n_geo(kk) ;

                dn_dc = dn_us;

                neff = nco + dn_dc;

                %dn = n_apo(kk); % use it when apodization is present

                design_lambda = (period_grating+z_geo(kk))*2*neff;

                 if  kk == floor(z_n/2)

                 %phase shift

                F_phase = [exp(-1i*phase/2) 0; 0 exp(1i*phase/2)];

                F1 = F_phase*F_matrix(lambda,design_lambda,neff,dn,dn_dc,delta_z);
```

```
            else
            % Coupled-mode Theory
            F1 = F_matrix(lambda,design_lambda,neff,dn,dn_dc,delta_z);
            end
            F = F1*F;
        end
            reflection(ii) = -F(2,1)./F(2,2);
            transmission(ii) = F(1,1)-F(2,1)*F(1,2)/F(2,2);
            F = eye(2);
end


end
```

Sample MATLAB script for sensitivity calculation using the FBG_spectra function

```
%calculate the whole reflection spectrum for inspection
bandwidth = 50;
stress = 0;
lambda_start = 1549.998e-9;
lambda_end = 1550.002e-9;
lambda_n = 1e4;
lambda_array = linspace(lambda_start,lambda_end,lambda_n);
```

```
reflection = FBG_spectra(bandwidth, stress,lambda_array );
PDout = 10*abs(reflection).^2;

%Inspect the spectrum and
 figure
 plot(lambda_array,PDout);
 title('Spectra for 50MHz');
 xlabel('Wavelength(m)');
 ylabel('Reflection %');

%choose the bias point on the side slope
bias_ind = 5500; %50MHz

% Acoustic wave definition
max_stress = 1e3;
freq = 63.86e6;
t_n = 1000;
time = linspace(0,19*1/freq,t_n);
stress = max_stress * sin(2*pi*freq*time);
ACsig = zeros(length(bias_ind),t_n);
plot(time/1e-9,stress/max_stress);

%Calculate the optical modulation
   for ii = 1:t_n
      lambda = lambda_array(bias_ind);
```

```
    ref = FBG_time(bandwidth, stress(ii),lambda);
    ACsig(ii) = 10*abs(ref).^2;
  end

plot(time,10*(ACsig-mean(ACsig)));
title('1kPa');
xlabel('Time(s)');
ylabel('Amplitude (V)');

% Pressure sensitivity calculation
Vout = max(ACsig)-min(ACsig)
Sensitivity = Vout/max_stress
```

REFERENCES

[1] E. M. Haacke, R. W. Brown, M. R. Thompson, and R. Venkatesan, Magnetic Resonance Imaging: Physical Principles and Sequence Design. Wiley, 1999.

[2] "MRI Cutaway." [Online]. Available: https://science.howstuffworks.com/mri1.htm.

[3] C. Z. Cooley, "Portable Low-Cost Magnetic Resonance Imaging," 2014.

[4] H. C. Torrey, "Bloch equations with diffusion terms," Phys. Rev., vol. 104, no. 3, p. 563, 1956.

[5] A. D. Elster [Online]. Available: http://mriquestions.com/what-is-a-gradient.html

[6] "MR imaging." [Online]. Available: http://www.diffusion-mri.com/phd/PhDch2.html.

[7] M. de Rooij, E. H. J. Hamoen, J. J. Fütterer, J. O. Barentsz, and M. M. Rovers, "Accuracy of multiparametric MRI for prostate cancer detection: a meta-analysis," Am. J. Roentgenol., vol. 202, no. 2, pp. 343–351, 2014.

[8] R. Bammer, "Basic principles of diffusion-weighted imaging," Eur. J. Radiol., vol. 45, no. 3, pp. 169–184, 2003.

[9] D. J. Heeger and D. Ress, "What does fMRI tell us about neuronal activity?," Nat. Rev. Neurosci., vol. 3, no. 2, pp. 142–151, 2002.

[10] W. M. Wells, W. E. L. Grimson, R. Kikinis, and F. A. Jolesz, "Adaptive segmentation of MRI data," IEEE Trans. Med. Imaging, vol. 15, no. 4, pp. 429–442, 1996.

[11] M. F. Dempsey, B. Condon, and D. M. Hadley, "MRI safety review," Semin. Ultrasound CT MRI, vol. 23, no. 5, pp. 392–401, 2002.

[12] M. J. Dawson, Paul Lauterbur and the Invention of MRI. MIT Press, 2013.

[13] R. P., “The Basic Textbook of the European Magnetic Resonance Forum.” 2017.

[14] D. Kessel and I. Robertson, Interventional Radiology: A Survival Guide E-Book. Elsevier Health Sciences, 2016.

[15] A. A. Bravo, S. G. Sheth, and S. Chopra, “Liver biopsy,” N. Engl. J. Med., vol. 344, no. 7, pp. 495–500, 2001.

[16] W. Grossman, “Cardiac catheterization and angiography,” 1986.

[17] J. F. Thompson, P. Hersey, and E. Wachter, “Chemoablation of metastatic melanoma using intralesional Rose Bengal,” Melanoma Res., vol. 18, no. 6, pp. 405–411, 2008.

[18] C. T. Dotter, “Catheter biopsy experimental technic for transvenous liver biopsy,” Radiology, vol. 82, no. 2, pp. 312–314, 1964.

[19] P. Kolh, A. Kerzmann, C. Honore, L. Comte, and R. Limet, “Aortic valve surgery in octogenarians: predictive factors for operative and long-term results,” Eur. J. cardio-thoracic Surg., vol. 31, no. 4, pp. 600–606, 2007.

[20] R. J. Lederman, W. W. O’Neill, and A. B. Greenbaum, “Transcaval access for TAVR across a polyester aortic graft,” Catheter. Cardiovasc. Interv., vol. 85, no. 7, pp. 1270–1273, 2015.

[21] “Heart Surgery - Aortic Valve Replacement.” [Online]. Available: https://www.alamy.com/heart-surgery-aortic-valve-replacement-image7712020.html

[22] “TAVR.” [Online]. Available: https://www.mayoclinic.org/tests-procedures/aortic-valve-repair-aortic-valve-replacement/about/pac-20385093

[23] P. B. Persson, P. Hansell, and P. Liss, “Pathophysiology of contrast medium–induced nephropathy,” Kidney Int., vol. 68, no. 1, pp. 14–22, 2005.

[24] E. P. Efstathopoulos et al., “Medical personnel and patient dosimetry during coronary angiography and intervention.,” Phys. Med. Biol., vol. 48, no. 18, pp. 3059–68, 2003.

[25] L. Renaud, “A 5-y follow-up of the radiation exposure to in-room personnel during cardiac catheterization.,” Health Phys., vol. 62, no. 1, pp. 10–15, Jan. 1992.

[26] I. Smith, J. Cameron, K. L. Mengersen, and J. T. Rivers, “Evaluation of coronary angiographic projections to balance the clinical yield with the radiation risk,” Br. J. Radiol., vol. 85, no. 1017, pp. 722–728, 2012.

[27] G. BEDETTI, N. BOTTO, M. G. ANDREASSI, C. TRAINO, E. VANO, and E. PICANO, “Cumulative patient effective dose in cardiology,” Br. J. Radiol., vol. 81, no. 969, pp. 699–705, Sep. 2008.

[28] J. M. K. Mislow, A. J. Golby, and P. M. Black, “Origins of intraoperative MRI,” Neurosurg. Clin. N. Am., vol. 20, no. 2, pp. 137–146, Apr. 2009.

[29] R. T. Blanco, R. Ojala, J. Kariniemi, J. Perälä, J. Niinimäki, and O. Tervonen, “Interventional and intraoperative MRI at low field scanner - A review,” Eur. J. Radiol., vol. 56, no. 2, pp. 130–142, 2005.

[30] A. Z. Faranesh, M. Hansen, T. Rogers, and R. J. Lederman, “Interactive black blood preparation for interventional cardiovascular MRI.,” J. Cardiovasc. Magn. Reson. Off. J. Soc. Cardiovasc. Magn. Reson., vol. 16, no. Suppl 1, pp. P32–P32, 2014.

[31] A. D. Scott, R. Boubertakh, M. J. Birch, and M. E. Miquel, “Towards clinical assessment of velopharyngeal closure using MRI: evaluation of real-time MRI sequences at 1.5 and 3 T,” Br. J. Radiol., vol. 85, no. 1019, pp. e1083–e1092, 2012.

[32] S. R. Yutzy and J. L. Duerk, “Pulse sequences and system interfaces for interventional and real-time MRI,” J. Magn. Reson. Imaging An Off. J. Int. Soc. Magn. Reson. Med., vol. 27, no. 2, pp. 267–275, 2008.

[33] F. Settecase, A. J. Martin, P. Lillaney, A. Losey, and S. W. Hetts, “Magnetic Resonance-Guided Passive Catheter Tracking for Endovascular Therapy,” Magn. Reson. Imaging Clin. N. Am., vol. 23, no. 4, pp. 591–605, Nov. 2015.

[34] D. Grainger, “Safety Guidelines for Magnetic Resonance Imaging Equipment in Clinical Use,” 2015.

[35] J. A. S. Brookes, “Magnetic resonance-compatible needle.” Google Patents, Jul-2001.

[36] P. Kulkarni, S. Sikander, P. Biswas, S. Frawley, and S.-E. Song, “Review of Robotic Needle Guide Systems for Percutaneous Intervention,” Ann. Biomed. Eng., vol. 47, no. 12, pp. 2489–2513, 2019.

[37] C. K. Gooden, “Anesthesia for magnetic resonance imaging,” Curr. Opin. Anesthesiol., vol. 17, no. 4, 2004.

[38] J. Kettenbach et al., “Interventional and intraoperative magnetic resonance imaging,” Annu. Rev. Biomed. Eng., vol. 2, no. 1, pp. 661–690, 2000.

[39] M. O. Köhler et al., “Volumetric HIFU ablation under 3D guidance of rapid MRI thermometry,” Med. Phys., vol. 36, no. 8, pp. 3521–3535, 2009.

[40] S. G. Nour and J. S. Lewin, “Creating a Clinical Interventional MRI Service,” Top. Magn. Reson. Imaging, vol. 27, no. 1, 2018.

[41] J. Barkhausen et al., “White paper: Interventional MRI: Current status and potential for development considering economic perspectives, Part 1: General application,” RoFo Fortschritte auf dem Gebiet der Rontgenstrahlen und der Bildgeb. Verfahren, vol. 189, no. 7, pp. 611–622, 2017.

[42] T. Rogers et al., “Real-Time Magnetic Resonance Imaging Guidance Improves the Diagnostic Yield of Endomyocardial Biopsy,” JACC Basic to Transl. Sci., vol. 1, no. 5, pp. 376–383, 2016.

[43] J. L. Duerk, E. Y. Wong, and J. S. Lewin, “A brief review of hardware for catheter tracking in magnetic resonance imaging,” Magn. Reson. Mater. Physics, Biol. Med., vol. 13, no. 3, pp. 199–208, 2002.

[44] C. J. Bakker, R. M. Hoogeveen, W. F. Hurtak, J. J. van Vaals, M. A. Viergever, and W. P. Mali, “MR-guided endovascular interventions: susceptibility-based catheter and near-real-time imaging technique.,” Radiology, vol. 202, no. 1, pp. 273–276, Jan. 1997.

[45] K. Ratnayaka et al., “Real-time MRI-guided right heart catheterization in adults using passive catheters,” Eur. Heart J., vol. 34, no. 5, pp. 380–389, Feb. 2013.

[46] C. L. Dumoulin, S. P. Souza, and R. D. Darrow, “Real-time position monitoring of invasive devices using magnetic resonance,” Magn. Reson. Med., vol. 29, no. 3, pp. 411–415, 1993.

[47] A. Glowinski, J. Kürsch, G. Adam, A. Bücker, T. G. Noll, and R. W. Günther, “Device visualization for interventional MRI using local magnetic fields: Basic theory and its application to catheter visualization,” IEEE Trans. Med. Imaging, vol. 17, no. 5, pp. 786–793, 1998.

[48] D. K. Yildirim, M. Sonmez, R. J. Lederman, and O. Kocaturk, “A novel active device fabrication method for interventional MRI procedure,” in IFMBE Proceedings, vol 62., 2017, pp. 122–128.

[49] W. R. Nitz, A. Oppelt, W. Renz, C. Manke, M. Lenhart, and J. Link, “On the heating of linear conductive structures as guide wires and catheters in interventional MRI,” J. Magn. Reson. Imaging, vol. 13, no. 1, pp. 105–114, 2001.

[50] M. Sonmez et al., “MRI active guidewire with an embedded temperature probe and providing a distinct tip signal to enhance clinical safety,” J. Cardiovasc. Magn. Reson., vol. 14, no. 1, pp. 1–10, 2012.

[51] C. L. Dumoulin, “Active Visualization — MR Tracking BT - Interventional Magnetic Resonance Imaging,” J. F. Debatin and G. Adam, Eds. Berlin, Heidelberg: Springer Berlin Heidelberg, 1998, pp. 65–75.

[52] S. M. Park, R. Kamondetdacha, A. Amjad, and J. A. Nyenhuis, “MRI safety: RF-induced heating near straight wires,” IEEE Trans. Magn., vol. 41, no. 10, pp. 4197–4199, 2005.

[53] K. N. Kurpad and O. Unal, “Multimode intravascular RF coil for MRI-guided interventions,” J. Magn. Reson. Imaging, vol. 33, no. 4, pp. 995–1002, 2011.

[54] M. Etezadi-Amoli, P. Stang, A. Kerr, J. Pauly, and G. Scott, “Controlling radiofrequency-induced currents in guidewires using parallel transmit,” Magn. Reson. Med., vol. 74, no. 6, pp. 1790–1802, 2015.

[55] A. C. Özen, T. Lottner, and M. Bock, “Safety of active catheters in MRI: Termination impedance versus RF-induced heating,” Magn. Reson. Med., vol. 81, no. 2, pp. 1412–1423, 2019.

[56] S. Fandrey, S. Weiss, and J. Muller, “Development of an Active Intravascular MR Device With an Optical Transmission System,” IEEE Trans. Med. Imaging, vol. 27, no. 12, pp. 1723–1727, 2008.

[57] S. Fandrey, S. Weiss, and J. Muller, “A novel active MR probe using a miniaturized optical link for a 1.5-T MRI scanner,” Magn. Reson. Med., vol. 67, no. 1, pp. 148–155, 2012.

[58] P. A. Bottomley, A. Kumar, W. A. Edelstein, J. M. Allen, and P. V. Karmarkar, “Designing passive MRI-safe implantable conducting leads with electrodes,” Med. Phys., vol. 37, no. 7, pp. 3828–3843, 2010.

[59] O. G. Memis, Y. Eryaman, O. Aytur, and E. Atalar, “Miniaturized fiber-optic transmission system for MRI signals,” Magn. Reson. Med., vol. 59, no. 1, pp. 165–173, 2008.

[60] E. Y. Wong, Q. Zhang, J. L. Duerk, J. S. Lewin, and M. Wendt, “An optical system for wireless detuning of parallel resonant circuits,” J. Magn. Reson. Imaging, vol. 12, no. 4, pp. 632–638, 2000.

[61] S. Weiss et al., “In vivo safe catheter visualization and slice tracking using an optically detunable resonant marker,” Magn. Reson. Med., vol. 52, no. 4, pp. 860–868, 2004.

[62] S. Nazarian et al., “Feasibility of Real-Time Magnetic Resonance Imaging for Catheter Guidance in Electrophysiology Studies,” Circulation, vol. 118, no. 3, pp. 223–229, 2008.

[63] M. Bock, R. Umathum, J. Sikora, S. Brenner, E. N. Aguor, and W. Semmler, “A Faraday effect position sensor for interventional magnetic resonance imaging,” Phys. Med. Biol., vol. 51, no. 4, pp. 999–1009, 2006.

[64] B. Sarioglu, O. Aktan, A. Oncu, S. Mutlu, G. Dundar, and A. D. Yalcinkaya, “An optically powered CMOS receiver system for intravascular magnetic resonance applications,” IEEE J. Emerg. Sel. Top. Circuits Syst., vol. 2, no. 4, pp. 683–691, 2012.

[65] V. M. Tronnier et al., “Intraoperative diagnostic and interventional magnetic resonance imaging in neurosurgery,” Neurosurgery, vol. 40, no. 5, pp. 891–902, 1997.

[66] D. F. Saldanha et al., “Current tumor ablation technologies: basic science and device review,” in Seminars in interventional radiology, 2010, vol. 27, no. 3, pp. 247–254.

[67] K. Hynynen, “MRIgHIFU: A tool for image-guided therapeutics,” J. Magn. Reson. Imaging, vol. 34, no. 3, pp. 482–493, 2011.

[68] C. Yiu-Cho, D. J. L., S. Ajit, H. Monika, M. E. M., and L. J. S., “Temperature measurement using echo-shifted FLASH at low field for interventional MRI,” J. Magn. Reson. Imaging, vol. 9, no. 1, pp. 138–145, Feb. 1999.

[69] J. Fritz, A. Chhabra, K. C. Wang, and J. A. Carrino, “Magnetic Resonance Neurography–Guided Nerve Blocks for the Diagnosis and Treatment of Chronic Pelvic Pain Syndrome,” Neuroimaging Clin., vol. 24, no. 1, pp. 211–234, Feb. 2014.

[70] R. J. Lederman, “Cardiovascular Interventional MRI,” Circulation, vol. 112, no. 19, pp. 3009–3017, Nov. 2005.

[71] J. Fritz, C. Thomas, S. Clasen, C. D. Claussen, J. S. Lewin, and P. L. Pereira, “Freehand Real-Time MRI-Guided Lumbar Spinal Injection Procedures at 1.5 T: Feasibility, Accuracy, and Safety,” Am. J. Roentgenol., vol. 192, no. 4, pp. W161–W167, Apr. 2009.

[72] N. A. Patel et al., “System Integration and Preliminary Clinical Evaluation of a Robotic System for MRI-Guided Transperineal Prostate Biopsy,” J. Med. Robot. Res., vol. 4, no. 2, p. 1950001, Apr. 2018.

[73] P. A. Bottomley, R. W. Redington, W. A. Edelstein, and J. F. Schenck, “Estimating radiofrequency power deposition in body NMR imaging,” Magn. Reson. Med., vol. 2, no. 4, pp. 336–349, Aug. 1985.

[74] G. Durbridge, “Magnetic resonance imaging: Fundamental safety issues,” J. Orthop. Sports Phys. Ther., vol. 41, no. 11, pp. 820–828, 2011.

[75] F. G. Shellock, “Radiofrequency energy-induced heating during MR procedures: a review,” J. Magn. Reson. Imaging, vol. 12, no. 1, pp. 30–36, 2000.

[76] L. A. Zaremba, FDA guidance for magnetic resonance system safety and patient exposures: Current status and future considerations. 2001.

[77] I. E. Consortium, “IEC 60601-2-33. Medical electrical equipment-Part 2-33: Particular requirements for the safety of magnetic resonance equipment for medical diagnosis.” 2003.

[78] “US Food and Drug Administration. Guidance for industry and FDA staff: criteria for significant risk investigations of magnetic resonance diagnostic devices.” .

[79] C. K. Chou et al., “Radio Frequency Electromagnetic Exposure : Tutorial Review on Experimental Dosimetry,” vol. 208, no. 1 996, pp. 195–208, 1996.

[80] G. S. Smith, “Limitations on the Size of Miniature Electric-Field Probes,” IEEE Trans. Microw. Theory Tech., vol. 32, no. 6, pp. 594–600, 1984.

[81] H. Bassen and G. Smith, “Electric field probes--A review,” IEEE Trans. Antennas Propag., vol. 31, no. 5, pp. 710–718, 1983.

[82] P. Jarrige et al., “Electro-Optic Probe Devoted to Simultaneous Electric Field and Temperature Measurement in Biological Media for Dosimetric Assessments,” Radio Sci. Bull., vol. 342, no. 342, pp. 5–15, 2012.

[83] S. Reiss, A. Bitzer, and M. Bock, “An optical setup for electric field measurements in MRI with high spatial resolution,” Phys. Med. Biol., vol. 60, no. 11, pp. 4355–4370, 2015.

[84] L. Duvillaret, S. Rialland, and J.-L. Coutaz, “Electro-optic sensors for electric field measurements I Theoretical comparison among different modulation techniques,” J. Opt. Soc. Am. B, vol. 19, no. 11, p. 2692, 2002.

[85] “Courtesy of ITiS Foundation.” .

[86] Y. Zhang, G. R. Pickrell, B. Qi, A. Safaai-Jazi, and A. Wang, “Single-crystal sapphire based optical polarimetric sensor for high temperature measurement,” Sensors, vol. 6, no. 8, pp. 823–834, 2006.

[87] D. A. Christensen, “Fiberoptic Temperature Sensing For Biomedical Applications,” 1988, vol. 906, no., p. 906.

[88] D. A. Jackson, M. W. Hathaway, D. A. Jackson, and I. Bennion, “First in-vivo trials of a fiber Bragg grating based temperature profiling system First in-vivo trials of a fiber Bragg grating based temperature profiling system,” vol. 5, no. FEBRUARY 2000, pp. 45–50, 2000.

[89] G. Palumbo et al., “Temperature profile of ex-vivo organs during radio frequency thermal ablation by fiber Bragg gratings,” J. Biomed. Opt., vol. 21, no. 11, p. 117003, 2016.

[90] E. Samset, T. Mala, R. Ellingsen, I. Gladhaug, O. Søreide, and E. Fosse, “Temperature measurement in soft tissue using a distributed fibre Bragg-grating sensor system,” Minim. Invasive Ther. Allied Technol., vol. 10, no. 2, pp. 89–93, Jan. 2001.

[91] F. Taffoni, D. Formica, P. Saccomandi, G. Di Pino, and E. Schena, “Optical Fiber-Based MR-Compatible Sensors for Medical Applications: An Overview,” Sensors, vol. 13, no. 10, pp. 14105–14120, 2013.

[92] A. Ostroff, “Temperature sensor for a leadless cardiac pacemaker.” Google Patents, Sep-2013.

[93] C. Armenean, E. Perrin, M. Armenean, O. Beuf, F. Pilleul, and H. Saint-Jalmes, “RF-induced temperature elevation along metallic wires in clinical magnetic resonance imaging: Influence of diameter and length,” Magn. Reson. Med., vol. 52, no. 5, pp. 1200–1206, 2004.

[94] Nyenhuis, A. V. Kildishev, J. D. Bourland, K. S. Foster, and G. Graber, “Heating near implanted medical devices by the mri rf-magnetic field,” IEEE Trans. Magn., vol. 35, no. 5 PART 2, pp. 4133–4135, 1999.

[95] “ISO/TS 10974:2018 Assessment of the safety of magnetic resonance imaging for patients with an active implantable medical device,” 2018.

[96] L. Brix, C. Isaksen, K. BH, and D. Tufa, “Third degree skin burns caused by a MRI conditional electrocardiographic monitoring system,” J. Radiol. Imaging, vol. 1, no. 5, pp. 29–32, 2016.

[97] N. J. Berg and J. N. Lee, “Acousto-optic signal processing: theory and implementation,” in New York, Marcel Dekker, Inc.(Optical Engineering. Volume 2), 1983, 496 p. No individual items are abstracted in this volume., 1983, vol. 2.

[98] R. G. Hunsperger, “Acousto-Optic Modulators BT - Integrated Optics: Theory and Technology,” R. G. Hunsperger, Ed. New York, NY: Springer New York, 2009, pp. 201–220.

[99] “Fiber Bragg Gratings.” .

[100] G. Wild and S. Hinckley, “Acousto-ultrasonic optical fiber sensors: Overview and state-of-the-art,” IEEE Sens. J., vol. 8, no. 7, pp. 1184–1193, 2008.

[101] G. Wissmeyer, D. Soliman, R. Shnaiderman, A. Rosenthal, and V. Ntziachristos, “All-optical optoacoustic microscope based on wideband pulse interferometry,” Opt. Lett., vol. 41, no. 9, p. 1953, 2016.

[102] a. a. Godil, D. B. Patterson, B. L. Heffner, G. S. Kino, and B. T. Khuri-Yakub, “All-fiber acoustooptic phase modulators using zinc oxide films on glass fiber,” J. Light. Technol., vol. 6, no. 10, pp. 1586–1590, 1988.

[103] M. P. Roe, B. Wacogne, and C. N. Pannell, “High-efficiency all-fiber phase modulator using an annular zinc oxide piezoelectric transducer,” IEEE Photonics Technol. Lett., vol. 8, no. 8, pp. 1026–1028, 1996.

[104] G. R. Fox, N. Setter, and H. G. Limberger, “Fabrication and structural analysis of ZnO coated fiber optic phase modulators,” J. Mater. Res., vol. 11, no. 8, pp. 2051–2061, 1996.

[105] A. Rosenthal, D. Razansky, and V. Ntziachristos, “High-sensitivity compact ultrasonic detector based on a pi-phase-shifted fiber Bragg grating.,” Opt. Lett., vol. 36, no. 10, pp. 1833–1835, 2011.

[106] D. C. Betz, G. Thursby, B. Culshaw, and W. J. Staszewski, “Acousto-ultrasonic sensing using fiber Bragg gratings,” Smart Mater. Struct, vol. 12, no. 3, pp. 122–128, 2003.

[107] N. Takahashi, K. Yoshimura, S. Takahashi, and K. Imamura, “Development of an optical fiber hydrophone with fiber Bragg grating,” Ultrasonics, vol. 38, no. 1, pp. 581–585, 2000.

[108] P. A. Lewin, C. Mu, S. Umchid, A. Daryoush, and M. El-Sherif, “Acousto-optic, point receiver hydrophone probe for operation up to 100 MHz,” Ultrasonics, vol. 43, no. 10, pp. 815–821, 2005.

[109] A. D. Kersey, T. A. Berkoff, and W. W. Morey, “Multiplexed fiber Bragg grating strain-sensor system with a fiber Fabry--Perot wavelength filter,” Opt. Lett., vol. 18, no. 16, pp. 1370–1372, Aug. 1993.

[110] G. B. Hocker, “Fiber-optic sensing of pressure and temperature.,” Appl. Opt., vol. 18, no. 9, pp. 1445–1448, 1979.

[111] L.-H. Kang, D.-K. Kim, and J.-H. Han, “Estimation of dynamic structural displacements using fiber Bragg grating strain sensors,” J. Sound Vib., vol. 305, no. 3, pp. 534–542, 2007.

[112] T. Liu and M. Han, “Analysis of fiber bragg gratings for ultrasonic detection,” IEEE Sens. J., vol. 12, no. 7, pp. 2368–2373, 2012.

[113] P. Fomitchov and S. Krishnaswamy, “Response of a fiber Bragg grating ultrasonic sensor,” Opt. Eng., vol. 42, no. 4, pp. 956–963, 2003.

[114] Q. Wu and Y. Okabe, “High-sensitivity ultrasonic phase-shifted fiber Bragg grating balanced sensing system.,” Opt. Express, vol. 20, no. 27, pp. 28353–62, 2012.

[115] B. Sutapun, M. Tabib-Azar, and A. Kazemi, “Pd-coated elastooptic fiber optic Bragg grating sensors for multiplexed hydrogen sensing,” Sensors Actuators B Chem., vol. 60, no. 1, pp. 27–34, 1999.

[116] H. J. Bang, H. Il Kim, and K. S. Lee, “Measurement of strain and bending deflection of a wind turbine tower using arrayed FBG sensors,” Int. J. Precis. Eng. Manuf., vol. 13, no. 12, pp. 2121–2126, 2012.

[117] D. C. Betz, G. Thursby, B. Culshaw, and W. J. Staszewski, “Acousto-ultrasonic sensing using fiber Bragg gratings,” Smart Mater. Struct., vol. 12, no. 1, p. 122, 2003.

[118] Y. J. Rao, “In-fibre Bragg grating sensors,” Meas. Sci. Technol., vol. 8, no. 4, pp. 355–375, 1997.

[119] W.-P. Huang, “Coupled-mode theory for optical waveguides: an overview,” J. Opt. Soc. Am. A, vol. 11, no. 3, p. 963, 1994.

[120] S. M. Norton, T. Erdogan, and G. M. Morris, “Coupled-mode theory of resonant-grating filters,” J. Opt. Soc. Am. A, vol. 14, no. 3, p. 629, 1997.

[121] G. S. Kino, Acoustic waves: devices, imaging and analog signal processing, no. 43 KIN. 1987.

[122] C. A. F. Marques, R. A. Oliveira, A. A. P. Pohl, J. Canning, and R. N. Nogueira, “Dynamic control of a phase-shifted FBG through acousto-optic modulation,” Opt. Commun., vol. 284, no. 5, pp. 1228–1231, 2011.

[123] Q. Wu, Y. Okabe, K. Saito, and F. Yu, “Sensitivity Distribution Properties of a Phase-Shifted Fiber Bragg Grating Sensor to Ultrasonic Waves,” Sensors, vol. 14, no. 1, pp. 1094–1105, 2014.

[124] S. A. Counter, A. Olofsson, H. F. Grahn, and E. Borg, “MRI acoustic noise: Sound pressure and frequency analysis,” J. Magn. Reson. Imaging, vol. 7, no. 3, pp. 606–611, 1997.

[125] B. Yu, D. W. Kim, J. Deng, H. Xiao, and A. Wang, “Fiber Fabry-Perot sensors for detection of partial discharges in power transformers,” Appl. Opt., vol. 42, no. 16, pp. 3241–3250, 2003.

[126] P. C. Beard, “Transduction mechanisms of the Fabry-Perot polymer film sensing concept for wideband ultrasound detection,” IEEE Trans. Ultrason. Ferroelectr. Freq. Control, vol. 46, no. 6, pp. 1575–1582, 1999.

[127] J. G. Och, G. D. Clarke, W. T. Sobol, C. W. Rosen, and S. K. Mun, “Acceptance testing of magnetic resonance imaging systems: report of AAPM Nuclear

Magnetic Resonance Task Group No. 6," Med. Phys., vol. 19, no. 1, pp. 217–229, 1992.

[128] R. Hui, "Chapter 4 - Photodetectors," R. B. T.-I. to F.-O. C. Hui, Ed. Academic Press, 2020, pp. 125–154.

[129] B. C. Buchler, E. H. Huntington, C. C. Harb, and T. C. Ralph, "Feedback control of laser intensity noise," Phys. Rev. A, vol. 57, no. 2, pp. 1286–1294, Feb. 1998.

[130] R. Paschotta, "Noise in Laser Technology," Opt. Photonik, vol. 4, no. 2, pp. 48–50, 2009.

[131] D. Morgan, A handbook for EMC testing and measurement, vol. 8. Iet, 1994.

[132] M. L. Crawford and J. L. Workman, Using a TEM cell for EMC measurements of electronic equipment, vol. 1013. Department of Commerce, Office of the Assistant Secretary of Commerce for …, 1979.

[133] E. Kaverine, S. Palud, F. Colombel, and M. Himdi, "Simple Approach to Miniaturized Antenna Gain Measurement Using a Parallel Plate Cell in the HF Band," vol. 46, no. January, pp. 11–18, 2016.

[134] S. M. Satav and V. Agarwal, "Do-it-Yourself Fabrication of an Open TEM Cell for EMC Pre-compliance," IEEE EMC Soc. Newsl., no. 20, pp. 66–71, 2008.

[135] V. M. N. Passaro, F. Dell'Olio, and F. De Leonardis, "Electromagnetic field photonic sensors," Prog. Quantum Electron., vol. 30, no. 2–3, pp. 45–73, 2006.

[136] T. Cheng, X. Zhou, and G. An, "A novel optical-fiber magnetic field sensor based on Surface Plasma resonance," 2018.

[137] C. Hao, Y. Song, W. Zhang, Y. Ma, F. Li, and D. Li, "Magnetic field sensor using Cu-coated DFB Fiber laser," Asia Commun. Photonics Conf. ACP, vol. 2018–Octob, pp. 3–6, 2018.

[138] S. M. M. Quintero, A. M. B. Braga, H. I. Weber, A. C. Bruno, and J. F. D. F. Araújo, "A magnetostrictive composite-fiber bragg grating sensor," Sensors, vol. 10, no. 9, pp. 8119–8128, 2010.

[139] L. Luo, S. Pu, S. Dong, and J. Tang, “Sensors and Actuators A : Physical Fiber-optic magnetic field sensor using magnetic fluid as the cladding,” vol. 236, pp. 67–72, 2015.

[140] M. J. P. van Osch and A. G. Webb, “Safety of ultra-high field MRI: what are the specific risks?,” Curr. Radiol. Rep., vol. 2, no. 8, p. 61, 2014.

[141] Z. Wang, J. C. Lin, W. Mao, W. Liu, M. B. Smith, and C. M. Collins, “SAR and temperature: Simulations and comparison to regulatory limits for MRI,” J. Magn. Reson. Imaging, vol. 26, no. 2, pp. 437–441, 2007.

[142] A. E. Campbell-Washburn et al., “Opportunities in interventional and diagnostic imaging by using high-performance low-field-strength MRI,” Radiology, vol. 293, no. 2, pp. 384–393, 2019.

[143] S. Sathyanarayana and P. A. Bottomley, “MRI endoscopy using intrinsically localized probes,” Med. Phys., vol. 36, no. 3, pp. 908–919, 2009.

[144] H. Gu, F. Zhang, Y. Meng, B. Qiu, and X. Yang, “Development of a 0.014-in., anti-solenoid loop MR imaging guidewire for intravascular 3.0-T MR imaging,” Magn. Reson. Imaging, vol. 29, no. 7, pp. 1002–1006, 2011.

[145] C. R. Wuethrich, C. a. P. Muller, G. R. Fox, and H. G. Limberger, “All-fibre acousto-optic modulator using ZnO piezoelectric actuators,” Sensors Actuators A Phys., vol. 66, no. 1–3, pp. 114–117, 1998.

[146] T. Kaneko, K. Iwata, and M. Kobayashi, “Piezoelectric sol-gel composite film fabrication by stencil printing,” IEEE Trans. Ultrason. Ferroelectr. Freq. Control, vol. 62, no. 9, pp. 1686–1695, 2015.

[147] N. Ozer, Sol-Gel Optics: Processing and applications, vol. 43, no. 3. 1996.

[148] P. C. Beard, A. M. Hurrell, and T. N. Mills, “Characterization of a polymer film optical fiber hydrophone for use in the range 1 to 20 MHz: A comparison with PVDF needle and membrane hydrophones,” IEEE Trans. Ultrason. Ferroelectr. Freq. Control, vol. 47, no. 1, pp. 256–264, 2000.

[149] Y. S. Yaras et al., "Acousto-Optic Catheter Tracking Sensor for Interventional MRI Procedures," IEEE Transactions on Biomedical Engineering, vol. 66, no. 4, pp. 1148-1154, 2019.

[150] Y. S. Yaras, D. K. Yildirim, O. Kocaturk, and F. L. Degertekin, "Sensitivity and phase response of FBG based acousto-optic sensors for real-time MRI applications," OSA Continuum 3, 447-458, 2020.